

# **De Eikonale Benadering in Dirac-Geïnspireerde Modellen voor $A(e,e'p)$ Reacties.**

The Eikonal Approximation  
in Dirac-Based Models  
for  $A(e,e'p)$  Reactions.

Dimitri Debruyne

Promotor: Prof. dr. J. Ryckebusch

Proefschrift ingediend tot het behalen van de graad van  
Doctor in de Toegepaste Wetenschappen

Vakgroep Subatomaire en Stralingsfysica  
Voorzitter: Prof. dr. K. Heyde  
Faculteit Wetenschappen  
Academiejaar 2000-2001





# Contents

---

<b>Table of Contents</b>	<b>i</b>
<b>1 Introduction</b>	<b>1</b>
<b>2 Reaction Observables and Kinematics</b>	<b>5</b>
<b>3 Relativistic Bound State Wave Functions</b>	<b>13</b>
3.1 Formalism . . . . .	14
3.2 Results . . . . .	16
<b>4 Off-Shell Electron-Proton Coupling</b>	<b>25</b>
<b>5 The Eikonal Final State</b>	<b>31</b>
5.1 The Relativistic Distorted Wave Approximation . . . . .	32
5.2 A Consistent Approach to Final State Interactions . . . . .	33
5.3 Optical Potentials and the Eikonal Method . . . . .	36
5.4 The Glauber Approach . . . . .	40
5.4.1 Non-relativistic Glauber theory . . . . .	40
5.4.2 Connection between the Profile Function and the NN Potential	48
5.4.3 Glauber Multiple Scattering Theory . . . . .	50
5.4.4 Relativistic Extension of the Glauber Approximation . . . . .	52
5.5 Higher Order Eikonal Corrections . . . . .	54
<b>6 Final State Interactions and the Eikonal Approximation</b>	<b>57</b>
6.1 $^{16}\text{O}(e, e'p)^{15}\text{N}$ . . . . .	57
6.1.1 The Self-Consistent Approach . . . . .	58
6.1.2 The Eikonal Approximation with Optical Potentials and the Glauber Multiple Scattering Extension	
6.2 $^{12}\text{C}(e, e'p)^{11}\text{B}$ . . . . .	70
<b>7 Off-Shell Ambiguities</b>	<b>77</b>
<b>8 Relativistic Effects</b>	<b>93</b>
<b>9 Nuclear Transparency</b>	<b>103</b>
9.1 Theoretical Background . . . . .	103
9.2 Review of Experimental Results . . . . .	108
9.3 Nuclear Transparency Calculations . . . . .	113

<b>10 Conclusion and Outlook</b>	<b>121</b>
<b>Bibliography</b>	<b>125</b>

---

# Chapter 1

## Introduction

---

Nuclear physics is the study of atomic nuclei. The primary aim of nuclear physics is to understand the force between nucleons, the structure of nuclei, and how nuclei interact with each other and with other subatomic particles. These three questions are, to a large extent, related to each other. It has been known for years that the nucleus is a many-body system of protons and neutrons, the two lightest members of the baryon family, that is held together by the strong nuclear force. Traditional models of nuclei rely on the shell model, where it is assumed that both protons and neutrons are moving independently in an average mean-field potential, which expresses the interaction of the nucleon with the surrounding medium. The nucleons then occupy the lowest single-particle levels up to the Fermi energy, whereas the single-particle levels above the Fermi energy remain unoccupied. From systematic investigations for a large number of target nuclei a richness of precise information about the independent-particle wave functions and spectroscopic strengths was assembled [1], and it turned out that many nuclear features could be explained within this single-particle picture.

However, as nucleons in the nucleus interact with each other through the strong, short-ranged interaction, a number of nuclear structure properties remains unexplained in the basic independent-particle model. An extensive amount of measurements has made it clear that the occupancy of the single-particle level is substantially smaller than what is expected in a naive independent-particle model. This observation has resulted in the conjecture that 2/3's of the nucleons in the nucleus act as independent quasi-particles, whereas the remaining ones are then correlated [1].

A full understanding of the nucleus can not be achieved without some knowledge about the underlying mechanisms that are responsible for the strong nuclear force. The strong nuclear force manifests itself as a result of the strongly interacting quark and gluon constituents which build up the nucleon. A better understanding of the quantum chromodynamics (QCD) theory which describes the strong interaction between quarks and gluons, will most certainly lead to a better understanding of

the strong nuclear force.

Electron scattering from nuclei provides us with an invaluable tool to probe the wide variety of nuclear and nucleonic properties. Electron scattering is an ideal way to study the limits of the independent single-particle model as it only interacts very weakly (compared to the strong nuclear force) with the nucleus through the electromagnetic interaction. This ensures that the mean free path of the electron is large enough to probe the entire nuclear volume. A hadronic probe interacts strongly with the nucleus and significantly disturbs the target object. Furthermore, the electromagnetic interaction is well understood. Quantum electrodynamics, the quantum field theory of electrons and photons, has produced predictions that are in excellent agreement with experimental observations. Therefore, the uncertainties in reaction modelling are restricted to the nuclear part of the reaction. In electron scattering experiments one can also vary the transferred momentum  $\vec{q}$  and energy  $\omega$  of the exchanged virtual photon independently from each other, as long as the virtual photon is space-like (i.e.  $|\vec{q}|^2 - \omega^2 > 0$ ). This is a big advantage over experiments using real photons as an electromagnetic probe.

In this work, we will focus on processes whereby the nucleus is struck by an electron, with the result that one of its protons is ejected, and is detected by the experimental setup. In the past, these exclusive  $A(e, e'p)B$  reactions have revealed a wealth of important information on the structure of nuclei and nucleons.

At low values of the virtual photon's four-momentum transfer  $Q^2 = \vec{q}^2 - \omega^2$  and, accordingly, large distance scales, the quasielastic  $A(e, e'p)$  reaction probes the mean-field structure of nuclei and allows to test the limits of the independent single-particle model.

At high  $Q^2$  and decreasing distance scales, the scope of exclusive  $(e, e'p)$  measurements shifts towards other physics issues, including

- Short-range structure of nuclei : are there any hadronic components in the nucleus that carry large momenta, or are the large momenta components in the nuclear wave function carried by the partonic degrees of freedom ?
- Quenching disappearance and single-particle strength restoration : how do spectroscopic factors evolve as  $Q^2$  is increased ? Is there some sort of scale dependence in nuclear physics ?
- Stringent tests of constituent quark models : to what extent are nucleons modified in the medium ?
- Nuclear transparency : are there any signatures for the onset of color transparency, which is a genuine QCD effect ? Within the context of exclusive  $(e, e'p)$  reactions, color transparency stands for the suggestion that at sufficiently high values of  $Q^2$  the struck proton may interact in an anomalously weak manner with the spectator nucleons in the target nucleus [2, 3, 4].

In this work, we will concentrate on  $A(e, e'p)$  reactions at intermediate and high  $Q^2$ . For all of the aforementioned physics issues, the interpretation of  $A(e, e'p)$  reactions very much depends on the availability of realistic models that describe the final state interactions.

The extraction of physical information from measured  $A(e, e'p)B$  cross sections usually involves some theoretical modelling of which the major ingredients are the initial (bound) and final (scattering) proton wave functions and the electromagnetic electron-nucleus coupling. At lower values of  $Q^2$ , most theoretical work on  $(e, e'p)$  reactions was performed in the so-called distorted-wave impulse approximation (DWIA). The idea behind the DWIA approach is that the initial (bound) and final (scattering) state of the struck nucleon can be computed in a potential model, whereas for the electron-nucleus coupling an off-shell corrected electron-proton form can be used. The wealth of high-quality  $(e, e'p)$  data that the electron-scattering experiments have provided over the last 20 years, made sure that the DWIA models are well tested against experimental data. For higher values of the energy and momentum transfer [ $Q^2 \geq 1$  (GeV/c)<sup>2</sup>], most theoretical work starts from the nonrelativistic Glauber theory [5]. This theory is highly successful in describing small-angle proton-nucleus scattering at higher energies [6] and is conceived as a baseline for calculating the effect of final state interactions in high-energy  $(e, e'p)$  reactions. Glauber theory is a multiple-scattering extension of the standard eikonal approximation that relates through a profile function the ejectile's distorted wave function to the elastic proton scattering amplitude [7, 8, 9, 10, 11]. The Glauber method has frequently been shown to be reliable in describing  $A(p, p')$  processes. Several nonrelativistic studies [12, 13, 14] have formally investigated the applicability of the Glauber model for describing  $A(e, e'p)$  reactions at higher energies and momentum transfers. These investigations were often hampered by the lack of  $A(e, e'p)$  data to compare the model calculations with. Recently, the first high-quality data for  $^{16}\text{O}(e, e'p)$  cross sections, separated structure functions and polarization observables became available [15].

Since relativistic effects are expected to become critical in the GeV energy domain, we explore the possibility of developing a fully relativistic model for describing  $A(e, e'p)$  processes. Various alternative methods to deal with final state interactions will be developed. In a first approach we will solve the relevant equations for the final state wave function in the eikonal limit, thereby using the mean-field potentials as they are obtained from bound state calculations. In a second step, we introduce optical potentials, constructed from experimental nucleon-nucleus scattering data, into the eikonal formalism in order to fully accommodate the effects of inelastic mechanisms in the  $A(e, e'p)$  scattering process. As we want to make a comparison of the eikonal model and Glauber theory, we also present a relativistic generalization of the Glauber multiple-scattering formalism.

The work presented here is a formulation of a fully relativistic model for the description of  $A(e, e'p)$  reactions that bridges the gap between the low and intermediate energy regime. The model developed in this work can be formally applied in

a wide  $Q^2$  range. As a matter of fact, we employ the relativistic eikonal method to estimate the sensitivity of  $(e, e'p)$  observables in the few GeV regime to a number of physical effects, including off-shell ambiguities, dynamical relativity and nuclear transparency.

The outline of this work is as follows. In Sec. 2 we introduce the formalism for the relevant  $A(e, e'p)$  observables and kinematics. Sec. 3 comprises the method employed to determine the bound states. We adopt a relativistic mean-field approximation to the Walecka model [16] to determine the bound-state wave functions and binding energies, as well as the nucleon and meson potentials. Results of these calculations are also presented here for the  $^{12}\text{C}$  and  $^{16}\text{O}$  nuclei. The various forms of the photon-nucleus interaction are introduced in Sec. 4. The different methods to deal with final-state interactions are developed in Sec. 5. Both the eikonal and the Glauber method are addressed, along with their relativistic and multiple-scattering extensions. The major results of this work are presented in Secs. 6, 7, 8 and 9. In Sec. 6 we compare  $A(e, e'p)$  predictions obtained with various prescriptions to deal with the final-state interactions. In particular, we concentrate on the fully relativistic eikonal method with complex scattering potentials and the relativistic Glauber multiple-scattering method. In Sec. 7 we adopt different prescriptions for the electron-nucleus coupling. By doing this, we estimate the sensitivity of the observables to the theoretical uncertainties that surround the choice of the off-shell electron-proton vertex. It is often claimed that off-shell ambiguities decrease in importance as the four-momentum transfer increases. Here we make an attempt to quantify the relative importance of the off-shell effects for the  $(e, e'p)$  structure functions by comparing results obtained with different off-shell electron-proton couplings. Hereby we are primarily concerned with the question how big the uncertainties remain when higher and higher four-momentum transfers are probed. In Sec. 8 we study the effects of the dynamical relativity that is introduced in the model by evaluating the role of the lower components of the bound and scattering states. A comparison with non-relativistic calculations is performed in order to estimate its effects on the  $(e, e'p)$  observables in a wide  $Q^2$  range. In Sec. 9 we take a closer look at the nuclear transparency in  $A(e, e'p)$  reactions. We present a brief overview of the experimental and theoretical results up to now, and also show results of our own calculations of the nuclear transparency in  $^{12}\text{C}$ . Our concluding remarks are summarized in Sec. 10.

---

## Chapter 2

# Reaction Observables and Kinematics

---

The fundamental theory of QED has produced predictions that are in excellent agreement with experimental observations. When considering electron scattering from nucleons and nuclei, the leptonic part of the process can be assumed to be well under control. Therefore, the uncertainties in the reaction modelling are restricted to the nuclear part of the reaction, namely, the electron-nucleon (nucleus) vertex and the physics governing the structure and the dynamics of the nucleon (nucleus). Furthermore, the electromagnetic coupling, characterized by the fine-structure constant  $\alpha \equiv e^2/\hbar c \approx 1/137$ , is relatively small, and, consequently, one only needs to consider the lowest order electromagnetic processes involved. This lowest order one-photon-exchange approximation is generally conceived to be sufficiently accurate. In this work we will only consider one-photon-exchange contributions together with plane wave electrons, the so-called plane wave Born approximation, (PWBA), as is commonly done. The more general case, which implies the use of distorted ingoing and outgoing electron waves, has been the subject of intensive investigations in the past [17, 18, 19, 20]. For light target nuclei, upon which we focus here, the effect of these so-called Coulomb distortion effects is rather small. Corrections from higher-order photon exchange contributions, can also be considered [21, 22, 23], but it has been shown that these corrections are roughly inversely proportional to the incident electron energy, and should not be considered a problem in the intermediate to high energy range [ $Q^2 > 1(\text{GeV}/c)^2$ ]. A formal separation of the coincidence cross section into the different structure functions is only feasible when adopting a plane wave framework for the electron waves.

Historically, electron scattering experiments were performed with unpolarized beams, simply because the technology required to polarize and measure electron beams was lacking. With unpolarized electron beams, two form factors can be extracted from  $p(e, e')$  cross sections. They correspond to the longitudinal and

transverse polarization of the absorbed photon, respectively. This separation is well known as the Rosenbluth decomposition [24]. Exclusive reactions from composite systems in which one or more particles are detected in coincidence with the scattered electron, allow to extract additional information about the target system. At present, the availability of high-duty electron facilities make these coincidence experiments involving the analysis of polarization degrees of freedom much easier than in previous times.

In discussing  $A + e \rightarrow B + e' + p$  processes, one faces the possibility of polarizing the incident and scattered wave, as well as the hadrons in the initial and final channel. In this work we will follow the conventions for the  $A(\vec{e}, \vec{e}'\vec{p})B$  kinematics and observables introduced by Donnelly and Raskin in Refs. [25, 26].

The four-momenta of the incident and scattered electron are labeled as  $K^\mu(\epsilon, \vec{k})$  and  $K'^\mu(\epsilon', \vec{k}')$ . The electron momenta  $\vec{k}$  and  $\vec{k}'$  define the scattering plane. The four-momentum transfer is given by  $q^\mu = K^\mu - K'^\mu = K_{A-1}^\mu + K_f^\mu - K_A^\mu$ , where  $K_A^\mu$  and  $K_{A-1}^\mu$  are the four-momenta of the target and residual nucleus, respectively, while  $K_f^\mu$  is the four-momentum of the ejected nucleon. Also,  $q^\mu = (\omega, \vec{q})$ , where the three-momentum transfer  $\vec{q} = \vec{k} - \vec{k}' = \vec{k}_{A-1} + \vec{k}_f - \vec{k}_A$ , and the energy transfer  $\omega = \epsilon - \epsilon' = E_{A-1} + E_f - E_A$ , are defined in the standard manner. The  $xyz$  coordinate system is chosen such that the  $z$ -axis lies along the momentum transfer  $\vec{q}$ , the  $y$ -axis lies along  $\vec{k} \times \vec{k}'$  and the  $x$ -axis lies in the scattering plane; the reaction plane is then defined by  $\vec{k}_f$  and  $\vec{q}$ , as in Fig. 2.1.

We now discuss processes in which a polarized electron with helicity  $h$  impinges on a nucleus and induces the knockout of a single nucleon, leaving the residual nucleus in a specific discrete state. The Feynman diagram corresponding to this process is shown in Fig. 2.2. The Bjorken-Drell convention [27] for the  $\gamma$  matrices and Dirac spinors is followed. Accordingly, the normalization condition for the Dirac plane waves, characterized by a four-momentum  $K^\mu$  and spin-state  $S^\mu$ , is

$$\bar{u}(K^\mu, S^\mu)u(K^\mu, S^\mu) = 1. \quad (2.1)$$

The electron charge is denoted by  $-e$ , and the virtual photon is represented by the propagator  $D_F(Q)_{\mu\nu} = -g_{\mu\nu}/Q^2$ , with  $Q^2 \equiv -q_\mu q^\mu \geq 0$ .

The differential scattering cross section in the laboratory frame can then be written as [25, 26, 27]:

$$\begin{aligned} d\sigma &= \frac{1}{\beta} \frac{m_e}{\epsilon} \sum_{if} |\overline{\mathcal{M}}_{fi}|^2 \frac{m_e}{\epsilon'} \frac{d^3\vec{k}'}{(2\pi)^3} \frac{M_{A-1}}{E_{A-1}} \frac{d^3\vec{k}_{A-1}}{(2\pi)^3} \frac{M_f}{E_f} \frac{d^3\vec{k}_f}{(2\pi)^3} \\ &\quad \times (2\pi)^4 \delta^{(4)}(K^\mu + K_A^\mu - K'^\mu - K_{A-1}^\mu - K_f^\mu), \end{aligned} \quad (2.2)$$

where  $\beta = |\vec{k}|/\epsilon = |\vec{v}_e|$  and where  $\overline{\sum}$  corresponds to the appropriate average over initial states and sum over final states as will be discussed below. The corresponding

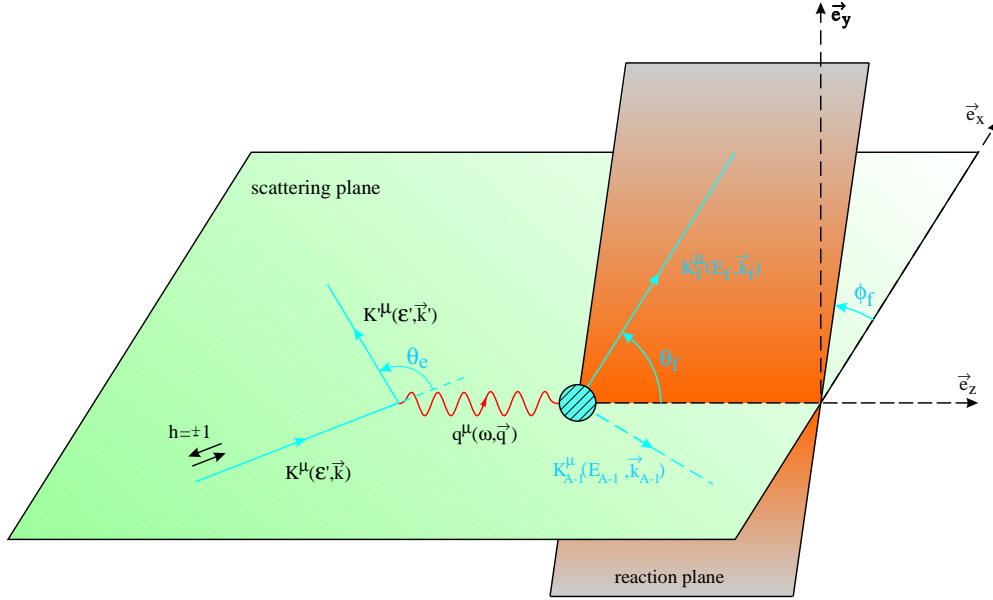


**Figure 2.1** Kinematics for the exclusive  $A(\vec{e}, \vec{e}'\vec{p})B$  scattering process. The scattering plane is defined by the electron momenta  $\vec{k}$  and  $\vec{k}'$ , and the  $xyz$  coordinate system is chosen such that the  $z$ -axis lies in the direction of the momentum transfer  $\vec{q}$ , the  $y$ -axis lies along  $\vec{k} \times \vec{k}'$  and the  $x$ -axis lies in the scattering plane; the reaction plane is then defined by  $\vec{k}_f$  and  $\vec{q}$ . The electron helicity  $h = +1$  and  $h = -1$  corresponds to the direction parallel and antiparallel to the electron beam, respectively.

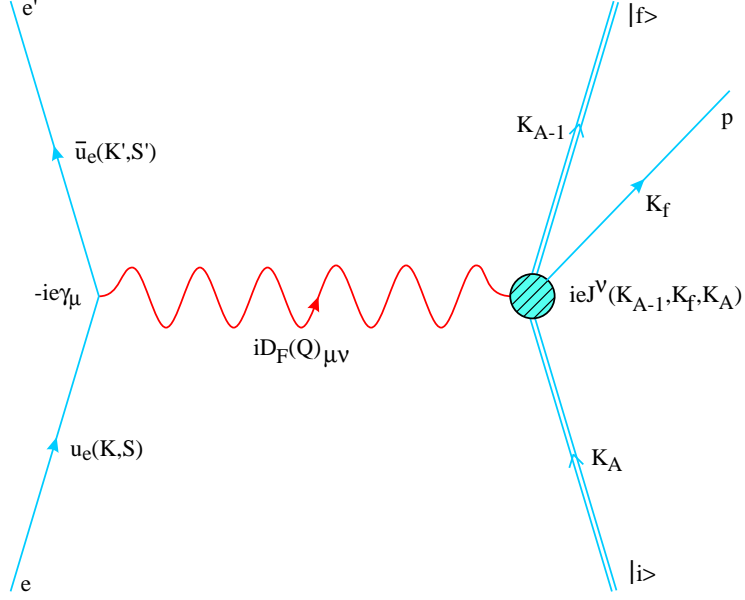


**Figure 2.2** Lowest order Feynman diagram for the exclusive  $A(\vec{e}, \vec{e}'\vec{p})B$  scattering process.  $J^\nu$  denotes the matrix element of the electromagnetic nuclear current operator between the initial and final hadronic states.

invariant matrix element  $\mathcal{M}_{fi}$  reads

$$\mathcal{M}_{fi} = \frac{ie}{Q^2} \left( \frac{\epsilon\epsilon'}{m_e^2} \right)^{1/2} j_e(K', S'; K, S)_\mu J^\mu(K_{A-1}, K_f; K_A)_{fi}, \quad (2.3)$$

with the electromagnetic current for the electron

$$j_e(K', S'; K, S)_\mu = -e \left( \frac{m_e^2}{\epsilon\epsilon'} \right)^{1/2} \bar{u}_e(K', S') \gamma_\mu u_e(K, S). \quad (2.4)$$

In the impulse approximation the nuclear electromagnetic current in momentum space  $J^\mu(K_{A-1}, K_f; K_A)_{fi} = J^\mu(Q)_{fi}$  can be written as

$$J^\mu(Q)_{fi} = \langle K_f S_f | \hat{J}^\mu | K_i S_i \rangle = \bar{u}_f \Gamma^\mu(K_f, K_i) u_i, \quad (2.5)$$

with  $\Gamma^\mu$  the electromagnetic vertex function for the nucleon and  $u_i$  ( $u_f$ ) the nucleon (distorted) spinors.

In the actual measurements, the momentum of the recoiling nucleus is not measured, while those of the electron and the ejected proton are. The recoil momentum can be eliminated from Eq. (2.2) through integration over  $\vec{k}_{A-1}$ . This results in the following fivefold differential cross section :

$$\frac{d^5\sigma}{d\epsilon' d\Omega_{e'} d\Omega_f} = \frac{m_e^2 M_f M_{A-1}}{(2\pi)^5 M_A} \frac{k' k_f}{k} f_{rec}^{-1} \sum_{if} |\mathcal{M}_{fi}|^2, \quad (2.6)$$

where  $f_{rec}$  is the hadronic recoil factor

$$f_{rec} = \frac{E_{A-1}}{E_A} \left| 1 + \frac{E_f}{E_{A-1}} \left( 1 - \frac{\vec{q} \cdot \vec{k}_f}{k_f^2} \right) \right| = \left| 1 + \frac{\omega k_f - q E_f \cos \theta_f}{M_A k_f} \right|, \quad (2.7)$$

with  $\theta_f$  the angle between  $\vec{k}_f$  and  $\vec{q}$  (see Fig. 2.1). The squared invariant matrix element  $\mathcal{M}_{fi}$  can be written as

$$\overline{\sum_{if}} |\mathcal{M}_{fi}|^2 = \frac{(4\pi\alpha)^2}{(Q^2)^2} \eta_e(K', S'; K, S)_{\mu\nu} W^{\mu\nu}(Q)_{fi}, \quad (2.8)$$

where the electron tensor  $\eta_e(K', S'; K, S)_{\mu\nu}$  is defined by

$$\eta_e(K', S'; K, S)_{\mu\nu} \equiv \overline{\sum_{if}} [\bar{u}_e(K', S') \gamma_\mu u_e(K, S)]^* [\bar{u}_e(K', S') \gamma_\nu u_e(K, S)], \quad (2.9)$$

and the nuclear tensor  $W^{\mu\nu}(Q)_{fi}$ , which contains all of the nuclear structure and dynamics information, is given by

$$W^{\mu\nu}(Q)_{fi} \equiv \overline{\sum_{if}} J^{\mu*}(Q)_{fi} J^\nu(Q)_{fi}. \quad (2.10)$$

As it is more difficult to measure the polarization of the scattered electron than it is to prepare a polarized electron beam, we will only consider the latter case from here on. Then, the differential cross section contains two terms :

$$\left( \frac{d^5\sigma}{d\epsilon' d\Omega_{e'} d\Omega_f} \right)_{fi}^h = \Sigma_{fi} + h\Delta_{fi}, \quad (2.11)$$

where  $h$  reduces to the electron helicity in the extreme relativistic limit (ERL,  $\epsilon \gg m_e$ ) for a longitudinally polarized beam. The first term  $\Sigma_{fi}$  is independent of the electron's polarization, and, would also occur if no polarizations were considered; the second term  $\Delta_{fi}$  occurs only if the initial beam is polarized.

In the most general case, the contraction of the electron tensor  $\eta_{\mu\nu}$  with the nuclear one  $W^{\mu\nu}$  results in an expression of the form [25]

$$4m_e^2 \eta_e(K', S'; K, S)_{\mu\nu} W^{\mu\nu}(Q)_{fi} = v_0 \sum_K V_K \mathcal{R}_{fi}^K, \quad (2.12)$$

where the label  $K$  takes on the values  $L, T, TT, TL, T', TL', \underline{TT}, \underline{TL}$  and  $\underline{TL}'$ . These labels refer to the longitudinal and transverse components of the virtual photon polarization, and hence correspond to the nuclear electromagnetic components with respect to the direction of  $\vec{q}$ . The  $\mathcal{R}_{fi}^{\underline{TT}}, \mathcal{R}_{fi}^{\underline{TL}}$  and  $\mathcal{R}_{fi}^{\underline{TL}'}$  terms do not vanish

for longitudinally polarized electron beams, but are suppressed by a factor  $m_e/\epsilon$ . Accordingly, these terms can be safely ignored. The various  $\mathcal{R}_{fi}^K$  are the nuclear response functions which contain all of the nuclear structure and dynamics information; the factor  $v_0 \equiv (\epsilon + \epsilon')^2 - q^2$  and the  $V_K$  are electron kinematics and polarization factors. In the ERL for the electrons, it can be shown [25, 26] that the differential cross section for the scattering of longitudinally polarized electrons from nuclei is given by

$$\begin{aligned} & \left( \frac{d^5\sigma}{d\epsilon' d\Omega_{e'} d\Omega_f} \right)_{fi}^h \\ &= \frac{MM_{A-1}k_f}{8\pi^3 M_A} f_{rec}^{-1} \sigma_M \left[ (v_L \mathcal{R}_L + v_T \mathcal{R}_T + v_{TT} \mathcal{R}_{TT} + v_{TL} \mathcal{R}_{TL}) \right. \\ & \quad \left. + h (v_{T'} \mathcal{R}_{T'} + v_{TL'} \mathcal{R}_{TL'}) \right], \end{aligned} \quad (2.13)$$

where  $\sigma_M$  is the well known Mott cross section

$$\sigma_M = \left( \frac{\alpha \cos \theta_e / 2}{2\epsilon \sin^2 \theta_e / 2} \right)^2, \quad (2.14)$$

with  $\theta_e$  the angle between the incident and the scattered electron. The electron kinematics is contained in the kinematical factors

$$v_L = \left( \frac{Q^2}{q^2} \right)^2, \quad (2.15)$$

$$v_T = \frac{1}{2} \left( \frac{Q^2}{q^2} \right) + \tan^2 \frac{\theta_e}{2}, \quad (2.16)$$

$$v_{TT} = -\frac{1}{2} \left( \frac{Q^2}{q^2} \right), \quad (2.17)$$

$$v_{TL} = -\frac{1}{\sqrt{2}} \left( \frac{Q^2}{q^2} \right) \sqrt{\left( \frac{Q^2}{q^2} \right) + \tan^2 \frac{\theta_e}{2}}, \quad (2.18)$$

$$v_{T'} = \tan \frac{\theta_e}{2} \sqrt{\left( \frac{Q^2}{q^2} \right) + \tan^2 \frac{\theta_e}{2}}, \quad (2.19)$$

$$v_{TL'} = -\frac{1}{\sqrt{2}} \left( \frac{Q^2}{q^2} \right) \tan \frac{\theta_e}{2}. \quad (2.20)$$

As for the contraction of the nuclear tensor with the electron tensor, we have that  $J^0(\vec{q})_{fi} = \rho(\vec{q})_{fi}$ , the Fourier transform of the transition charge density  $\langle f | \hat{\rho}(\vec{r}) | i \rangle$ , while

$$\vec{J}(\vec{q})_{fi} = \sum_{m=0,\pm 1} J(\vec{q}; m)_{fi} \vec{e}^*(\vec{q}; 1, m), \quad (2.21)$$

is the expansion of the Fourier transform of the transition three-current in terms of the standard unit spherical vectors  $\vec{e}(\vec{q}; 1, m)$  defined by

$$\vec{e}(\vec{q}; 1, 0) = \vec{e}_z \quad (2.22)$$

$$\vec{e}(\vec{q}; 1, \pm 1) = \mp \frac{1}{\sqrt{2}}(\vec{e}_x \pm i\vec{e}_y). \quad (2.23)$$

Furthermore, current conservation imposes that only three components of the four-current  $J^\mu$  are independent :

$$q_\mu J^\mu(\vec{q})_{fi} = \omega \rho(\vec{q})_{fi} - qJ(\vec{q}; 0)_{fi} = 0, \quad (2.24)$$

so that  $J(\vec{q}; 0)_{fi} = (\omega/q)\rho(\vec{q})_{fi}$ . The unpolarized structure functions are then defined in a standard fashion as

$$\mathcal{R}_{fi}^L = |\rho(\vec{q})_{fi}|^2, \quad (2.25)$$

$$\mathcal{R}_{fi}^T = |J(\vec{q}; +1)_{fi}|^2 + |J(\vec{q}; -1)_{fi}|^2, \quad (2.26)$$

$$\mathcal{R}_{fi}^{TT} = 2 \operatorname{Re} \{ J^*(\vec{q}; +1)_{fi} J(\vec{q}; -1)_{fi} \}, \quad (2.27)$$

$$\mathcal{R}_{fi}^{TL} = -2 \operatorname{Re} \{ \rho^*(\vec{q})_{fi} (J(\vec{q}; +1)_{fi} - J(\vec{q}; -1)_{fi}) \}. \quad (2.28)$$

Similarly, for the polarized structure functions we have

$$\mathcal{R}_{fi}^{T'} = |J(\vec{q}; +1)_{fi}|^2 - |J(\vec{q}; -1)_{fi}|^2, \quad (2.29)$$

$$\mathcal{R}_{fi}^{TL'} = -2 \operatorname{Re} \{ \rho^*(\vec{q})_{fi} (J(\vec{q}; +1)_{fi} + J(\vec{q}; -1)_{fi}) \}. \quad (2.30)$$

From here on one can proceed and perform a multipole expansion for the electromagnetic transition operators. At higher momentum transfer this method becomes cumbersome as a large amount of multipoles has to be considered. Therefore, we will not consider these expansions here, and proceed with the full transition operators.



---

## Chapter 3

# Relativistic Bound State Wave Functions

---

For many years, nuclear structure and the nucleon-nucleon interaction have been studied thoroughly within the context of the nonrelativistic Schrödinger framework. In this non-relativistic many-body theory, nuclei are regarded as bound states of nucleons interacting via two- and three-body potentials. The modern nucleon-nucleon potentials accommodate the exchange of mesons, as well as relativistic effects. Over the years, complex models for the structure of nuclei have been developed. Some of these models provide an accurate description of the ground-state properties of nuclei throughout the mass table.

There are a number of good arguments to prefer a relativistic description of nuclei above a nonrelativistic one. Firstly, in a field-theoretic approach the mesonic degrees of freedom can be implemented right at the start of the development of the model. Furthermore, causality, retardation, and relativistic kinematics can be incorporated in the most natural fashion. Note that the mean velocity of nucleons in a nucleus is approximately 25% of the velocity of light. The spin-orbit interaction, which is inserted by hand in non-relativistic approaches, emerges naturally in relativistic theories.

There are also less obvious benefits to be gained from a relativistic model. In Ref. [28] it is demonstrated that the one-pion contribution to the two-body potentials in the nonrelativistic approach is reduced severely by the nonlocalities, inherent to a relativistic description, which in turn has its effects on pion exchange currents. Furthermore, the boost interactions, which are naturally incorporated in a relativistic description, are proven to be responsible for over one third of the phenomenological part of the three-nucleon interaction needed in nonrelativistic Hamiltonians. There are also indications that the small nuclear binding energies arise from a cancellation between large Lorentz scalar and vector components. Since these potentials are comparable to the nucleon mass, it becomes essential to adopt a relativistic treatment.

A Dirac formalism based on these scalar and vector potentials, makes it possible to maintain a distinction between them.

Various relativistic models with varying degrees of accuracy have been developed up until now [29, 30, 31, 32, 33, 34]. One such an approach is based on a relativistic quantum field theory, where nucleons interact with one another by exchanging mesons, and was originally introduced by Walecka in Ref. [35].

### 3.1 Formalism

A relativistic quantum field theory for nucleons ( $\psi$ ) interacting with scalar mesons ( $\phi$ ) through a Yukawa coupling  $\bar{\psi}\psi\phi$  and with neutral vector mesons ( $V_\mu$ ) that couple to the conserved baryon current  $\bar{\psi}\gamma_\mu\psi$ , can be described through a lagrangian density of the type [16, 29, 36]

$$\begin{aligned} \mathcal{L}_0 = & \bar{\psi}(i\partial - M)\psi + \frac{1}{2}(\partial_\mu\phi\partial^\mu\phi - m_s^2\phi^2) - \frac{1}{4}G_{\mu\nu}G^{\mu\nu} \\ & + \frac{1}{2}m_v^2V_\mu V^\mu - g_v\bar{\psi}\gamma_\mu\psi V^\mu + g_s\bar{\psi}\psi\phi, \end{aligned} \quad (3.1)$$

with  $M$ ,  $m_s$  and  $m_v$  the nucleon, scalar meson and vector meson masses, respectively, and  $G^{\mu\nu} \equiv \partial^\mu V^\nu - \partial^\nu V^\mu$  the vector meson field strength. The scalar and vector fields may be associated with the  $\sigma$  and  $\omega$  mesons. The model can be extended to include also  $\pi$  and  $\rho$  mesons, as well as the coupling to the photon field. Then, the corresponding lagrangian has the form

$$\begin{aligned} \mathcal{L} = & \mathcal{L}_0 + \frac{1}{2}(\partial_\mu\vec{\pi} \cdot \partial^\mu\vec{\pi} - m_\pi^2\vec{\pi} \cdot \vec{\pi}) - ig_\pi\bar{\psi}\gamma_5\vec{\tau} \cdot \vec{\pi}\psi - \frac{1}{4}\vec{B}_{\mu\nu} \cdot \vec{B}^{\mu\nu} \\ & + \frac{1}{2}m_\rho^2\vec{b}_\mu \cdot \vec{b}^\mu - \frac{1}{2}g_\rho\bar{\psi}\gamma_\mu\vec{\tau} \cdot \vec{b}^\mu\psi - \frac{1}{4}F_{\mu\nu}F^{\mu\nu} - eA_\mu[\bar{\psi}\gamma^\mu\frac{1}{2}(1 + \tau_3)\psi \\ & + (\vec{b}_\nu \times \vec{B}^{\nu\mu})_3 + (\vec{\pi} \times (\partial^\mu\vec{\pi} + g_\rho(\vec{\pi} \times \vec{b}^\mu)))]_3. \end{aligned} \quad (3.2)$$

Here  $\vec{\pi}$ ,  $\vec{b}_\mu$  and  $A_\mu$  are the pion, rho and Maxwell fields, respectively, while  $\vec{B}^{\mu\nu} \equiv \partial^\mu\vec{b}^\nu - \partial^\nu\vec{b}^\mu - g_\rho(\vec{b}^\mu \times \vec{b}^\nu)$  is the  $\rho$  meson field strength and  $F_{\mu\nu}$  is the electromagnetic field strength. In the lagrangian of Eq. (3.2), higher order electromagnetic corrections and non-linear meson terms are omitted.

As discussed by Walecka in Ref. [35], the complete quantum field theory, which is a non-trivial problem, can be approximated by replacing the meson field operators with their expectation values at high densities. In infinite matter one then takes  $\langle \phi \rangle \equiv \phi_0$  and  $\langle V^\mu \rangle \equiv \delta^{\mu 0}V_0$ . This model can be extended to include the interactions of pions and  $\rho$  mesons [37]. The resulting mean-field theory may then be solved exactly.

In the relativistic Hartree approximation under study here, use is made of a coordinate-space Green's function approach to derive the relevant equations of motion (for details, see Refs. [16, 29]). Eventually one arrives at a theory similar in

content to the mean-field theory of Walecka, except that one is now working in a finite system. Hence, it can be shown that, when starting from the langrangian of Eq. (3.2), the following (static) Dirac equation for the baryon field  $\Psi_\alpha$  results [16] :

$$\left[ i\vec{\alpha} \cdot \vec{\nabla} + \gamma_0 M + \gamma_0 \Sigma_H(\vec{r}) \right] \psi_\alpha(\vec{r}) \equiv \hat{H} \psi_\alpha(\vec{r}) = \epsilon_\alpha \psi_\alpha(\vec{r}) , \quad (3.3)$$

where the self-energy  $\Sigma_H(\vec{r})$  is defined according to

$$\begin{aligned} \Sigma_H(\vec{r}) = & -g_s \phi_0(\vec{r}) + g_v \gamma_\mu V^\mu(\vec{r}) + g_\pi \gamma_5 \tau_\alpha \pi^\alpha(\vec{r}) + \frac{1}{2} g_\rho \gamma_\mu \tau_\alpha b^{\mu\alpha}(\vec{r}) \\ & + \frac{1}{2} \gamma_\mu (1 + \tau_3) A^\mu(\vec{r}) , \end{aligned} \quad (3.4)$$

and again only static field solutions were taken into consideration. Assuming further that the nuclear ground state is spherically symmetric and a parity eigenstate, it can be shown that the pion field does not enter in the Hartree approximation. Furthermore, the meson fields only depend on the radius  $r$ , and only the time component of the vector fields survives [16].

The general solutions to a Dirac equation with spherically symmetric potentials have the form

$$\psi_\alpha(\vec{r}) \equiv \psi_{n\kappa m t}(\vec{r}) = \begin{bmatrix} iG_{n\kappa t}(r)/r \mathcal{Y}_{\kappa m \eta t} \\ -F_{n\kappa t}(r)/r \mathcal{Y}_{-\kappa m \eta t} \end{bmatrix} , \quad (3.5)$$

where  $n$  denotes the principal,  $\kappa$  and  $m$  the generalized angular momentum and  $t$  the isospin quantum numbers. The  $\mathcal{Y}_{\pm\kappa m}$  are the well-known spin spherical harmonics and determine the angular and spin parts of the wavefunction :

$$\begin{aligned} \mathcal{Y}_{\kappa m} &= \sum_{m_l m_s} \langle l m_l \frac{1}{2} m_s | l \frac{1}{2} j m \rangle Y_{l, m_l} \chi_{\frac{1}{2} m_s} , \\ j &= |\kappa| - \frac{1}{2} , \quad l = \begin{cases} \kappa , & \kappa > 0 \\ -(\kappa + 1) , & \kappa < 0 . \end{cases} \end{aligned} \quad (3.6)$$

The Hartree approximation yields the following set of coupled equations for the different fields :

$$\begin{aligned} \frac{d^2}{dr^2} \phi_0(r) + \frac{2}{r} \frac{d}{dr} \phi_0(r) - m_s^2 \phi_0(r) &= -g_s \rho_s(r) \\ &\equiv -g_s \sum_{\alpha_{occ}} \left( \frac{2j_\alpha + 1}{4\pi r^2} \right) \left[ |G_\alpha(r)|^2 - |F_\alpha(r)|^2 \right] , \\ \frac{d^2}{dr^2} V_0(r) + \frac{2}{r} \frac{d}{dr} V_0(r) - m_v^2 V_0(r) &= -g_s \rho_B(r) \\ &\equiv -g_v \sum_{\alpha_{occ}} \left( \frac{2j_\alpha + 1}{4\pi r^2} \right) \left[ |G_\alpha(r)|^2 + |F_\alpha(r)|^2 \right] , \end{aligned}$$

Meson Mass	Coupling constant
$m_s = m_\sigma = 520$ MeV	$g_s^2 = 109.6$
$m_v = m_\omega = 783$ MeV	$g_v^2 = 190.4$
$m_\rho = 770$ MeV	$g_\rho^2 = 65.23$

**Table 3.1** Meson masses and coupling constants, as taken from Ref. [16].

$$\begin{aligned}
& \frac{d^2}{dr^2} b_0(r) + \frac{2}{r} \frac{d}{dr} b_0(r) - m_\rho^2 \phi_0(r) = -\frac{1}{2} g_\rho \rho_3(r) \\
& \equiv -\frac{1}{2} g_\rho \sum_{\alpha_{occ}} \left( \frac{2j_\alpha + 1}{4\pi r^2} \right) [ |G_\alpha(r)|^2 + |F_\alpha(r)|^2 ] (-1)^{t_\alpha - 1/2}, \\
& \frac{d^2}{dr^2} A_0(r) + \frac{2}{r} \frac{d}{dr} A_0(r) = -e \rho_P(r) \\
& \equiv -e \sum_{\alpha_{occ}} \left( \frac{2j_\alpha + 1}{4\pi r^2} \right) [ |G_\alpha(r)|^2 + |F_\alpha(r)|^2 ] (t_\alpha + \frac{1}{2}), \\
& \frac{d}{dr} G_\alpha(r) + \frac{\kappa}{r} G_\alpha(r) - [E_\alpha - g_v V_0(r) - t_\alpha g_\rho b_0(r) \\
& \quad - (t_\alpha + \frac{1}{2}) e A_0(r) + M - g_s \phi_0(r)] F_\alpha(r) = 0, \\
& \frac{d}{dr} F_\alpha(r) - \frac{\kappa}{r} F_\alpha(r) + [E_\alpha - g_v V_0(r) - t_\alpha g_\rho b_0(r) \\
& \quad - (t_\alpha + \frac{1}{2}) e A_0(r) - M + g_s \phi_0(r)] G_\alpha(r) = 0, \\
& \int_0^\infty dr (|G_\alpha|^2 + |F_\alpha|^2) = 1, \tag{3.7}
\end{aligned}$$

where  $\rho_s(r)$ ,  $\rho_B(r)$ ,  $\rho_3(r)$  and  $\rho_P(r)$  are the scalar, baryon, rho and proton densities, respectively. The above set of equations constitute the basis of the relativistic Hartree approach to the lagrangian of Eq. (3.2). This set depends on the meson and nucleon masses and coupling constants. Some of these can be taken directly from experiments ( $M_p$ ,  $M_n$ ,  $m_v = m_\omega$ ,  $m_\rho$ , and  $e^2$ ), others can be calculated by requiring that when the Dirac-Hartree equations are solved in the limit of infinite matter, relevant empirical equilibrium observables are reproduced. For all bound state wave functions that will be used in this work we have adopted the values quoted by Horowitz et al. in Ref. [16]. Table 3.1 shows the values for the coupling constants and meson masses quoted in this work.

## 3.2 Results

A new computer program to solve the set of coupled nonlinear differential equations of Eq. (3.7) was developed. Starting from an initial guess for the scalar and vector

	$^{12}\text{C}$		$^{16}\text{O}$	
	proton	neutron	proton	neutron
$1s_{1/2}$	36.47 MeV	39.98 MeV	35.09 MeV	39.22 MeV
$1p_{3/2}$	11.58 MeV	14.72 MeV	15.29 MeV	19.13 MeV
$1p_{1/2}$	-	-	7.94 MeV	11.67 MeV
B.E./nucl.	4.90 (7.42) MeV		5.85 (7.72) MeV	

**Table 3.2** Single particle energies in  $^{12}\text{C}$  and  $^{16}\text{O}$  for all occupied proton and neutron levels. The theoretical average binding energy per nucleon is compared to the experimental energy (in brackets).

potential in a Woods-Saxon form, the Dirac equations can be solved iteratively using a shooting point method, where one first integrates outward from small  $r$  to a chosen match radius  $r_m$  (the so-called shooting point), and then integrates inward from large  $r$  to  $r_m$ . Analytic solutions to the equations in the regions of large and small  $r$  allows one to impose the proper boundary conditions. The solutions are scaled so that  $G_\alpha$  is continuous at the shooting point  $r_m$ , and the wave function is then normalized to unity. The discontinuity in  $F_\alpha$  is then used to adjust the energy eigenvalue according to

$$\delta E_\alpha = -MG_\alpha(r_m)[F_\alpha(r_m^+) - F_\alpha(r_m^-)]. \quad (3.8)$$

This shooting procedure is repeated until  $|\delta E_\alpha|$  is less than a predefined tolerance. Once the nucleon wave functions are obtained, the densities and the meson fields can be reevaluated. Boundary conditions of exponential decay at large  $r$ , and vanishing slope for the fields at the origin were imposed.

For the  $^{12}\text{C}$  and  $^{16}\text{O}$  nuclei, the newly developed C-code **SOR** performed all integrations for a radial extension of the nucleus of 20 fm and a stepsize of 0.01 fm. The coupled Dirac equations were solved for a shooting point lying at 2 fm using a fourth-order Runge-Kutta algorithm. As a convergence criterion we imposed a tolerance level as small as 0.001 MeV on all single-particle energy levels.

In Table 3.2 the calculated neutron and proton single-particle energies in  $^{12}\text{C}$  and  $^{16}\text{O}$  are presented. A comparison of single-particle energy levels with experimental data is very ambiguous, so we only compare the average binding energy per nucleon with the empirical binding energies. The total energy of the system  $E$  is given by

$$E = \sum_{\alpha_{occ}} \epsilon_\alpha (2j_\alpha + 1) - \frac{1}{2} \int d\vec{r} [-g_s \phi_0(r) \rho_s(r) + g_v V_0(r) \rho_B(r) + \frac{1}{2} g_\rho b_0(r) \rho_3(r) + e A_0(r) \rho_P(r)]. \quad (3.9)$$

The computed densities for the  $^{12}\text{C}$  and  $^{16}\text{O}$  nuclei are depicted in Fig. 3.1. We

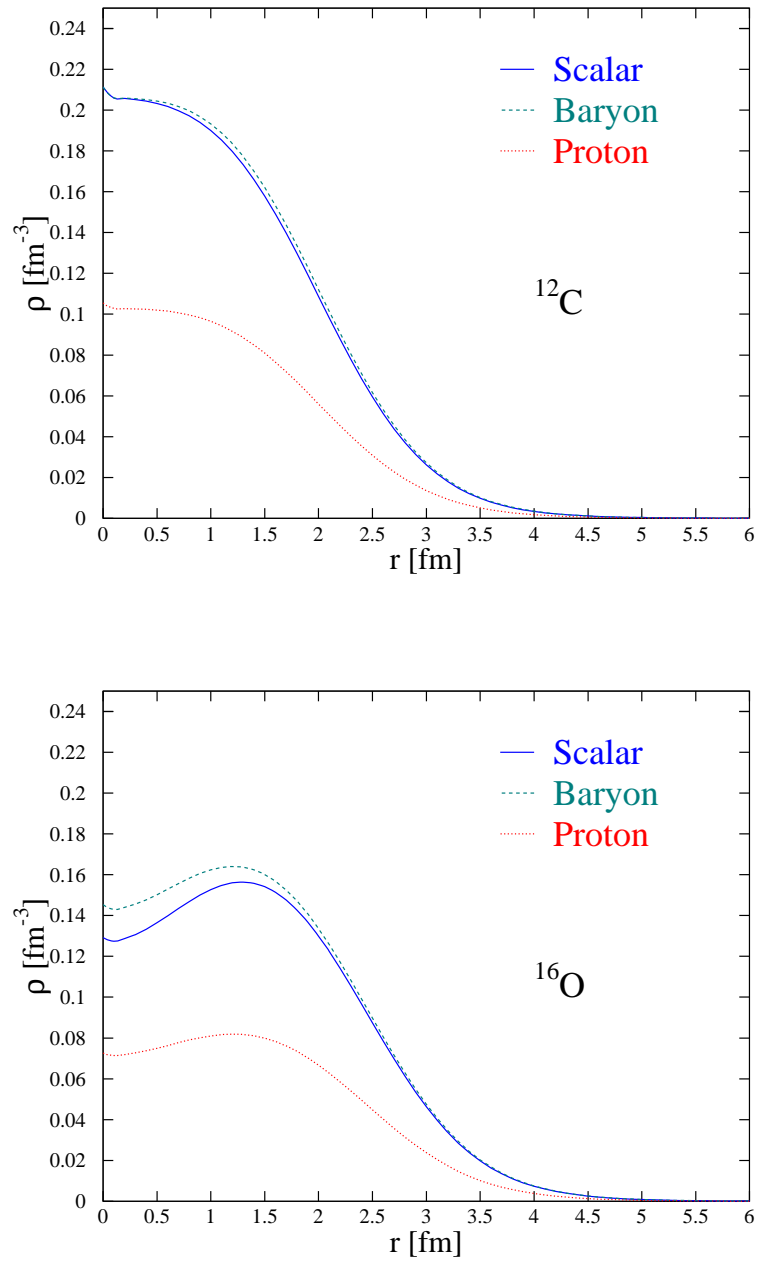


**Figure 3.1** The calculated scalar ( $\rho_s$ ), baryon ( $\rho_B$ ) and proton ( $\rho_P$ ) density distributions in the  $^{12}\text{C}$  and  $^{16}\text{O}$  nuclei. The rho density ( $\rho_3$ ) is not depicted as it is several orders of magnitudes smaller.

have verified that these results are comparable to those produced by the TIMORA code [16], which is widely used to solve the set of Eq. (3.7).

The scalar potential is entirely governed by the scalar meson field ( $\sigma$  meson), and is responsible for the attractive force that keeps the nucleons bound within the nucleus. The repulsive vector potential has contributions from the vector ( $\omega$  and  $\rho$ ) meson fields and the Maxwell field. It should be noted that the contributions from the  $\rho$  meson field and the Maxwell field are several orders of magnitude smaller than the contribution from the  $\omega$  meson field. Since the potential experienced by the neutrons differs only from the one experienced by the protons in these two minor terms, the total scalar and vector potentials for protons and neutrons are almost exactly the same. That is why we have only depicted the proton potentials in Fig. 3.2. These very same potentials will be used in Sec. 5 to derive the eikonal scattering states.

A point of high interest in nuclear physics are the nucleon spectral functions and momentum distributions. In calculating these contributions, we closely follow the method outlined in Ref. [38]. In free space the nucleon's motion is governed by the free particle solution of the Dirac equation. These plane wave states with momentum  $\vec{k}$  and energy  $\epsilon_k = \sqrt{k^2 + M^2}$  are given by

$$\phi_{\vec{k},s}(\vec{r}) = \sqrt{\frac{\epsilon_k + M}{2M}} \left[ \begin{array}{c} 1 \\ \frac{1}{E+M} \vec{\sigma} \cdot \vec{k} \end{array} \right] e^{i\vec{k} \cdot \vec{r}} \chi_{\frac{1}{2}m_s} . \quad (3.10)$$

Since the Dirac-Hartree potentials are spherically symmetric, we expand this free space solution in terms of the spin-spherical harmonics of Eq. (3.6) :

$$\begin{aligned} \phi_{\vec{k},s}(\vec{r}) &= \sqrt{\frac{\epsilon_k + M}{2M}} \sum_{\kappa m m_l} 4\pi (+i)^l \langle l m_l \frac{1}{2} m_s | l \frac{1}{2} j m \rangle \frac{Y_{lm_l}^*(\Omega_{\vec{k}})}{kr} \\ &\times \left[ \begin{array}{c} \nu g_{\kappa}(kr) \mathcal{Y}_{\kappa m} \\ -f_{\kappa}(kr) \mathcal{Y}_{-\kappa m} \end{array} \right] , \end{aligned} \quad (3.11)$$

where the usual spherical harmonics  $Y_{lm_l}$  are given in terms of the associated Legendre polynomials  $P_l^{m_l}$  :

$$Y_{lm_l}(\theta, \phi) = \sqrt{\frac{(2l+1)}{4\pi} \frac{(l-m_l)!}{(l+m_l)!}} (-1)^{m_l} e^{im_l\phi} P_l^{m_l}(\cos\theta) . \quad (3.12)$$

The radial components of the wave function are written in terms of Ricatti-Bessel functions (these are the spherical Bessel functions times their argument) :

$$\begin{aligned} g_{\kappa}(kr) &= \hat{j}_l(kr) \\ f_{\kappa}(kr) &= \frac{\pm k}{\epsilon_k + M} \hat{j}_{l\mp 1}(kr) , \end{aligned} \quad (3.13)$$

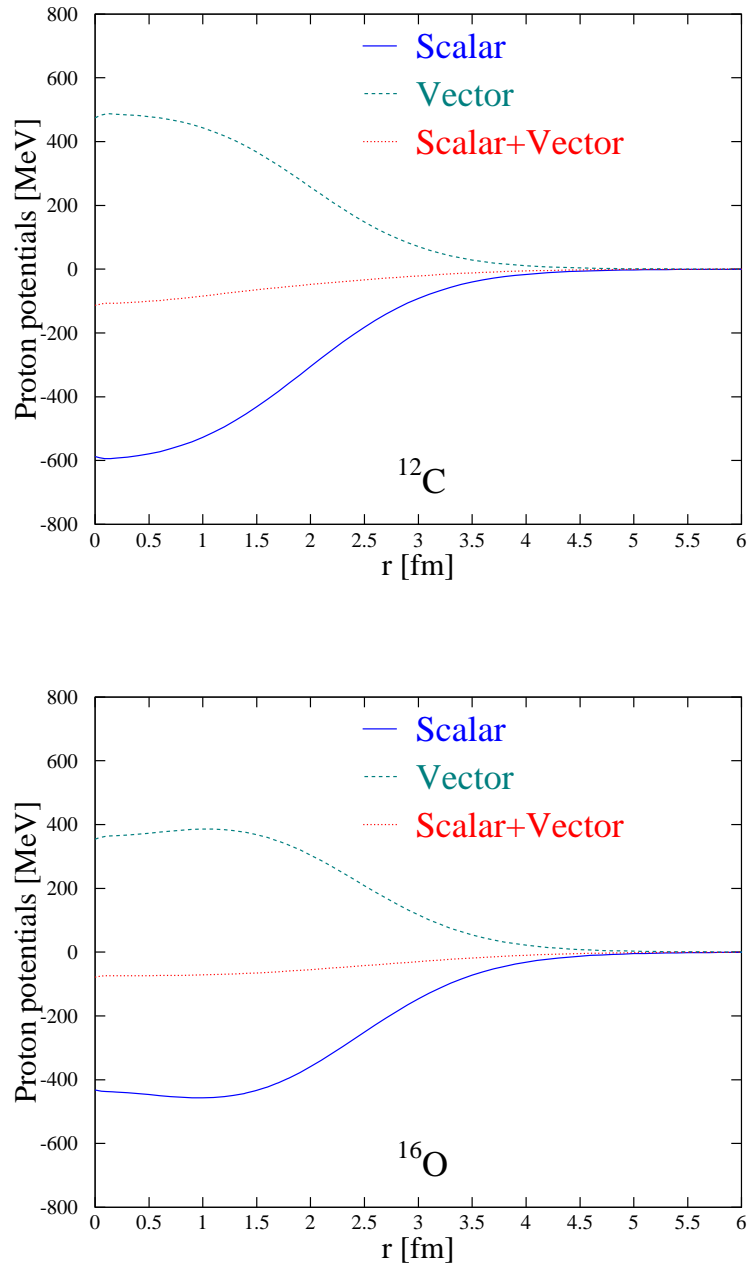


**Figure 3.2** The radial dependence of the scalar and vector proton potentials as obtained from relativistic Hartree calculations for  $^{12}\text{C}$  and  $^{16}\text{O}$ . The neutron potentials are quasi identical to those of the proton's and have not been plotted.

where the positive (negative) sign corresponds to  $\kappa > 0$  ( $\kappa < 0$ ). The overlap between a free plane wave spinor characterized by a momentum  $\vec{k}$  and the mean-field eigenstates of Eq. (3.5), summed over all spin projections, is then given by

$$\rho_{\vec{k},\epsilon,\kappa} \equiv \sum_{m_s,m} \left| \int d\vec{r} \phi_{\vec{k},s}^\dagger(\vec{r}) \psi_{\epsilon\kappa m}(\vec{r}) \right|^2. \quad (3.14)$$

Making use of the following identity :

$$\sum_{m=-j}^j \mathcal{Y}_{\kappa m}^\dagger \mathcal{Y}_{\kappa' m} = \left( \frac{2j+1}{4\pi} \right) \delta_{\kappa\kappa'}, \quad \kappa' = \pm\kappa, \quad (3.15)$$

we finally arrive at the following expression for the nucleonic momentum distribution :

$$\rho_{\vec{k},\epsilon,\kappa} = (2j+1) \left( \frac{1}{2\pi^2 k^2} \right) \left( \frac{\epsilon_k + M}{2M} \right) |G_{\epsilon\kappa}(k) + F_{\epsilon\kappa}(k)|^2, \quad (3.16)$$

where

$$\begin{aligned} G_{\epsilon\kappa}(k) &= \int_0^\infty dr G_{\epsilon\kappa}(r) g_\kappa(kr), \\ F_{\epsilon\kappa}(k) &= \int_0^\infty dr F_{\epsilon\kappa}(r) f_\kappa(kr), \end{aligned} \quad (3.17)$$

are the Fourier transforms of the radial components of the bound state wave function. Eq. (3.16) can be seen as the relativistic generalization of the nucleon momentum distribution.

Fig. 3.3 shows the momentum distributions for all occupied levels in  $^{12}\text{C}$  and  $^{16}\text{O}$ . Since the proton and neutron results can be hardly distinguished from each other, the latter are not shown.

The nucleon momentum distributions are subject to sizeable corrections when correlations beyond the mean-field Hartree approach are implemented. In an uncorrelated Fermi gas all states up to the Fermi momentum  $k_F$  are occupied, and the states above  $k_F$  remain empty. In a correlated system, states below the Fermi surface become partially depleted and states above the Fermi surface get a non-vanishing occupation probability. The nucleon-nucleon correlations are mainly induced by the short-range and tensor components of the nucleon-nucleon interaction. Evidence for the depletion of the single-particle states was obtained from the analysis of (e,e'p) reactions for a large number of target nuclei [1].

Another possible source for the fragmentation of the single-particle strength is the mixing between the positive and negative energy states, or, equivalently, between particles and antiparticles [38]. For small values of the momenta ( $k < 300$  MeV/c), it has been shown that the nucleon spectral function is dominated by positive energy

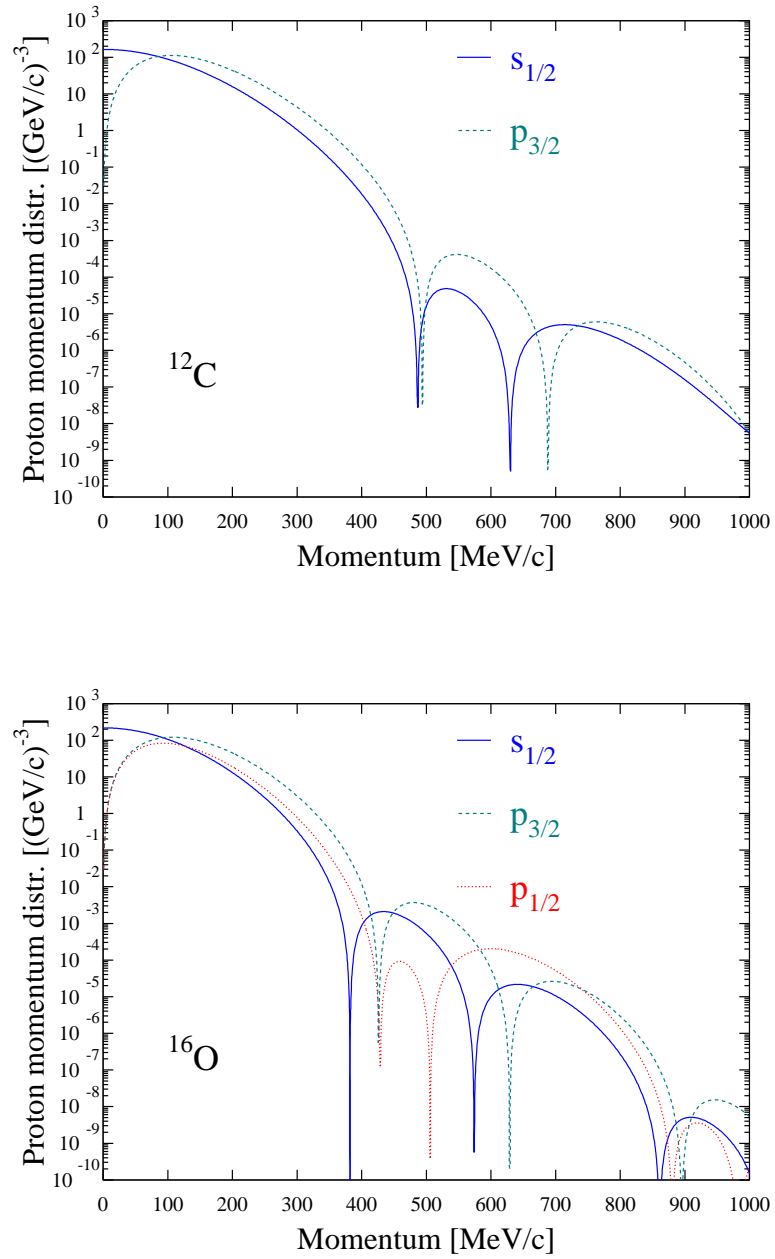


**Figure 3.3** The proton momentum distributions for the different single particle states in the  $^{12}\text{C}$  and  $^{16}\text{O}$  nuclei. The neutron momentum distributions are almost identical, and are not shown.

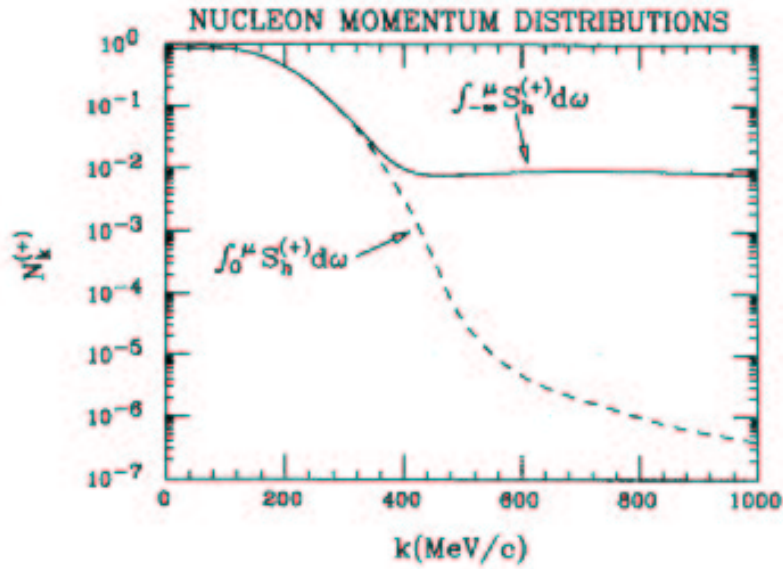


**Figure 3.4** Nucleon momentum distributions for  $^{16}\text{O}$  including (solid line) and neglecting (dashed line) the contribution from negative-energy states. This picture was taken from Ref. [38].

states close to the Fermi energy. In contrast, the high momentum components ( $k > 500$  MeV/c) are driven almost entirely by high-lying excitations located 1-2 GeV away from the Fermi surface. The presence of these negative energy states gives rise to high momentum components that are four orders of magnitude larger than would have otherwise been in the absence of negative energy states. The nucleon momentum distributions for  $^{16}\text{O}$  calculated in such a way, is represented in Fig. 3.4.



---

## Chapter 4

# Off-Shell Electron-Proton Coupling

---

The scattering process of an electron on a free (or, on-shell) nucleon can be computed in a model-independent fashion. The electromagnetic coupling on a bound (or, off-shell) nucleon, on the other hand, is not free of ambiguities. For one, it is believed that the electromagnetic vertices for off-shell nucleons have a more complicated structure than for free nucleons. This elusive feature is known as the Gordon ambiguity and there has been a string of papers that have addressed this issue [39, 40, 41, 42] resulting in a number of recipes for the form of the off-shell electron-proton coupling.

Another equally important issue, that is closely related to the Gordon ambiguity, is the gauge invariance of the electromagnetic current in many-body systems. This topic is closely related to the condition that the electromagnetic current should be conserved. In trying to describe the nuclear reaction by means of the free electromagnetic current, one is forced to make certain assumptions. These assumptions lead the off-shell nucleons to affect the nuclear current in such a way that current conservation is lost. As discussed in many works [41, 42, 43, 44, 45], some arbitrariness, often referred to as the “off-shell ambiguity”, surrounds the choice for the functional form of the electromagnetic vertex function  $\Gamma^\mu$  for a bound nucleon. There exists no uniquely defined procedure to remedy this unphysical feature and one is forced to introduce ad hoc prescriptions to restore current conservation, as will be discussed below.

We express the matrix elements of the nucleon current in the usual form

$$\langle K_f S_f | J^\mu | K_i S_i \rangle = \bar{u}_f \Gamma^\mu(K_f, K_i) u_i, \quad (4.1)$$

where  $\Gamma^\mu$  is the electromagnetic vertex function for the nucleon and  $u_i$  ( $u_f$ ) are the nucleon spinors. For a free nucleon,  $\Gamma^\mu$  can be expressed in several fully equivalent

forms

$$\Gamma_{cc1}^\mu = G_M(Q^2)\gamma^\mu - \frac{\kappa}{2M}F_2(Q^2)(K_i^\mu + K_f^\mu), \quad (4.2)$$

$$\Gamma_{cc2}^\mu = F_1(Q^2)\gamma^\mu + i\frac{\kappa}{2M}F_2(Q^2)\sigma^{\mu\nu}q_\nu, \quad (4.3)$$

$$\Gamma_{cc3}^\mu = \frac{1}{2M}F_1(Q^2)(K_i^\mu + K_f^\mu) + i\frac{1}{2M}G_M(Q^2)\sigma^{\mu\nu}q_\nu, \quad (4.4)$$

where  $F_1$  is the Dirac,  $F_2$  the Pauli form factor and  $\kappa$  is the anomalous magnetic moment. The relation with the Sachs electric and magnetic form factors is established through the relations  $G_E = F_1 - \tau\kappa F_2$  and  $G_M = F_1 + \kappa F_2$ , with  $\tau \equiv Q^2/4m^2$ .

When considering bound (or, “off-shell”) nucleons, however, the above vertex functions can no longer be guaranteed to produce the same results. As a matter of fact, explicit current conservation is rather an exception than a rule in most calculations that deal with  $(e, e'p)$  reactions from finite nuclei. In nuclear physics, the most widely used procedure to “effectively” restore current conservation is based on modifying the longitudinal component of the nuclear vector current using the substitution

$$J_3 \rightarrow \frac{\omega}{q}J_0. \quad (4.5)$$

The four-current then becomes

$$J_\mu = (J_0, J_1, J_2, \frac{\omega J_0}{q}). \quad (4.6)$$

This procedure is partly inspired on the observation that meson-exchange and isobar terms enter the charge current operator in a higher relativistic order than they used to do for the vector current. There exist several other prescriptions which are meant to restore current conservation. Along similar lines, the charge operator can be replaced by

$$J_0 \rightarrow \frac{q}{\omega}J_3, \quad (4.7)$$

and the four-current can be rewritten as

$$J_\mu = (\frac{qJ_3}{\omega}, J_1, J_2, J_3). \quad (4.8)$$

In other recipes one adds a term proportional to  $q^\mu$  to obtain a divergence free current [46] :

$$J_\mu \rightarrow J_\mu + \frac{J_\nu q^\nu}{Q^2}q_\mu. \quad (4.9)$$

One can also construct a vertex function that guarantees current conservation for any initial and final nucleon state. This can be achieved for example by adding an extra term to the vertex [47]

$$\Gamma_{DON}^\mu = F_1(Q^2)\gamma^\mu + i\frac{\kappa}{2M}F_2(Q^2)\sigma^{\mu\nu}q_\nu + F_1(Q^2)\frac{\not{q}q^\mu}{Q^2}, \quad (4.10)$$

which is also equivalent to the Eqs. (4.2) - (4.4) in the free nucleon case. An operator derived from the generalized Ward-Takahashi identity reads [44]

$$\Gamma_{WT}^\mu = \gamma^\mu - i\frac{\kappa}{2M}F_2(Q^2)\sigma^{\mu\nu}q_\nu + [F_1(Q^2) - 1]\frac{\not{q}q^\mu + Q^2\gamma^\mu}{Q^2}. \quad (4.11)$$

We now proceed with putting the above-mentioned recipes in a more fundamental context. We write the transition matrix element corresponding with the electron scattering process in the general form

$$M = j^\mu \Pi_{\mu\nu} J^\nu, \quad (4.12)$$

where  $\Pi_{\mu\nu}$  is the photon propagator and  $j^\mu$  the electron current. The explicit form of the propagator is gauge dependent, and, consequently, so is the matrix element. In the covariant class of gauges one has that

$$M_{\text{Lorentz}} = \frac{i}{Q^2} \left( j_\mu J^\mu + (1 - \xi) \frac{(q_\mu J^\mu)(q_\mu j^\mu)}{Q^2} \right), \quad (4.13)$$

where  $\xi$  is a free gauge parameter.

Usually one works in the so-called Feynman gauge, where  $\xi$  is set equal to 1. In this case, the matrix element reduces to

$$M_{\text{Feynman}} = \frac{i}{Q^2} j_\mu J^\mu. \quad (4.14)$$

The equation (4.14) holds always true in a covariant Lorentz gauge since the electron current  $j$  is conserved. A choice of one or another gauge should have no effect on the results. In calculations dealing with finite nuclei however, the occurrence of current non-conserving terms cannot be excluded, so that the different gauge possibilities may eventually affect the predictions. We will now show that the prescriptions of Eqs. (4.5), (4.7) and (4.9) are connected to different gauge choices.

In the frequently adopted Coulomb gauge, which is a noncovariant gauge, the matrix element of Eq. (4.12) is written as

$$M_{\text{Coulomb}} = \frac{i}{q^2} j_0 J_0 - \frac{i}{Q^2} \left( \vec{j} \cdot \vec{J} - \frac{(\vec{q} \cdot \vec{J})(\vec{q} \cdot \vec{j})}{q^2} \right). \quad (4.15)$$

This is the same matrix element one would obtain in the Feynman gauge when using the replacement given in Eq. (4.5). Another noncovariant gauge, the Weyl, or temporal, gauge defines the matrix element as

$$M_{\text{Weyl}} = -\frac{i}{Q^2} \left( \vec{j} \cdot \vec{J} - \frac{(\vec{q} \cdot \vec{J})(\vec{q} \cdot \vec{j})}{\omega^2} \right). \quad (4.16)$$

Similarly, this expression is obtained from Eq. (4.14) upon replacement of Eq. (4.7). The substitution of Eq. (4.9) is simply obtained by setting the gauge parameter  $\xi$  equal to zero in Eq. (4.13); this is the so-called Landau gauge. And again, the same expression is found upon substituting the recipe of Eq. (4.9) into Eq. (4.14). For the prescription of Eq. (4.10) there is no deeper-lying justification on the basis of the most general covariant expression of Eq. (4.13).

The electromagnetic vertex function of Eq. (4.11) is based on the following. It is shown in Ref. [44] that the electromagnetic interactions of any two-body system (i.e. electron-proton system) described by a relativistic two-body equation will always conserve current provided that the following conditions are met

- the electromagnetic currents for the interacting off-shell nucleons (and mesons) satisfy the appropriate Ward-Takahashi identity
- the interacting incoming and outgoing two-body system satisfies the same two-body relativistic equation
- the interaction current is built up from the relativistic kernel by coupling the virtual photon to all possible places (or possible orders) in the kernel

It is obvious that in a many-body calculation not all of these conditions can be met, so that the occurrence of current non-conserving terms becomes almost unavoidable. In analogy with the CC1 and CC2 current operators, we have chosen to restore current conservation by means of the recipes of Eqs. (4.5) and (4.7).

In Sec. 7 we will focus on the uncertainties induced by the off-shell effects and quantify the importance of these ambiguities for the description of the  $A(e, e'p)$  process at various energy scales.

Another issue of current interest related to the off-shellness of nucleons, is the question whether the electromagnetic form factors are modified by the presence of a nuclear medium. In Ref. [40] variations due to the off-shellness of the proton were found up to 10 % relative to the on-shell form factors for intermediate energy kinematics. When going off-shell the magnitudes of the form factors are generally increased, and, consequently so are the cross sections. On the other hand it was found that the ratio of the form factors  $G_M/G_E$  was rather insensitive to off-shell effects.

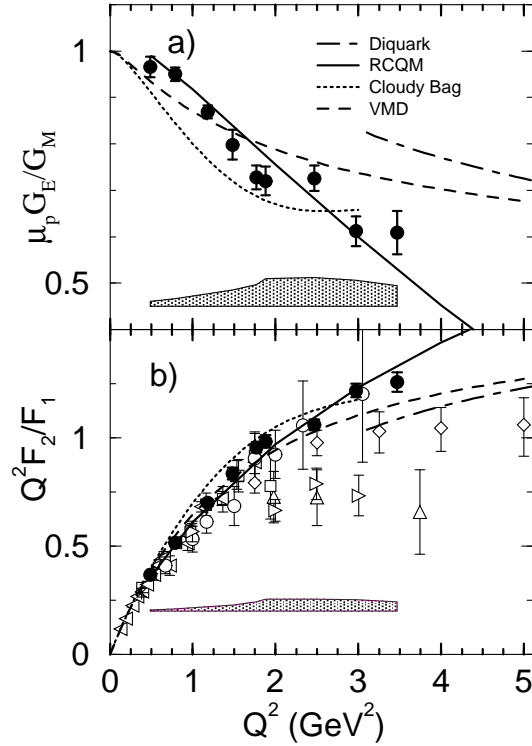


**Figure 4.1** The upper panel shows the ratio  $\mu_p G_{E_p} / G_{M_p}$  from the experiment of Ref. [48], compared with theoretical calculations. The lower panel shows the ratio  $Q^2 F_{2_p} / F_{1_p}$  compared to the same calculations and world data (non-black symbols). This figure was taken from Ref. [48].

Perhaps more important when studying high energy ( $e, e'p$ ) reactions is the  $Q^2$  evolution of this ratio. It has long been thought that the ratio  $\mu_p G_{E_p} / G_{M_p}$  equals 1. With the advent of high duty facilities and the powerful technique of polarization transfer, measurements of nucleonic form factors have been performed with unprecedented accuracy. One such measurement of the free proton's form factors was performed at JLAB [48] and the results are contained in Fig. 4.1. The most important feature of the data is the sharp decrease of the ratio  $\mu_p G_{E_p} / G_{M_p}$  as  $Q^2$  increases, which indicates that  $G_{E_p}$  falls more rapidly with  $Q^2$  than  $G_{M_p}$ . The  $Q^2 F_{2_p} / F_{1_p}$  ratio indicates a continuing increase with  $Q^2$ , also in contradiction with earlier observations. Some QCD-based quark models are able to sustain this  $Q^2$  evolution of the form factors, and it is hoped that these measurements may shed some light on the problem of nucleon spin.



---

## Chapter 5

# The Eikonal Final State

---

In the description of photoinduced breakup reactions, semi-classical methods become useful whenever the de Broglie wavelength  $\lambda = h/k$  of the ejected particle with momentum  $k$  is sufficiently short compared with the distance in which the potential varies appreciably. The eikonal approximation, which finds its origins in optics, belongs to the class of semi-classical methods. If the potential varies smoothly and has a range  $a$ , this short wavelength condition is equivalent to the requirement that  $ka \gg 1$ . Referring to the potentials of Fig. 3.2, it is clear that the potentials vary smoothly and have an approximate range of 2-3 fm. The condition to be fulfilled can then be written as  $k \gg 500$  MeV/c, what will be the case in our discussion of the performed calculations.

For  $A(e, e'p)$  reactions with proton kinetic energies  $T_p \geq 500$  MeV/c a relativistic description is a prerequisite. Originally, the gap between the low and the intermediate/high energy range was bridged by a distorted wave formalism, where a broad basis of Dirac eigenstates are joined in a coherent manner to construct the final distorted scattering state [49, 50, 51]. In principle, this method allows to solve the Dirac equation for the scattered particle exactly. As already mentioned in the introduction of this work this method can no longer be applied at higher energies, say a few GeV. As one goes higher in energies, one needs an increasingly larger base of plane wave solutions to reach a certain point of convergence, and, unfortunately, this procedure gets increasingly more tedious and the numerical stability gets out of hand. Since we want to develop a relativistic model that makes use of (optical) scattering potentials, and still remains valid for higher values of  $Q^2$ , we need another way to describe the scattering problem.

Fortunately, an alternative is offered by the eikonal method, and its multiple-scattering extension, which was developed by Glauber [5]. This technique is primarily based on the observation that at high energies, pp reactions become highly diffractive, implying that they are extremely forwardly peaked.

In this chapter, we will first briefly review the relativistic distorted wave impulse

approximation (RDWIA). Next, we will introduce a consistent relativistic model for the description of  $A(e, e'p)$  processes in the eikonal approximation. With the term “consistent” we refer to a procedure in which the bound and scattering states are derived from the same Dirac equation. The consistent approach possesses the virtue of obeying orthogonality and unitarity constraints but will soon be observed to provide poor descriptions of the experimental data. In a next step, we will improve our model by implementing complex optical potentials for the description of proton distortion in the final state. Finally, we develop a scheme that allows to perform fully relativistic and unfactorized  $A(e, e'p)$  calculations in a Glauber multiple-scattering framework.

## 5.1 The Relativistic Distorted Wave Approximation

We will now briefly outline the RDWIA scheme to solve the Dirac equation of Eq. (3.3). Within a relativistic framework the bound state wave functions with well defined angular quantum numbers  $\kappa$  and  $m$  were of the form

$$\psi_{n\kappa m}(\vec{r}) = \begin{bmatrix} iG_{n\kappa t}(r)/r \mathcal{Y}_{\kappa m} \\ -F_{n\kappa t}(r)/r \mathcal{Y}_{-\kappa m} \end{bmatrix}. \quad (5.1)$$

These solutions are eigenstates of the total Hamiltonian and the total angular momentum with eigenvalue  $j = |\kappa| - 1/2$ ,

$$\begin{aligned} \mathcal{Y}_{\kappa m} &= \sum_{m_l m_s} \langle l m_l \frac{1}{2} m_s | l \frac{1}{2} j m \rangle Y_{l, m_l} \chi_{\frac{1}{2} m_s}, \\ j &= |\kappa| - \frac{1}{2}, \quad l = \begin{cases} \kappa, & \kappa > 0 \\ -(\kappa + 1), & \kappa < 0. \end{cases} \end{aligned} \quad (5.2)$$

The wave function for the outgoing proton  $\Psi_f$  is a scattering solution of the same Dirac equation of Eq. (3.3). In the RDWIA approach it is obtained as a partial wave expansion in configuration space [17, 18, 52, 53],

$$\Psi_f(\vec{r}) = 4\pi \sqrt{\frac{E_f + M}{2M}} \sum_{\kappa, m, m_l} e^{-i\delta_\kappa^*} \langle l m_l \frac{1}{2} m_s | l \frac{1}{2} j m \rangle Y_{l m_l}^*(\hat{k}_f) \psi_{\kappa m}(\vec{r}). \quad (5.3)$$

The phase shifts  $\delta_\kappa$  are calculated with a procedure as for example outlined in Ref. [54]. Basically, one expresses the incident, or bound, wave as a sum of partial waves and one can then compare the asymptotic radial functions of Eq. (5.3) with this plane wave expansion to determine the phase-shifts.

## 5.2 A Consistent Approach to Final State Interactions

To construct the scattering states for the ejected nucleons, we start from the Hamiltonian that was already used to calculate the bound state wave functions

$$\hat{H} \equiv -i\vec{\alpha} \cdot \vec{\nabla} + \gamma^0 M + \gamma^0 \Sigma_H(r), \quad (5.4)$$

where the self-energy  $\Sigma_H(r)$  is determined by

$$\begin{aligned} \Sigma_H(r) = & -g_s \phi_0(r) + g_v \gamma_0 V^0(r) + \frac{1}{2} g_\rho \gamma_0 \tau_\alpha b^{0\alpha}(r) + \\ & \frac{1}{2} e \gamma_0 (1 + \tau_3) A^0(r), \end{aligned} \quad (5.5)$$

and where the pion terms have been dropped. With the formal substitutions

$$\begin{aligned} V_s(r) & \equiv -g_s \phi_0, \\ V_v(r) & \equiv g_v V_0(r) + \frac{1}{2} g_\rho b_0(r) (-1)^{t_\alpha - 1/2} + e A_0(r) (t_\alpha + \frac{1}{2}), \end{aligned} \quad (5.6)$$

the time independent Dirac equation for a projectile with relativistic energy  $E = \sqrt{k^2 + M^2}$  and spin state  $s$ , can be cast in the form

$$\hat{H} \Psi_{\vec{k},s}^{(+)} = E \Psi_{\vec{k},s}^{(+)} = [\vec{\alpha} \cdot \vec{p} + \beta M + \beta V_s(r) + V_v(r)] \Psi_{\vec{k},s}^{(+)}, \quad (5.7)$$

where we have introduced the notation  $\Psi_{\vec{k},s}^{(+)}$  for the unbound Dirac states. After some straightforward manipulations, a Schrödinger-like equation for the upper component can be obtained

$$\left[ -\frac{\hbar^2 \nabla^2}{2M} + V_c + V_{so}(\vec{\sigma} \cdot \vec{L} - i\vec{r} \cdot \vec{p}) \right] u_{\vec{k},s}^{(+)} = \frac{k^2}{2M} u_{\vec{k},s}^{(+)}, \quad (5.8)$$

where the central and spin orbit potentials  $V_c$  and  $V_{so}$  are defined as

$$\begin{aligned} V_c(r) & = V_s(r) + \frac{E}{M} V_v(r) + \frac{V_s(r)^2 - V_v(r)^2}{2M}, \\ V_{so}(r) & = \frac{1}{2M[E + M + V_s(r) - V_v(r)]} \frac{1}{r} \frac{d}{dr} [V_v(r) - V_s(r)]. \end{aligned} \quad (5.9)$$

In computing the scattering wave functions, we use the scalar and vector potentials as they are determined in the iterative bound state calculations. As a result the initial and final state wave functions are orthogonalized and no spurious contributions are expected to enter the calculated cross sections.

Since the lower component is related to the upper one through

$$w_{\vec{k},s}^{(+)} = \frac{1}{E + M + V_s - V_v} \vec{\sigma} \cdot \vec{p} u_{\vec{k},s}^{(+)}, \quad (5.10)$$

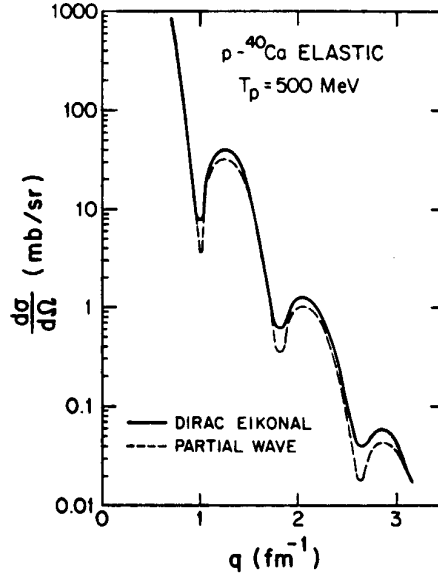


**Figure 5.1** The 500 MeV  $p$ - $^{40}\text{Ca}$  elastic scattering cross section at  $T_p = 500$  MeV, calculated using the Dirac eikonal method of Ref. [57] (solid line) compared to that using a Dirac partial wave code (dashed line). This picture was taken from Ref. [57].

the solutions to the equation (5.8) determine the complete relativistic eigenvalue problem.

So far no approximations have been made. Various groups [17, 18, 55] have solved a Dirac equation of the type (5.8) for the final scattering state using Dirac optical potentials derived from global fits to elastic proton scattering data [56]. Not only are global parametrizations of Dirac optical potentials usually restricted to proton kinetic energies  $T_p \leq 1$  GeV, calculations based on exact solutions of the Dirac equation frequently become impractical at higher energies. This is particularly the case for approaches that rely on partial-wave expansions in determining the transition matrix elements. To overcome these complications, we solve the Dirac equation (5.8) in the eikonal limit [57, 58, 59, 60]. In intermediate-energy proton scattering ( $T_p \approx 500$  MeV) the eikonal approximation was shown to reproduce fairly well the exact Dirac partial wave results as can be seen from Fig. 5.1 [57].

Following the discussion of Ref. [57], we define the average momentum  $\vec{K}$  and the momentum transfer  $\vec{q}$  in terms of the projected initial ( $\vec{k}_i$ ) and final momentum ( $\vec{k}_f$ ) of the ejectile

$$\vec{q} = \vec{k}_f - \vec{k}_i, \quad (5.11)$$

$$\vec{K} = \frac{1}{2}(\vec{k}_f + \vec{q}). \quad (5.12)$$

In the eikonal, or, equivalently, the small-angle approximation ( $q \gg k_i$ ), the following operatorial substitution is made in computing the scattering wave function

$$p^2 = [(\vec{p} - \vec{K}) + \vec{K}]^2 \longrightarrow 2\vec{K} \cdot \vec{p} - K^2. \quad (5.13)$$

After introducing this approximate relation, the Dirac equation for the upper component (5.8) becomes

$$[-i\vec{K} \cdot \vec{\nabla} - K^2 + M(V_c + V_{so}[\vec{\sigma} \cdot (\vec{r} \times \vec{K}) - i\vec{r} \cdot \vec{K}])]u_{\vec{k},s}^{(+)} = 0, \quad (5.14)$$

where the momentum operators in the spin orbit and Darwin terms are substituted by  $\vec{K}$ . Remark that the above equation is now linear in the momentum operator. In the eikonal limit, the scattering wave functions take on the form

$$u_{\vec{k},s}^{(+)} = e^{i\vec{k} \cdot \vec{r}} e^{iS(\vec{r})} \chi_{\frac{1}{2}m_s}. \quad (5.15)$$

Inserting this into Eq. (5.14), yields an expression for the eikonal phase [59]. Defining the  $z$ -axis along the direction of the average momentum  $\vec{K}$ , this phase can be written in an integral form as

$$iS(\vec{b}, z) = -i\frac{M}{K} \int_{-\infty}^z dz' [V_c(\vec{b}, z') + V_{so}(\vec{b}, z')[\vec{\sigma} \cdot (\vec{b} \times \vec{K}) - iKz']], \quad (5.16)$$

where we have introduced the notation  $\vec{r} \equiv (\vec{b}, z)$ . The scattering wave function, which is proportional to

$$\psi_{\vec{k},s}^{(+)} \sim \left[ \frac{1}{E+M+V_s-V_v} \vec{\sigma} \cdot \vec{p} \right] e^{i\vec{k} \cdot \vec{r}} e^{iS(\vec{r})} \chi_{\frac{1}{2}m_s}, \quad (5.17)$$

is normalized such that

$$\lim_{\vec{r} \rightarrow -\infty} \phi_{\vec{k},s}^{(+)} = \phi_{\vec{k},s}^{PWIA}(\vec{r}) = \sqrt{\frac{E+M}{2M}} \left[ \frac{1}{E+M} \vec{\sigma} \cdot \vec{p} \right] e^{i\vec{k} \cdot \vec{r}} \chi_{\frac{1}{2}m_s}. \quad (5.18)$$

The scattering wave function from Eq. (5.17) differs from the plane wave solution in two respects. First, the lower component exhibits the dynamical enhancement due to the combination of the scalar and vector potentials. Second, the eikonal phase  $e^{iS(\vec{r})}$  accounts for the interactions that the struck nucleon undergoes in its way out of the target nucleus.

It is worth noting that the eikonal wave function does not exhibit the correct asymptotic behaviour for  $\vec{r} \rightarrow +\infty$  :

$$\lim_{\vec{r} \rightarrow +\infty} \psi_{\vec{k},s}^{(+)}(\vec{r}) = \sqrt{\frac{E+M}{2M}} \left[ \frac{1}{E+M} \vec{\sigma} \cdot \vec{p} \right] e^{i\vec{k} \cdot \vec{r}} e^{-i\frac{M}{K} \int_{-\infty}^{+\infty} dz' [V_c + V_{so} \vec{\sigma} \cdot (\vec{b} \times \vec{K})]} \chi_{\frac{1}{2}m_s} \quad (5.19)$$

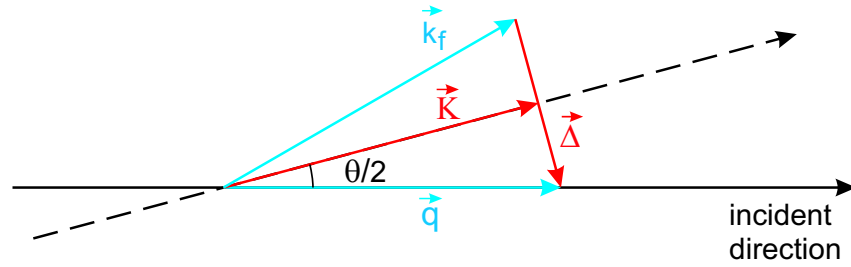


**Figure 5.2** Illustration of the vectors involved in the eikonal trajectory.

As a matter of fact, this feature is generally not considered as a serious deficiency. Indeed, the transition matrix elements, which involve bound state wave functions, are only sensitive to the radial range in which the potentials are non-vanishing.

Another point of concern is the angular range in which the eikonal method is a valid approximation. In Eq. (5.16) the eikonal phase is calculated by performing a straight line integration along the direction of the average momentum  $\vec{K}$ , as in Fig. 5.2. A more accurate evaluation of the scattering wave function would in fact involve the calculation of its phase along the actual curved classical trajectory. This is exactly the small-angle approximation that was imposed. It must be remembered that the semi-classical approximation is not valid for large scattering angles. But, as already mentioned, high energy pA scattering is diffractive and extremely forwardly peaked.

The calculation of the eikonal phase of Eq. (5.16) involves a transformation to a reference frame other than the usual laboratory or center-of-mass frame, namely the frame where the average momentum is pointing along the  $z$  axis. As the eikonal phase has to be reevaluated for every  $(\vec{b}, z)$  point in space, the Dirac eikonal ( $e, e'p$ ) calculations are very demanding as far as computing power is concerned. In evaluating the matrix elements, the radial integrations were performed on a 0.1 fm mesh.

### 5.3 Optical Potentials and the Eikonal Method

The potentials that are used in relativistic Hartree calculations are real potentials. This results in a purely imaginary eikonal phase (that is, apart from a tiny contribution in the spin-orbit channel). Although this consistent treatment minimizes the effects of spurious states, it can also only take elastic contributions into account. In general, strength from the incident beam is drained into other inelastic channels, and one needs to incorporate this local absorption in the description of the reaction process. This is commonly done in DWIA by adopting a complex or optical potential that is able to describe elastic scattering accompanied by absorption. With such potentials one obtains an eikonal phase that contains both an imaginary and real part. This reflects the fact that part of the strength will be removed from the

elastic channel into the inelastic ones.

For several years now Dirac phenomenology has been used to determine global nucleon-nucleus optical potentials which cover proton kinetic energies up to 1 GeV [56, 61, 62]. This phenomenology, which uses the Dirac equation to describe the dynamics of the nucleon, naturally accomodates the major characteristics of the nonrelativistic nuclear optical potentials, namely, its central and spin-orbit terms. Moreover, the use of relativistic kinematics is undoubtedly required for kinetic energies exceding intermediate energies. In our calculations we have adopted the global relativistic optical potential model of Cooper et al. [56]. By fitting proton elastic scattering data in the energy range of 20 - 1040 MeV, Cooper et al. succeeded in obtaining a set of energy-dependent potentials for the target nuclei  $^{12}\text{C}$ ,  $^{16}\text{O}$ ,  $^{40}\text{Ca}$ ,  $^{90}\text{Zr}$  and  $^{208}\text{Pb}$ . The general form for their scalar and vector optical potentials is

$$\begin{aligned} U(r, E, A) = & V^V(E, A)f^V(r, E, A) + V^S(E, A)f^S(r, E, A) \\ & + iW^V(E, A)g^V(r, E, A) \\ & + iW^S(E, A)g^S(r, E, A), \end{aligned} \quad (5.20)$$

where the superscripts  $V$  and  $S$  refer to volume and surface peaked terms. The geometries are parametrized as :

$$f^V \text{ and } g^V = \frac{\cosh[R(E, A)/a(E, A)] - 1}{\cosh[R(E, A)/a(E, A)] + \cosh[r/a(E, A)] - 2}, \quad (5.21)$$

$$f^S \text{ and } g^S = \frac{(\cosh[R(E, A)/a(E, A)] - 1)(\cosh[r/a(E, A)] - 1)}{(\cosh[R(E, A)/a(E, A)] + \cosh[r/a(E, A)] - 2)^2}. \quad (5.22)$$

The energy and mass dependence of the potentials are then parametrized in terms of a set of polynomials of the form

$$\begin{aligned} V^V(E, A) = & v_0 + \sum_{m=1}^4 v_m x^m + \sum_{n=1}^3 v_{n+4} y^n + v_8 xy \\ & + v_9 x^2 y + v_{10} xy^2, \end{aligned} \quad (5.23)$$

where  $x = 1000/E$  and  $y = A/(A + 20)$ . An equivalent expression is used for the other potentials and for the  $R(E, A)$  and  $a(E, A)$  variables. Such a model provides a set of 264 parameters, which are determined by requiring that the above functional dependencies describe the data as accurately as possible.

As an illustration, we present potentials for the target nuclei  $^{12}\text{C}$  and  $^{16}\text{O}$ . In Figs. 5.3 and 5.4 the Cooper potentials are presented for three values of the proton kinetic energy (expressed in the laboratory frame). As a reference, the energy-independent potentials as obtained from the bound state calculations on the basis of Eq. (3.7) are also shown.

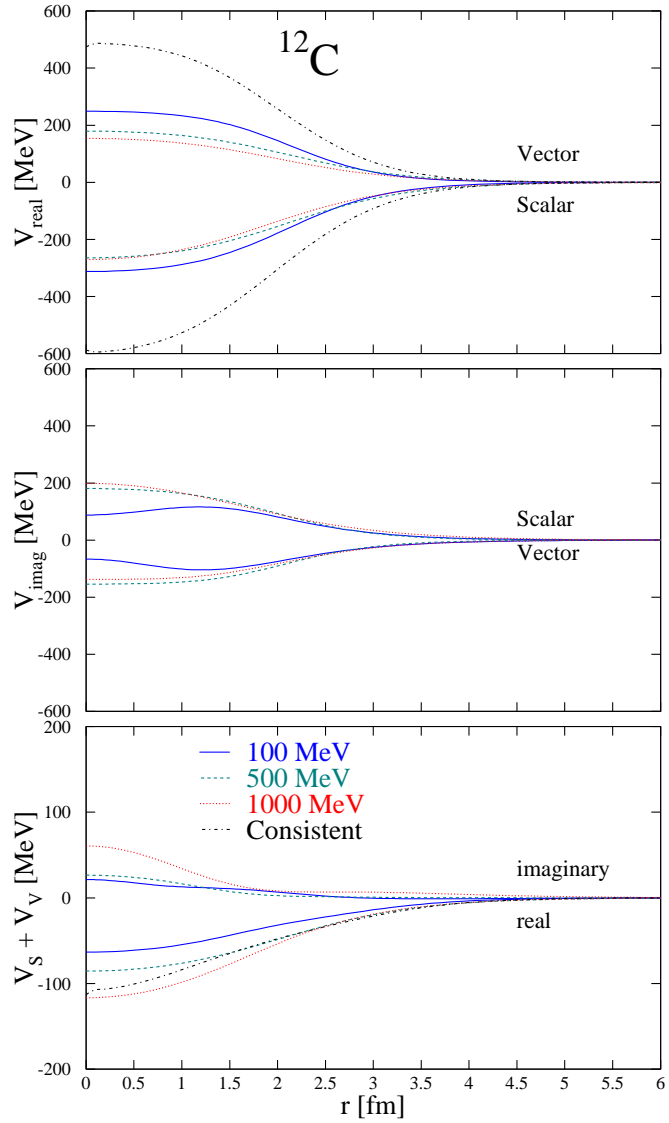


**Figure 5.3** The real and imaginary parts of the Cooper optical potentials for the  $^{12}\text{C}$  target nucleus, at three values of the proton kinetic energy : 100 MeV (solid line), 500 MeV (dashed line) and 1000 MeV (dotted line). The upper panel depicts the real parts of the Dirac vector and scalar potentials, while the middle panel does the same for the imaginary parts. In the bottom panel, the dot-dashed line shows the sum of the scalar and vector potential as obtained from the relativistic Hartree calculations as outlined in Sec. 3.

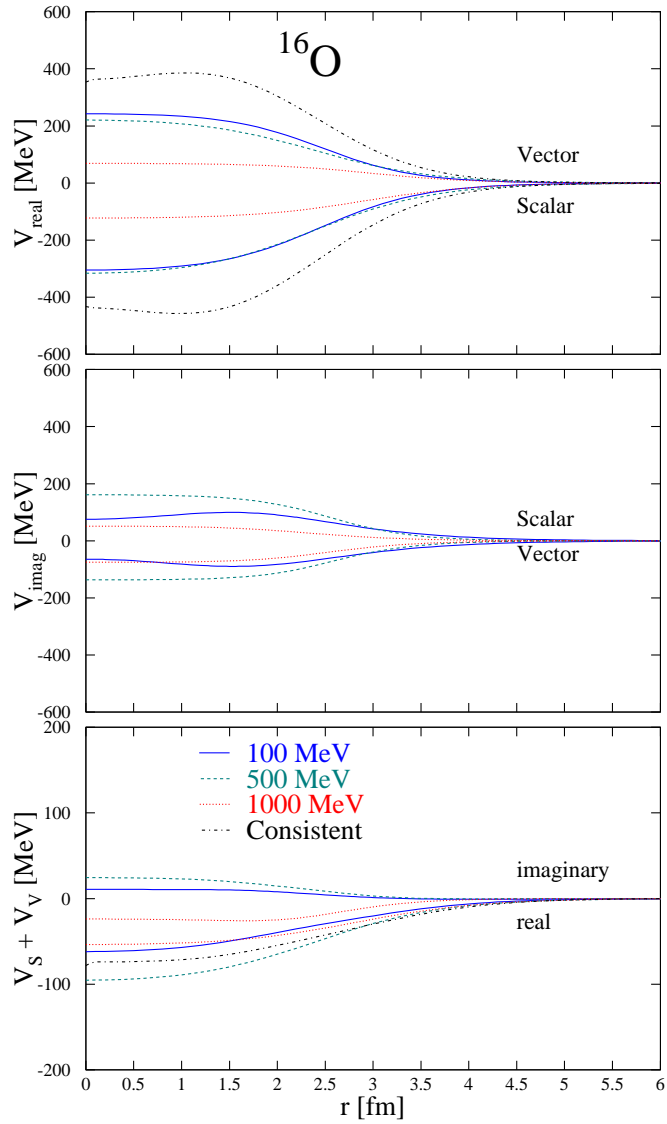


Figure 5.4 As in Fig. 5.3, but now for the  $^{16}\text{O}$  target nucleus.

## 5.4 The Glauber Approach

Glauber theory is a multiple-scattering extension of the standard (non-relativistic) eikonal approximation that relates the ejectile's distorted wave function to the proton elastic scattering data through the introduction of a profile function. In the past, Glauber theory has been highly successful in describing small-angle proton-nucleus scattering in the energy domain  $T_p > 500$  MeV [6, 9]. It has been suggested that Glauber theory may also provide a good starting basis for the description of the final state interactions in  $A(e, e'p)$  reactions at high energies.

### 5.4.1 Non-relativistic Glauber theory

In deriving the non-relativistic eikonal wave function, one starts from the time-independent Schrödinger equation

$$\left( -\frac{\hbar^2}{2m} \nabla^2 + V(\vec{r}) \right) \Psi(\vec{r}) = E\Psi(\vec{r}), \quad (5.24)$$

for a particle with mass  $m$  moving in the field of a potential  $V(\vec{r})$ . As in Sec. 5.2, one arrives, after some straightforward manipulations, at the following eikonal wave function [63] :

$$\Psi_{k_f}^E(\vec{r}) = (2\pi)^{-3/2} \exp \left[ i\vec{k}_f \cdot \vec{r} - \frac{i}{2k_f} \int_{-\infty}^z dz' U(x, y, z') \right], \quad (5.25)$$

where  $U(\vec{r}) \equiv 2mV(\vec{r})/\hbar^2$  is the reduced potential. The scattering amplitude is formally written as

$$f_E = -2\pi^2 \langle \Phi_{\vec{k}_i} | U | \Psi_{k_f}^E \rangle, \quad (5.26)$$

with  $\Phi_{\vec{k}_i}$  a plane wave corresponding to the momentum  $\vec{k}_i$ . Inserting the eikonal wave of Eq. (5.25) into Eq. (5.26) leaves us with the following expression :

$$f_E = -\frac{1}{4\pi} \int d\vec{r} e^{i(\vec{k}_f - \vec{k}_i) \cdot \vec{r}} U(\vec{r}) \exp \left[ -\frac{i}{2k_f} \int_{-\infty}^z U(x, y, z') dz' \right]. \quad (5.27)$$

Since only small-angle scattering is considered here, on the basis of Fig. 5.2 one can write that

$$(\vec{k}_f - \vec{k}_i) \cdot \vec{r} \simeq (\vec{k}_f - \vec{k}_i) \cdot \vec{b} = \vec{\Delta} \cdot \vec{b}. \quad (5.28)$$

The integration over the variable  $z$  is straightforward. With the aid of Eq. (5.28) the eikonal scattering amplitude can be rewritten as

$$f_E = \frac{ik_f}{2\pi} \int d\vec{b} \exp(i\vec{\Delta} \cdot \vec{b}) \Gamma(k_f, \vec{b}) \quad (5.29)$$

where we defined the profile function

$$\Gamma(k_f, \vec{b}) = 1 - \exp[i\chi(k_f, \vec{b})]. \quad (5.30)$$

The eikonal phase-shift function is determined through the following expression :

$$\chi(k_f, \vec{b}) = -\frac{1}{2k_f} \int_{-\infty}^{+\infty} U(\vec{b}, z) dz. \quad (5.31)$$

In standard Glauber theory the phase shifts are not calculated on the basis of potentials, but are directly extracted from proton-proton and proton-neutron scattering data. To cut a long story short, on the basis of Eq. (5.29) one manages to determine the profile function directly from elastic nucleon scattering data. In what follows, this procedure will be outlined in far more detail.

The analysis of pp and pn scattering observables in which at most one of the hadrons is polarized, can be done on the basis of the following general structure for the scattering amplitude [6]

$$f_{pN}(\vec{\Delta}) = f_{pN}^c(\Delta) + f_{pN}^s(\Delta) \vec{\sigma} \cdot \vec{n}, \quad (N = p, n), \quad (5.32)$$

where  $f_{pN}^c$  and  $f_{pN}^s$  are the central and spin-orbit amplitudes,  $\vec{\sigma}$  is the spin-operator corresponding with the incident proton, and  $\vec{\Delta}$  is the transferred momentum. The small angle elastic scattering of energetic protons is dominated by the central, spin-independent amplitude. The central amplitudes are usually parametrized in the form

$$f_{pN}^c(\Delta) = \frac{k_f \sigma_{pN}^{tot}}{4\pi} (\epsilon_{pN} + i) \exp\left(-\frac{\Delta^2 \beta_{pN}^2}{2}\right). \quad (5.33)$$

The parameters in Eq. (5.33) can be taken directly from the nucleon-nucleon scattering experiments. The measured elastic and total cross sections  $\sigma_{pp}$  and  $\sigma_{pn}$  are shown in Fig. 5.5. These data points have been collected by various experimental groups, and are bundled by the Particle Data Group [64]. All experimental results for pp and pn scattering cross sections used in our calculations were taken from these references. The slope parameters  $\beta_{pp}^2$  and  $\beta_{pn}^2$  may be found by analysing the shape of the differential cross sections assuming that the contribution from the spin-dependent terms is negligible. At energies  $E_p \leq 1$  GeV the slope parameters found directly from experiment and phase-shift analysis differ significantly due to a large contribution from the spin terms. This feature emerging from the analysis of the data is illustrated in Fig. 5.6. Results for measured and calculated values for the slope parameters are shown in Fig. 5.7. At higher energies this difference drops quickly indicating that spin effects are small in that region. Since values for the slope parameters below 1 GeV are scarce and not free of ambiguities due to spin contributions, we have chosen to use a parametrization based on the theoretical

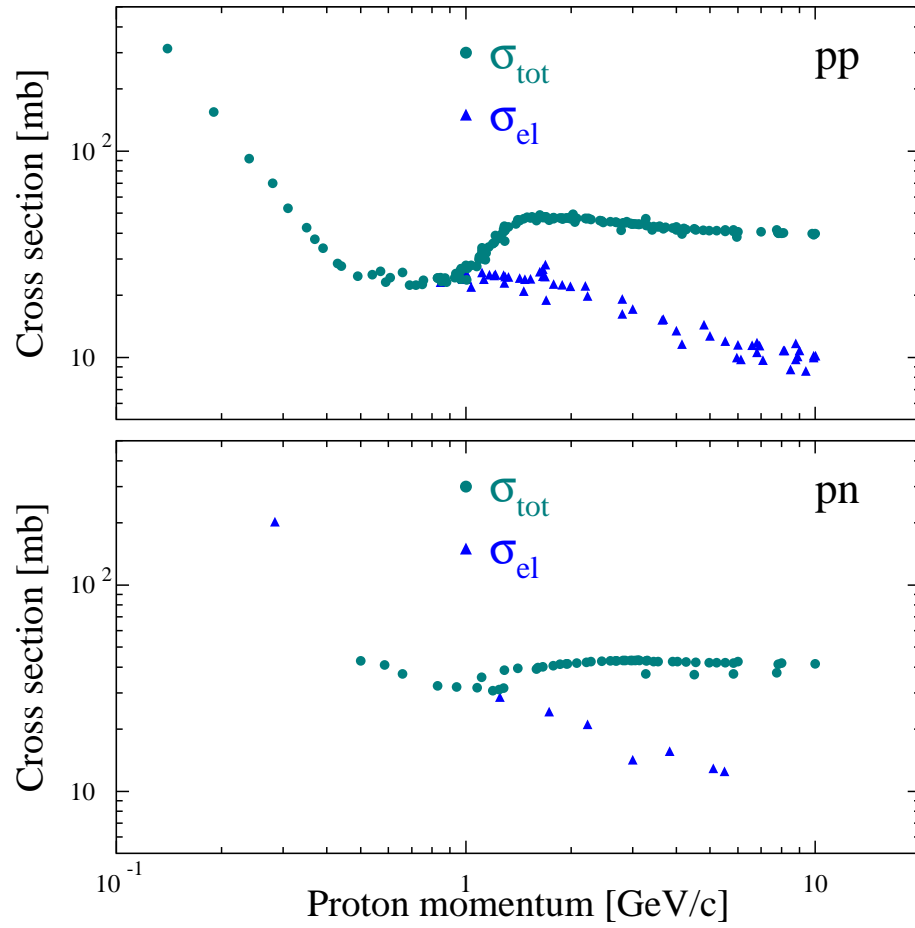


**Figure 5.5** Total and elastic cross sections for pp and pn scattering as a function of the lab proton momentum. The data were taken from Ref. [64].

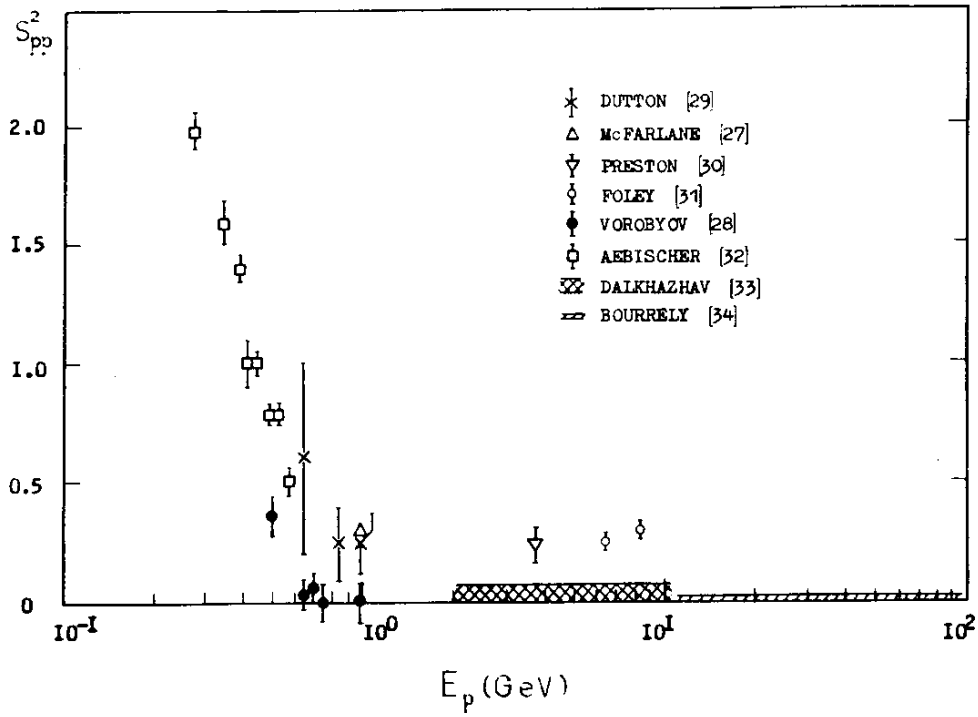


**Figure 5.6** This picture, that was taken from Ref. [6] shows the absolute contributions from the spin-dependent terms to the differential pp scattering cross section at small angles.

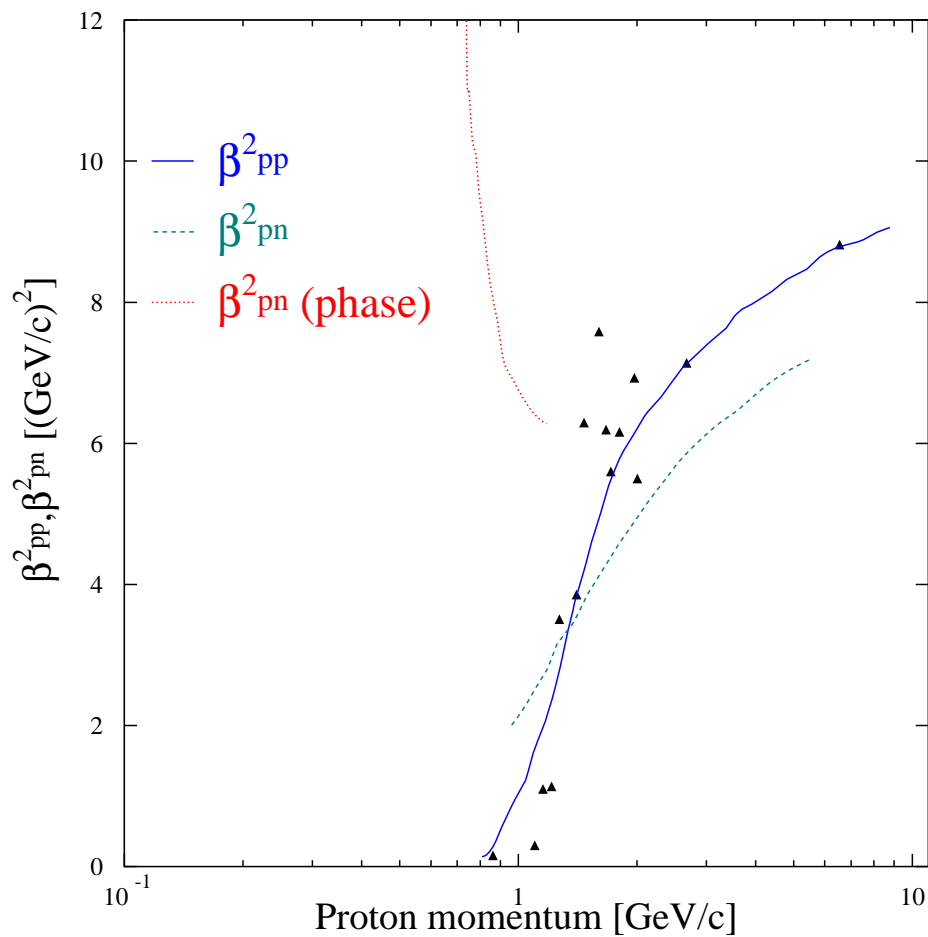


**Figure 5.7** Slope parameters for pp and pn scattering. The solid and dashed lines are results of calculations that rely on the experimental data points, for pp and pn scattering, respectively. These experimental data points have been plotted for the pp scattering reaction. The dotted line is the result of a phase shift analysis of the pn scattering reaction. For references to the data points and calculations, see Ref. [6].

shape of the elastic nucleon-nucleon cross section. The elastic scattering amplitude of Eq. (5.33) is directly related to the elastic differential cross section through the following expression

$$\frac{d^2\sigma_{el}}{d\Delta} = \frac{1}{k_f^2} |f_{el}(\Delta)|^2 = \frac{\sigma_{tot}^2(1+\epsilon^2)}{16\pi^2} \exp(-\Delta^2\beta^2), \quad (5.34)$$

which is the standard high-energy approximation of the elastic differential cross section. Integrating this differential cross section leaves us with

$$\sigma_{el} = \int \frac{d^2\sigma_{el}}{d\Delta} d\Delta = \frac{\sigma_{tot}^2(1+\epsilon^2)}{16\pi^2\beta^2}. \quad (5.35)$$

This expression allows to derive the value of the slope parameter from the experimentally known values of the elastic cross section and the ratios of the real to imaginary part of the forward elastic scattering amplitudes. An example of such a calculation can be found in Fig. 5.8, that has been taken from Ref. [65]. In this reference use is made of a widely spread partial-wave analysis of nucleon-nucleon elastic scattering data by Arndt et al. [66, 67, 68, 69, 70]. We use the experimental values for  $\epsilon_{pp}$  and  $\epsilon_{pn}$  of Ref. [64] however; they can be found in Fig. 5.9.

By analogy with the central amplitude, the spin-orbit amplitude can be parametrized as

$$f_{pN}^s = \gamma \frac{k_f \sigma_{pN}^{tot}}{4\pi} (\epsilon_{pN}^s + i) \exp\left(-\frac{\Delta^2 \beta_{pN}^{s2}}{2}\right). \quad (5.36)$$

Let us now consider the case of central scattering scattering. Inverting Eq. (5.29) leaves us with

$$\Gamma(k_f, \vec{b}) = \frac{2\pi}{ik_f} \int \frac{d\vec{\Delta}}{(2\pi)^2} \exp(-i\vec{\Delta} \cdot \vec{b}) f_E(\vec{\Delta}). \quad (5.37)$$

Inserting the parametrization of Eq. (5.33) into this expression, gives us then the following expression for the profile function :

$$\Gamma(k_f, \vec{b}) = \frac{\sigma_{pN}^{tot}(1-i\epsilon_{pN})}{4\pi\beta_{pN}^2} \exp\left(-\frac{b^2}{2\beta_{pN}^2}\right). \quad (5.38)$$

In the analysis of the proton-nucleus scattering data, the spinless version of Glauber theory was very successful [5, 71]. As can be inferred from Fig. 5.6, the spin-dependent contributions to the proton scattering process are relatively weak for higher kinetic energies. All results that are presented in this work are obtained within the framework of the spinless version of the Glauber theory.

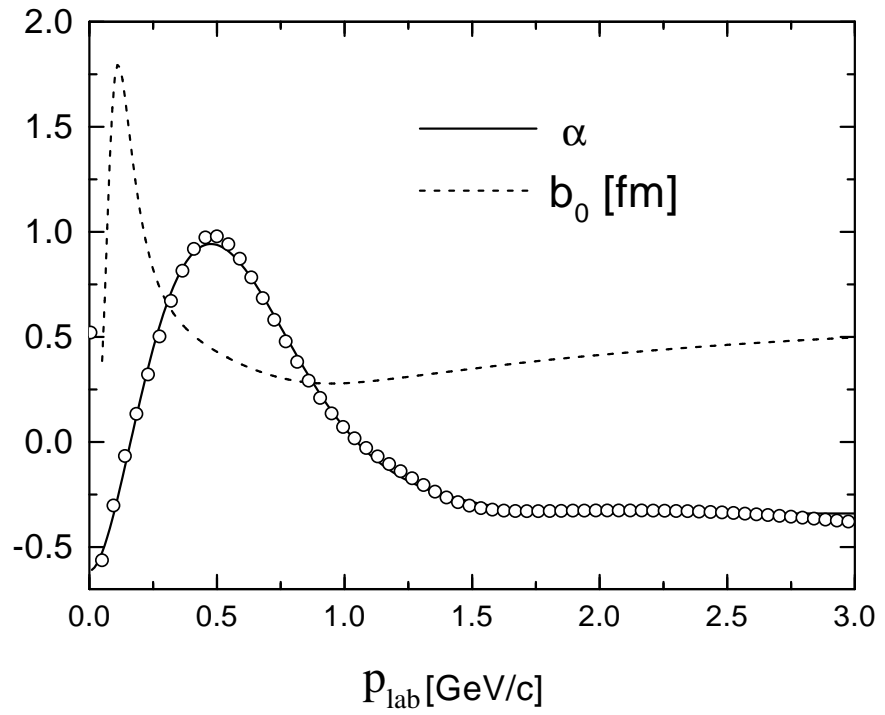


**Figure 5.8** The pn slope parameter  $b_0$  (in our notation,  $\beta$ ) calculated with the aid of Eq. (5.35). The ratio between the imaginary to the real part of the forward elastic amplitude for pn scattering  $\alpha$  (in our notation,  $\epsilon$ ) that was used in Eq. (5.35) is also depicted. These plots were taken from Ref. [65].

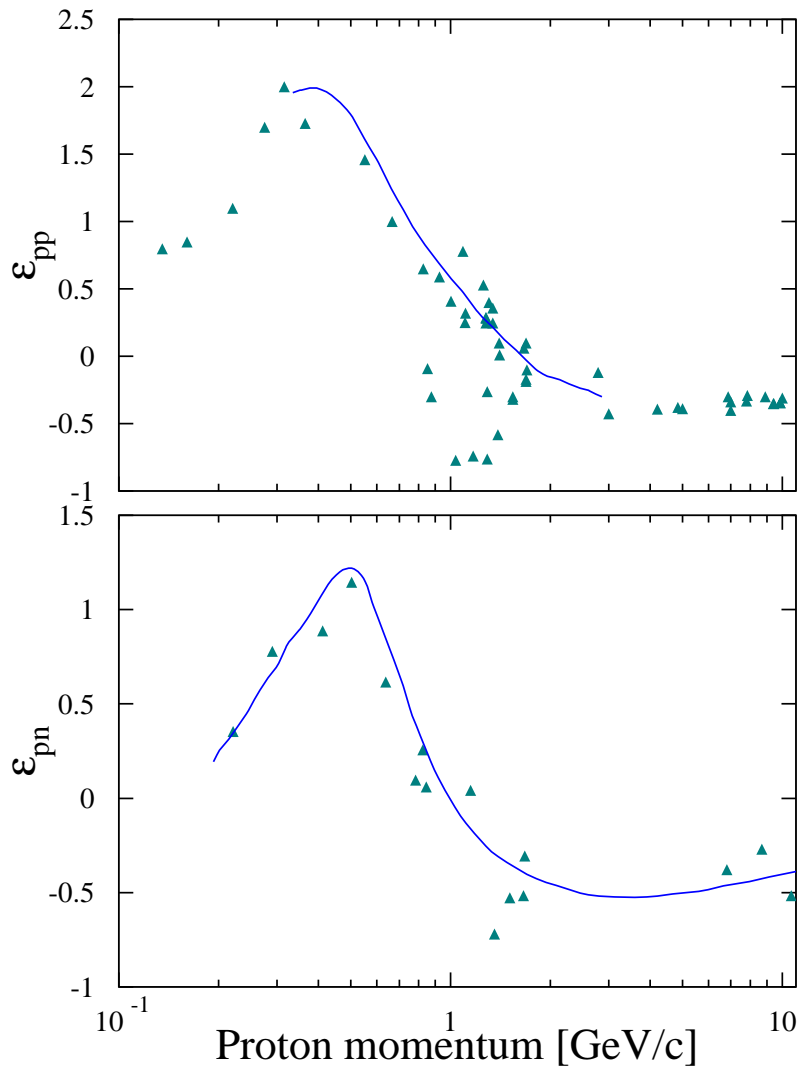


**Figure 5.9** The ratios of the real to imaginary parts of the central amplitude for pp and pn scattering. The solid lines present calculations based on the data. For references see Ref. [6].

### 5.4.2 Connection between the Profile Function and the NN Potential

In this section we sketch a procedure which allows to construct the nucleon-nucleon potential directly from the profile function of Eq. (5.38), which in itself was derived from the scattering amplitudes [14, 72]. We assume that the scattering process is dominated by the central, spin-independent amplitude.

From Eq. (5.30) we have that

$$\chi(k_f, \vec{b}) = \frac{1}{i} \log(1 - \Gamma(k_f, \vec{b})) , \quad (5.39)$$

and from Eq. (5.31) that

$$\chi(k_f, \vec{b}) = -\frac{1}{2k_f} \int_{-\infty}^{+\infty} U(\vec{b}, z) dz = -\frac{1}{v_f} \int_{-\infty}^{+\infty} V_{NN}(\vec{b}, z) dz , \quad (5.40)$$

where  $V_{NN}$  is the nucleon-nucleon potential and  $v_f$  denotes the proton's velocity. By using the Abel integration equation [73] to invert Eq. (5.40), we obtain

$$\begin{aligned} V_{NN}(r) &= \frac{v_f}{\pi} \frac{1}{r} \frac{d}{dr} \int_r^{\infty} b db \frac{\chi(b)}{\sqrt{b^2 - r^2}} \\ &= \frac{v_f}{\pi} \frac{1}{r} \frac{d}{dr} \int_r^{\infty} b db \frac{\log(1 - \Gamma(b))}{i\sqrt{b^2 - r^2}} \\ &= \frac{v_f}{\pi} \frac{1}{r} \frac{d}{dr} \int_0^{\infty} dy \frac{1}{i} \log(1 - \Gamma(y^2 + r^2)) \\ &= \frac{v_f}{i\pi\beta_{pN}^2} \int_0^{\infty} dy \frac{\Gamma(0)e^{-(y^2+r^2)/2\beta_{pN}^2}}{1 - \Gamma(0)e^{-(y^2+r^2)/2\beta_{pN}^2}} , \end{aligned} \quad (5.41)$$

where  $y = \sqrt{b^2 - r^2}$ , and where we have introduced the notation

$$\Gamma(0) = \frac{\sigma_{pN}^{tot}(1 - i\epsilon_{pN})}{4\pi\beta_{pN}^2} . \quad (5.42)$$

A word of caution is in order when trying to extract potentials directly from the scattering observables. In Fig. 5.10 we have plotted the proton-proton potential calculated with the aid of Eq. (5.41) for a 2 GeV proton-proton collision. We have assumed a value of 47.5 mb for the total pp cross section and a value of  $-0.10$  for the ratio of the real to imaginary part of the forward elastic scattering amplitude. The three calculations present results for three different slope parameters. As can be seen, relatively small changes in the slope parameters induce considerable shifts in the obtained potentials. This exercise also illustrates the role of the slope parameter as a measure for the range in which the nucleon-nucleon interaction takes place. The smaller the slope parameter the longer the range in which the nucleon-nucleon interaction takes place. This concurs with the fact that the slope parameter increases with increasing energies, and, hence, smaller distance scales are probed.

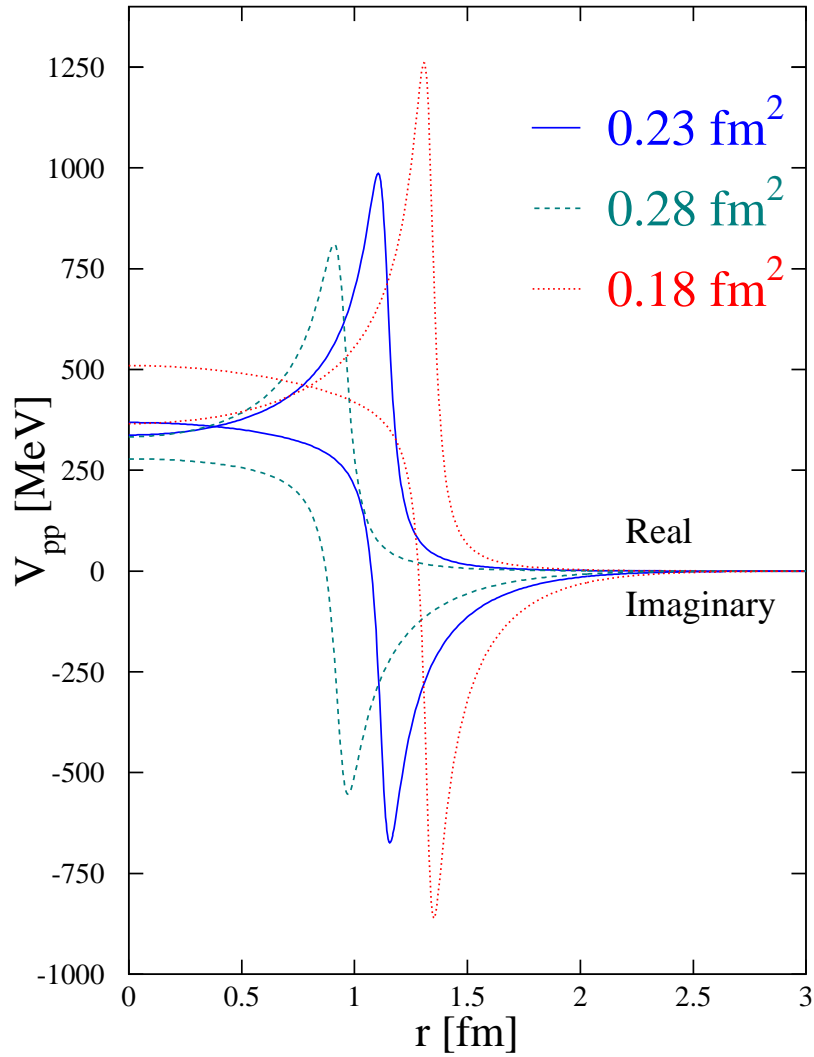


**Figure 5.10** Proton-proton potential as a function of the radius  $r$  for the case of  $k_f = 2$  GeV/c,  $\sigma_{tot}^{pp} = 47.5$  mb and  $\epsilon_{pp} = -0.1$ . The slope parameters were varied about the central value  $\beta_{pp}^2 = 0.23$  fm<sup>2</sup>.

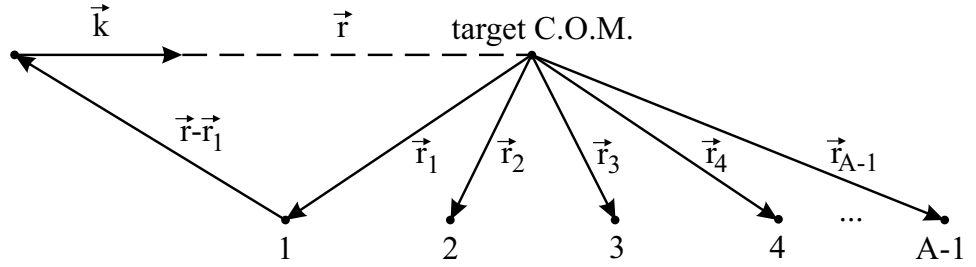


**Figure 5.11** Schematic representation of the multiple-scattering of one proton with the rest of the nucleons in the nucleus.

### 5.4.3 Glauber Multiple Scattering Theory

We now take things a step further by considering the scattering of a fast particle A (“ejected proton”) by a composite target B (“nucleus”) containing  $N$  scatterers (“remaining nucleons”), as in Fig. 5.11. We assume that the motion of the target particles is slow by comparison with the relative motion of A and B (i.e.  $|\vec{k}| \gg |k_1|, |k_2|, \dots$ ). Moreover, we suppose that the incident particle interacts with the target scatterers by means of two-body spin-independent interactions. Exchange effects between the incident and target particles are also neglected. The Glauber scattering amplitude for a direct collision leading from an initial target state  $|i\rangle$  to a final state  $|f\rangle$  is then given by

$$f_{\text{Multi}}(\vec{\Delta}) = \frac{ik_f}{2\pi} \int d\vec{b} e^{i\vec{\Delta} \cdot \vec{b}} \langle f | 1 - e^{i\chi_{\text{tot}}(\vec{b}, \vec{b}_1, \dots, \vec{b}_N)} | i \rangle . \quad (5.43)$$

The total Glauber phase shift function

$$\chi_{\text{tot}}(\vec{b}, \vec{b}_1, \dots, \vec{b}_N) = \sum_{i=1}^N \chi_i(\vec{b} - \vec{b}_i) , \quad (5.44)$$

is the sum of the phase shifts  $\chi_i$  contributed by each of the target scatterers as the wave, representing the incident particle, progresses through the target system. This property of so-called phase-shift additivity is a direct consequence of the one-dimensional nature of the relative motion, together with the neglect of three-body forces, target scatterer motion and longitudinal momentum transfer. Furthermore, it is important to note that the expression of Eq. (5.43) only applies to collisions for which the energy transfer is small compared to the incident particle energy. This is true for elastic collisions and for mildly inelastic ones in which the target is excited. It is not true for deep inelastic collisions in which the nature of the incident or target particles is modified or the number of particles is altered during collision.

Following the work of Glauber [5], we define the quantity

$$\Gamma_{\text{tot}}(\vec{b}, \vec{b}_1, \dots, \vec{b}_N) = 1 - \exp[i\chi_{\text{tot}}(\vec{b}, \vec{b}_1, \dots, \vec{b}_N)] , \quad (5.45)$$

so that Eq. (5.43) becomes

$$f_{\text{Multi}}(\vec{\Delta}) = \frac{ik_f}{2\pi} \int d\vec{b} e^{i\vec{\Delta} \cdot \vec{b}} \langle f | \Gamma_{\text{tot}}(\vec{b}, \vec{b}_1, \dots, \vec{b}_N | i \rangle . \quad (5.46)$$

We introduce the functions

$$\Gamma_i(\vec{b} - \vec{b}_i) = 1 - \exp[i\chi_i(\vec{b} - \vec{b}_i)] , \quad (5.47)$$

and by combining Eqs. (5.44), (5.45) and (5.47), we can write that

$$\Gamma_{\text{tot}} = 1 - \prod_{i=1}^N [1 - \Gamma_i(\vec{b} - \vec{b}_i)] , \quad (5.48)$$

or

$$\Gamma_{\text{tot}} = \sum_{i=1}^N \Gamma_i - \sum_{i \neq j} \Gamma_i \Gamma_j + \dots + (-1)^{N-1} \prod_{i=1}^N \Gamma_i . \quad (5.49)$$

This last equation, when substituted into Eq. (5.46), leads directly to an interpretation of the collision process in terms of a multiple scattering expansion. The terms linear in  $\Gamma_i$  on the right-hand side of Eq. (5.49) account for the single scattering, whereas the next terms provide double, triple,... scattering contributions. As is mostly done in many-body calculations, all Glauber calculations reported in this work are performed in the approximation

$$\Gamma_{\text{tot}} \approx \sum_{i=1}^N \Gamma_i . \quad (5.50)$$

which amounts to retaining all single rescattering processes in the calculation.

In calculating the transition strength in the Glauber approach one finds himself confronted with matrix elements of the type

$$\langle A-1 | \sum_{j=1}^{A-1} \Gamma_j(\vec{b} - \vec{b}_j) \theta(z - z_j) | A-1 \rangle , \quad (5.51)$$

where  $\theta(z - z_j)$  expresses the fact that the proton only interacts (collides) with the other nucleons if they are localised in its forward propagation path. The above expression easily reduces to the following sum :

$$\begin{aligned} & \int d\vec{r}_1 \rho_1(\vec{r}_1) \Gamma_1(\vec{b} - \vec{b}_1) \theta(z - z_1) + \int d\vec{r}_2 \rho_2(\vec{r}_2) \Gamma_2(\vec{b} - \vec{b}_2) \theta(z - z_2) \\ & + \dots + \int d\vec{r}_{A-1} \rho_{A-1}(\vec{r}_{A-1}) \Gamma_{A-1}(\vec{b} - \vec{b}_{A-1}) \theta(z - z_{A-1}) , \end{aligned} \quad (5.52)$$

where  $\rho_i$  denotes the density distribution of the nucleon with quantumnumbers  $i$ . One thus arrives at an expression where the profile functions are folded with the nucleonic densities.

In deriving Eq. (5.52) we have supposed an independent-particle behaviour. A more realistic description needs the introduction of nucleon-nucleon correlations. This can now simply be adopted by the substitution

$$\rho_i(\vec{r}_i) \rightarrow \rho_i(\vec{r}_i)g(\vec{r} - \vec{r}_i) , \quad (5.53)$$

where  $g(\vec{r} - \vec{r}_i)$  is the (central) correlation function. The important role played by these short-range correlations has been extensively discussed in literature [8, 74, 75, 76, 77]. We will address these correlations further in Sec. 9, when discussing nuclear transparencies, as they appear to play a significant role there. We use the correlation function proposed by Gearheart and Dickhoff [78, 79] as plotted in Fig. 5.12. This choice is based on the fact that this correlation function was shown to produce a favorable agreement with  $^{12}\text{C}(e, e'p)$  data [80]. Also, in comparison with other model predictions for the central correlation function, the one obtained by Gearhart and Dickhoff can be classified between the categories of “hard” (with a core at short internucleonic distances) and “soft” (characterized by a finite probability to observe nucleon pairs at very short internucleonic distances) correlations.

#### 5.4.4 Relativistic Extension of the Glauber Approximation

In this section a relativistic generalization of the non-relativistic Glauber framework will be outlined. We start from the scattering amplitude [57]

$$F_{ss'}(\vec{k}_i, \vec{k}_f, E) = -\frac{M}{2\pi} \langle \Phi_{\vec{k}_i, s} | (\beta V_s + V_v) | \psi_{\vec{k}_f, s'}^{(+)} \rangle , \quad (5.54)$$

with a relativistic scattered wave of the type

$$\psi_{\vec{k}_f, s'}^{(+)} = \sqrt{\frac{E+M}{2M}} \left[ \frac{1}{E+M+V_s-V_v} \vec{\sigma} \cdot \vec{p} \right] e^{i\vec{k}_f \cdot \vec{r}} e^{iS(\vec{r})} \chi_{\frac{1}{2}m_{s'}} , \quad (5.55)$$

and the free Dirac solution

$$\Phi_{\vec{k}_i, s} = \sqrt{\frac{E+M}{2M}} \left[ \frac{1}{E+M} \vec{\sigma} \cdot \vec{k}_i \right] e^{i\vec{k}_i \cdot \vec{r}} \chi_{\frac{1}{2}m_s} . \quad (5.56)$$

After some straightforward algebraic manipulations one obtains

$$F(\vec{k}_i, \vec{k}_f, E) = -iK \int \frac{d\vec{b}}{2\pi} e^{i\vec{q} \cdot \vec{b}} (e^{i\chi(\vec{b})} - 1) , \quad (5.57)$$

where

$$F_{ss'}(\vec{k}_i, \vec{k}_f, E) = \langle \chi_{s'} | F(\vec{k}_i, \vec{k}_f, E) | \chi_s \rangle . \quad (5.58)$$

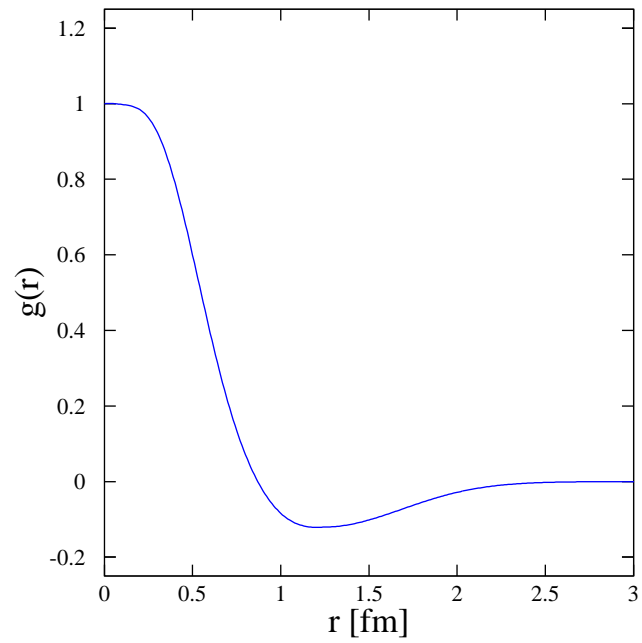


**Figure 5.12** The Gearheart-Dickoff correlation function as a function of the relative internucleonic range  $r$ .

The phase shift function is given by

$$\chi(\vec{b}) = i \frac{M}{K} \int_{-\infty}^{+\infty} dz [V_c(\vec{b}, z) + V_{so}(\vec{b}, z) [\vec{\sigma} \cdot (\vec{b} \times \vec{K})]] . \quad (5.59)$$

In what follows only the spin-independent parts of the scattering amplitude will be retained. In a completely analogous manner as outlined in the previous sections, one can generalize and perform a multiple-scattering expansion. The profile functions remain the same as in Sec. 5.4.3, but we are now working with relativistic plane waves and we can make use of relativistic current operators when evaluating the interaction matrix elements. All Glauber calculations presented in this work are the result of this relativistic Glauber scheme.

## 5.5 Higher Order Eikonal Corrections

In this section we want to show that the wave function derived in Sec. 5.2 is in fact the first-order term in a semiclassical expansion of the Dirac equation under a specific cone-like geometry [81, 82, 83, 84].

The derivation starts from the time-dependent Dirac equation for a relativistic nucleon with energy  $E = \sqrt{k^2 + M^2}$  in the presence of local scalar and vector potentials  $S$  and  $V_\mu$ , respectively :

$$[\gamma^\mu (p_\mu - V_\mu) - (M + S)] \Psi = 0 . \quad (5.60)$$

Multiplying this equation with the operator  $[\gamma_\nu (p_\nu - V_\nu) + (M + S)]$  leaves us with a second order equation for the bi-spinor  $\Psi$  :

$$\left[ (i\partial_\mu - V_\mu)^2 - (M + S)^2 + \sigma^{\mu\nu} (\partial_\nu V_\mu) - i\gamma^\mu (\partial_\mu S) \right] \Psi = 0 . \quad (5.61)$$

Apart from the divergencies in the potentials  $S$  and  $V_\mu$ , this equation corresponds to the Klein-Gordon equation for a particle with mass  $M + S$  in an external field  $V_\mu$ . At high energies, one searches for a solution of the following form :

$$\Psi = e^{i\chi} f , \quad (5.62)$$

where  $f$  now contains all of the spinor information. Insertion of Eq. (5.62) into Eq. (5.61) then yields

$$\begin{aligned} & \left[ (\partial_\mu \chi)(\partial^\mu \chi) + 2V^\mu (\partial_\mu \chi) + V^\mu V_\mu - (M + S)^2 \right] e^{i\chi} f \\ & - i [(\partial^\mu \partial_\mu \chi) + (\partial_\mu V^\mu)] e^{i\chi} f - 2i [(\partial^\mu \chi) + V^\mu] (\partial_\mu f) e^{i\chi} \\ & + \sigma^{\mu\nu} (\partial_\nu V_\mu) e^{i\chi} f - i\gamma^\mu (\partial_\mu S) e^{i\chi} f \\ & = e^{i\chi} \left( \frac{\partial^2}{\partial t^2} - \nabla^2 \right) f . \end{aligned} \quad (5.63)$$

Solving this equation can be reduced to finding the solutions to the following set of equations :

$$[(\partial_\mu \chi) + V_\mu]^2 - (M + S)^2 = 0 , \quad (5.64)$$

$$\begin{aligned} [\partial_\mu (\partial^\mu \chi + V^\mu)] f + 2 [\partial^\mu \chi + V^\mu] \partial_\mu f + i \sigma^{\mu\nu} (\partial_\nu V_\mu) f \\ + \gamma^\mu (\partial_\mu S) f = i \left( \frac{\partial^2}{\partial t^2} - \nabla^2 \right) f . \end{aligned} \quad (5.65)$$

One could question a representation of the wavefunction as in Eq. (5.62). It can be shown however that Eq. (5.64) is the relativistic Hamilton-Jacobi equation for the classical action  $\chi$  [82]. Eq. (5.65) then determines the behaviour of the wave packet and the spin of the nucleon in the external scalar and vector fields. In the semiclassical approach one neglects the terms proportional to  $\hbar$ . The wave packets themselves then behave similarly to particles moving along classical trajectories corresponding to the action  $\chi$ .

We will only consider local, static potentials, and, on grounds of spherical symmetry, we will assume that only the time-component of  $V_\mu$  is non-zero. Since we are only interested in time-independent solutions, the set of Eqs. (5.64) - (5.65) simplifies to the following one :

$$(\vec{\nabla} \chi)^2 = (E - V)^2 - (M + S)^2 , \quad (5.66)$$

$$- (\nabla^2 \chi) f - 2 \vec{\nabla} \chi \cdot \vec{\nabla} f + \gamma^i (\gamma^0 \partial_i V + \partial_i S) f = 0 . \quad (5.67)$$

Thus far we have followed the approach of Akhiezer et al. [82]. Starting from Eqs. (5.64) - (5.65), or, equivalently, from (5.66) - (5.67), they calculate the eikonal wave function by subsequently distorting a plane wave. However, since we know the correct relation between the upper and lower component of the bi-spinor, we choose to split the Eq. (5.67) in two parts : one for the upper and one for the lower component. Solution of the equation for the upper component then gives us immediately the solution for the lower component. In that way we should produce a more accurate description of the eikonal wave.

This procedure simplifies the set of equations to be solved to following one :

$$\left[ \frac{1}{E + M + S(r) - V(r)} \vec{\sigma} \cdot \vec{p} \right] e^{i\chi(\vec{r})} g(\vec{r}) \chi_{(1/2)m_s} , \quad (5.68)$$

$$(\vec{\nabla} \chi)^2 = (E - V)^2 - (M + S)^2 , \quad (5.69)$$

$$\frac{1}{E + M + S - V} \vec{\sigma} \cdot \vec{\nabla} (S - V) \left[ \vec{\sigma} \cdot \vec{\nabla} \chi g - i \vec{\sigma} \cdot \vec{\nabla} g \right] \quad (5.70)$$

$$-(\nabla^2 \chi)g - 2\vec{\nabla} \cdot \vec{\nabla} g = 0. \quad (5.71)$$

To solve this set of equations, we introduce the following expansions :

$$\chi(\vec{r}) = \vec{k} \cdot \vec{r} + \chi_0(\vec{r}) + \chi_1(\vec{r}) + \dots, \quad (5.72)$$

$$g(\vec{r}) = g_0(\vec{r}) + g_1(\vec{r}) + g_2(\vec{r}) + \dots, \quad (5.73)$$

where  $\chi_n(\vec{r}), g_n(\vec{r}) \propto k^{-n}$ . The lowest, first and second-order solutions read

$$\chi_0 = -\int_{-\infty}^z V dz', \quad (5.74)$$

$$g_0 = 1 \quad (5.75)$$

$$\chi_1 = -\frac{1}{2E} \int_{-\infty}^z [S^2 - V^2 + 2MS + (\vec{\nabla} \chi_0)^2] dz' \quad (5.76)$$

$$g_1 = -\frac{1}{2E} \int_{-\infty}^z [\nabla^2 \chi_0 - \vec{\sigma} \cdot \vec{\nabla} (S - V) \sigma_z] dz' \quad (5.77)$$

$$\chi_2 = -\frac{1}{2E} \int_{-\infty}^z [2\vec{\nabla} \chi_0 \cdot \vec{\nabla} \chi_1 - \frac{M^2}{E} \nabla_z \chi_0] dz' \quad (5.78)$$

$$\begin{aligned} g_2 = & -\frac{1}{2E} \int_{-\infty}^z [(\nabla^2 \chi_0)g_1 + (\nabla^2 \chi_1)g_0 + 2\vec{\nabla} \chi_0 \cdot \vec{\nabla} g_1 \\ & - \frac{1}{E} \vec{\sigma} \cdot \vec{\nabla} (S - V) \{ \sigma_z E g_1 + \vec{\sigma} \cdot \vec{\nabla} \chi_0 g_0 \} \\ & + \frac{M + S - V}{E^2} \vec{\sigma} \cdot \vec{\nabla} (S - V) \sigma_z E g_0] dz'. \end{aligned} \quad (5.79)$$

---

## Chapter 6

# Final State Interactions and the Eikonal Approximation

---

In the previous chapter we have discussed various methods to treat the final state interactions in exclusive  $A(e, e'p)$  reactions. In this chapter all of these different approximations will be put to a stringent test. This will be done by comparing calculated  $A(e, e'p)$  observables with exclusive  $^{16}\text{O}(\vec{e}, e'\vec{p})$  and  $^{12}\text{C}(\vec{e}, e'\vec{p})$  data that have recently been collected at Jefferson Lab (JLAB) and the Stanford Linear Accelerator (SLAC) facility.

### 6.1 $^{16}\text{O}(e, e'p)^{15}\text{N}$

We start our  $(e, e'p)$  investigations within the relativistic eikonal approximation for the kinematics of an  $^{16}\text{O}(e, e'p)$  experiment that was recently performed at Jefferson Lab (E89-003) [15]. The main objectives of this experiment were to determine [15, 85]

- the limits of the validity of the single-particle model of valence proton knockout
- the effects of relativity and spinor distortion on valence proton knockout using the diffractive character of the  $A_{LT}$  asymmetry (with the term “diffractive” we refer to the behaviour of the experimental asymmetry at higher missing momenta)
- the bound state wave function and spectroscopic factors for knockout from the valence shells
- the longitudinal component of the  $(e, e'p)$  cross section at higher missing energies (through the  $R_{TL}$  response function).

In this experiment, the separated  $^{16}\text{O}(e, e'p)$  structure functions and differential cross section were measured at  $Q^2 = 0.8 \text{ (GeV/c)}^2$  and  $\omega = 0.439 \text{ GeV}$  for missing (or, initial) proton momenta  $p_m = |\vec{k}_f - \vec{q}|$  below 355 MeV/c. The variation in missing momentum was achieved by varying the detection angle of the ejected proton with respect to the direction of the momentum transfer (“quasi-perpendicular kinematics”). The measured cross sections for knockout from the  $1p_{1/2}$  and  $1p_{3/2}$  levels are displayed in Fig. 6.1 along with the predictions of our calculations.

The major objective of this chapter is to compare the various schemes for the description of the final state interactions. To that purpose, we will compare the  $A(e, e'p)$  predictions for the various frameworks at specific kinematics. More in particular, we will present results in the Relativistic Plane Wave Impulse Approximation (RPWIA) and three different versions of the eikonal method :

1. a Consistent Eikonal Approximation (CEA) in which the eikonal phase is calculated from the relativistic scalar-vector potential that determines also the bound states
2. an Optical Model Eikonal Approximation (OMEA) in which the eikonal phase is calculated from the optical potentials as they are derived from global fits to elastic proton-nucleus data
3. the Relativistic Multiple-Scattering Glauber Approximation (RMSGGA) as it was outlined in Sec. 5.4

All results presented in this chapter were obtained with the standard dipole form for the electromagnetic form factor. In Fig. 6.1  $^{16}\text{O}(e, e'p)$  results are displayed for all the different models that were sketched above. The spectroscopic factors were determined by performing a  $\chi^2$  fit to the complete data set and are summarized in Table 6.1. Inspecting this table, it becomes clear that in utilizing the CC1 form of the hadron-photon vertex one reaches a far better description of the data than what is obtained with the CC2 version. The spectroscopic factors, on the other hand, do not substantially depend on the choice with respect to the photon-hadron vertex.

### 6.1.1 The Self-Consistent Approach

Fig. 6.1 clearly illustrates that the CEA predicts cross sections that do not follow the experimentally determined trend in the  $p_m$  dependence. Nevertheless, we will discuss the CEA results in some detail, as they do provide insight in the general trends set by the eikonal approach to calculating nucleon scattering states [87].

At low missing momenta, the eikonal results provide a fair description of the  $p_m$  dependence of the data. As a comparison, the results of a relativistic plane wave calculation in the impulse approximation (RPWIA) are also displayed. Through comparing the plane wave and the eikonal calculations, thereby keeping all other ingredients of the calculations identical, one can evaluate how the eikonal method

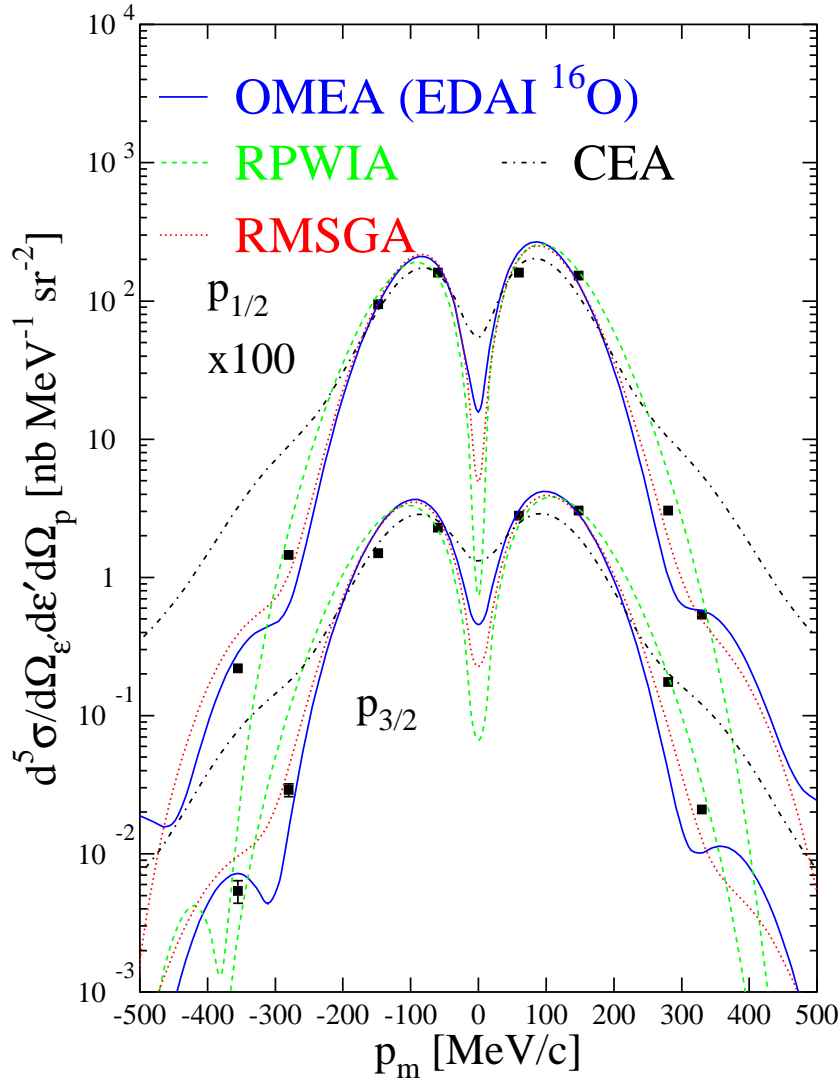


**Figure 6.1** Measured  $^{16}\text{O}(e, e'p)$  cross sections compared to relativistic eikonal, Glauber and RPWIA calculations at  $\epsilon = 2.4$  GeV,  $q = 1$  GeV/c, and  $\omega = 0.439$  GeV in quasiperpendicular kinematics. The calculations use the current operator CC1. The data are taken from Ref. [15].

CC1 operator						
	RPWIA	CEA	OMEA	RMSGGA	Udias	Kelly
$1p_{3/2}$	0.59 (0.56)	0.53 (1.19)	0.96 (1.78)	0.96 (0.75)	0.71	0.67
$1p_{1/2}$	0.53 (0.48)	0.50 (0.58)	0.79 (0.60)	0.80 (0.38)	0.73	0.72
CC2 operator						
$1p_{3/2}$	0.61 (1.59)	0.62 (2.80)	1.01 (3.48)	1.01 (2.19)		
$1p_{1/2}$	0.53 (0.56)	0.57 (1.09)	0.82 (1.04)	0.82 (0.95)		

**Table 6.1** The spectroscopic factors for the  $^{16}\text{O}(e, e'p)$  reaction of Ref. [15], as obtained with a  $\chi^2$  procedure. The reduced  $\chi^2$  (i.e. the  $\chi^2$  per degree of freedom) is given between brackets. The spectroscopic factors obtained by Udias et al. in Ref. [86], and by Kelly in Ref. [45] are also given by comparison.

deals with final state interactions (FSI's). In the eikonal calculations, the dips of the RPWIA calculations are filled in, and, at low missing momenta the RPWIA cross sections are reduced. These two features reflect nothing but the usual impact of the final state interactions on the  $A(e, e'p)$  angular cross sections. The limitations of the consistent eikonal calculations ( $q \gg k_i$ ) are immediately visible at higher missing momenta ( $p_m \geq 250$  MeV/c). Here, the eikonal cross sections largely overshoot both the RPWIA results and the data and should by no means be considered realistic. It is worth remarking that the data closely follow the trend set by the RPWIA curves. As a matter of fact, whereas the eikonal calculations predict huge effects from final state interactions at large transverse missing momenta, the data seem to suggest rather the opposite effect.

One may wonder whether the observed behaviour of the consistent eikonal results at higher missing momenta in Fig. 6.1 is a mere consequence of the small-angle approximation contained in Eq. (5.13), or whether the adopted model assumptions for computing the scattering states is also (partly) at the origin of this pathological behaviour. To address this question, we have performed calculations for various fixed recoil angles  $\theta$  defined as

$$\cos \theta = \frac{\vec{p}_m \cdot \vec{q}}{|\vec{p}_m| |\vec{q}|}. \quad (6.1)$$

The results are displayed in terms of the reduced cross section which is defined in the standard fashion as the differential cross section, divided by a kinematical factor times the ‘‘CC1’’ off-shell electron-nucleon cross section  $\sigma_{eN}^{cc1}$  of Ref. [39]. This cross section is defined as

$$\sigma_{eN}^{cc1} = \sigma_{Mott} \left[ \frac{Q^4}{q^4} w_C + \left( \frac{Q^2}{2q^2} + \tan^2 \frac{\theta_e}{2} \right) w_T \right]$$

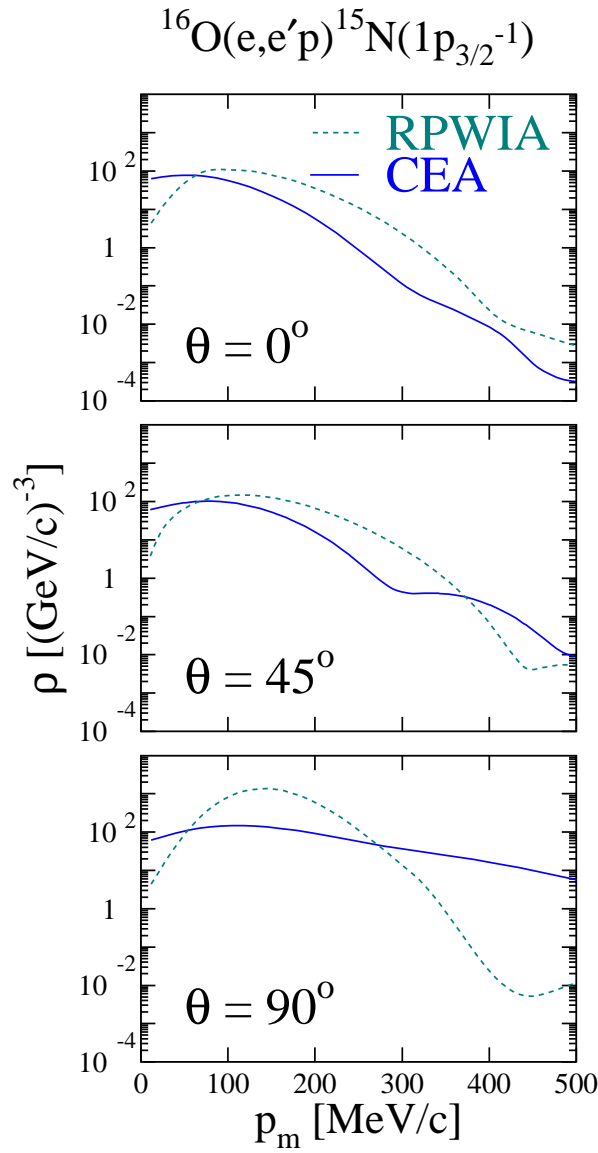


**Figure 6.2** The reduced cross section for the  $^{16}\text{O}(e, e'p)^{15}\text{N}(1p_{3/2}^{-1})$  reaction versus missing momentum at three values of the recoil angle  $\theta$ . A fixed outgoing proton momentum of  $|\vec{k}_f| = 1$  GeV/c was considered. The solid line shows the consistent eikonal calculation, while the dashed one shows RPWIA results.

$$+ \left. \frac{Q^2}{q^2} \left( \frac{Q^2}{q^2} + \tan^2 \frac{\theta_e}{2} \right)^{1/2} w_I \cos \phi + \left( \frac{Q^2}{q^2} \cos^2 \phi + \tan^2 \frac{\theta_e}{2} \right) w_S \right] \quad (6.2)$$

where the conventions of Sec. 2 were adopted. The structure functions are explicitly given by

$$\begin{aligned} w_C &= \frac{1}{4\bar{E}_f\bar{E}} \left[ (\bar{E} + E_f)^2 (F_1^2 + \frac{\bar{Q}^2}{4m^2} \kappa^2 F_2^2) - q^2 (F_1 + \kappa F_2)^2 \right], \\ w_T &= \frac{\bar{Q}^2}{2\bar{E}E_f} (F_1 + \kappa F_2)^2, \\ w_S &= \frac{k_f^2 \sin^2 \theta}{\bar{E}E_f} (F_1^2 + \frac{\bar{Q}^2}{4M^2} \kappa^2 F_2^2), \\ w_I &= -\frac{k_f \sin \theta}{\bar{E}E_f} (\bar{E} + E_f) (F_1^2 + \frac{\bar{Q}^2}{4M^2} \kappa^2 F_2^2), \end{aligned} \quad (6.3)$$

where  $\bar{E} = ((\vec{k}_f - \vec{q})^2 + M^2)^{1/2}$  and  $\bar{Q}^2 = q^2 - \bar{\omega}^2$ , with  $\bar{\omega} = E_f - \bar{E}$ .

For the results of Fig. 6.2 we considered in-plane kinematics at a fixed value of the outgoing proton momentum [ $k_f = 1$  GeV/c] and an initial electron energy of 2.4 GeV. The variation in missing momentum was achieved by changing the momentum transfer  $q$ . For recoil angles  $\theta = 0^\circ$  (“parallel kinematics”) the eikonal calculations do not exhibit an unrealistic behaviour up to  $p_m = 0.5$  GeV/c, which is the highest momentum considered here. With increasing recoil angles, and consequently, growing “transverse” components in the missing momenta the unrealistic behaviour of the eikonal results becomes manifest. Accordingly, the accuracy of the eikonal method based on the small-angle approximation of Eq. (5.13) can only be guaranteed for proton knockout in a small cone about the momentum transfer. A similar quantitative behaviour as a function of the recoil angle to what is observed in Fig. 6.2 was reported in Ref. [7] for  $d(e, e'p)n$  cross sections determined in a Glauber framework. We conclude this discussion with remarking that the eikonal method does not exclude situations with high initial (or, missing) momenta, it only requires that the perpendicular component of the ejectile’s momentum  $\vec{k}_f$  is sufficiently small. It speaks for itself that such conditions are best fulfilled as one approaches parallel kinematics.

At first sight, this observation puts serious constraints on the applicability of the Glauber method, which is based on the eikonal approximation, for modelling the final state interactions in high-energy ( $e, e'p$ ) reactions from nuclei. However, as we noted before, this consistent framework does use purely real scalar and vector potentials. More realistic scattering potentials demand an imaginary part that accounts for the inelastic channels that are open during the reaction process. The Glauber approach effectively includes these inelastic channels and on these grounds one may expect

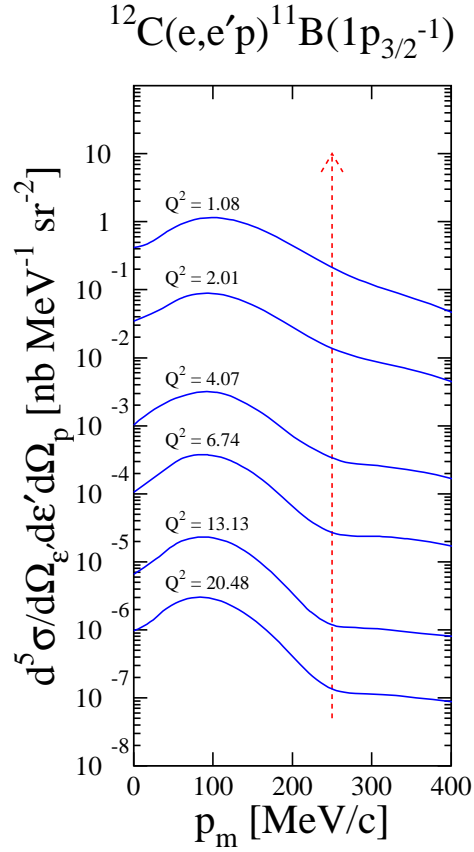


**Figure 6.3** The differential cross section for the  $^{12}\text{C}(e, e'p)^{11}\text{B}(1p_{3/2}^{-1})$  reaction versus missing momentum at six different values for  $Q^2$  (in  $(\text{GeV}/c)^2$ ). Quasielastic conditions and perpendicular kinematics were considered.

that its range of applicability is wider than what is observed here. This matter will be discussed in greater detail in Sec. 6.1.2.

With the eye on defining the region of validity for the eikonal approximation in the consistent approach, we have studied differential cross sections for various  $Q^2$ . In Fig. 6.3, we display the computed differential cross section for the  $^{12}\text{C}(e, e'p)^{11}\text{B}(1p_{3/2}^{-1})$  process against the missing momentum for  $Q^2$  varying between 1 and 20  $(\text{GeV}/c)^2$ . Hereby, quasielastic conditions were imposed. The arrow indicates the missing momentum where the slope of the eikonal differential cross section starts deviating from the trend set by the RPWIA cross section. In the light of the conclusions drawn from the comparison between data and the eikonal curves in Fig. 6.1, the eikonal results should be regarded with care beyond this missing momen-

tum. Furthermore, it is clear that the change in the slope of the angular cross section becomes more and more pronounced as  $Q^2$  increases. It is apparent from Fig. 6.3 that the eikonal differential cross section changes slope at about  $p_m = 250$  MeV/c for all values of  $Q^2$  considered. As a consequence, the momentum of the ejected nucleon varies quite dramatically as one moves up in  $Q^2$ . The uniform behaviour of all curves contained in Fig. 6.3 allows one to write down a relation between the transferred momentum  $\vec{q}$  and the polar scattering angle  $\theta$  :  $|\vec{q}|\theta \leq 250$  MeV/c rad. This simple relation can serve as a conservative guideline to determine the opening angle of the cone in which the outgoing proton momentum has to reside to ascertain that the eikonal approximation produces realistic results. This limitation of the eikonal method can also be inferred from the results contained in Refs. [12, 88]. Indeed, in Figs. 3 and 4 of Ref. [12] one can confirm that the above relation between  $|\vec{q}|$  and  $\theta$  defines the missing momentum at which a sudden change in the  $p_m$  dependence of the calculated cross sections is observed. The above relation can be understood as follows. In quasi-perpendicular kinematics and quasielastic conditions, the missing momentum roughly equals the transverse momentum of the ejected nucleon. With increasing momentum transfer, the longitudinal momentum of the escaping nucleon increases correspondingly while its transverse momentum has to stay smaller than this empirical value of 250 MeV/c. Hence, the sine of the angle between the transferred momentum and the ejectile's momentum has to decrease. Since we are dealing with small angles,  $\sin(\theta)$  can be approximated by  $\theta$ . The opening angle of the cone in which the eikonal approximation is valid, can be inferred to be independent of  $Q^2$  in the Lorentz frame where the ejected nucleon is at rest. When transforming back to the lab frame, lateral dimensions become dilated, and, thus, angles contracted.

### 6.1.2 The Eikonal Approximation with Optical Potentials and the Glauber Multiple Scattering Extension

The selfconsistent results that were presented in the previous section made clear that inelastic mechanisms in the trajectory of the ejected particle affect both the magnitude and the  $p_m$  dependence of the  $A(e, e'p)$  cross sections. Consequently, the CEA cannot be used as a model to extract spectroscopic factors in a reliable manner. It is a common practice in modelling  $A(e, e'p)$  reactions to use optical potentials. It is widely accepted that the errors induced by violating orthogonality and unitarity constraints are of minor importance than the error induced by completely leaving out the inelastic process in the final state.

We now concentrate on eikonal calculations that make use of optical potentials to determine the eikonal phase  $iS(\vec{b}, z)$ . In Fig. 6.1 the RPWIA and consistent eikonal calculations are compared to the eikonal calculations that make use of the complex potentials of Ref. [56]. The spectroscopic factors were taken from the results of Table 6.1.

In general the effect of final state interactions is far weaker compared to the

CEA when using complex optical potentials. This behaviour reflects itself in a number of things. The dips in the RPWIA cross sections, for example, are much less filled in compared to the consistent approach, while at high  $p_m$  the cross section falls much steeper. Another very interesting feature is the enhancement of the spectroscopic factors. These values have to be compared with the values obtained by other calculations performed by Udias et al. [86] and Kelly [45], and that were published in Ref. [15]. They can also be found in Table 6.1. These two calculations made use of the RDWIA approach and resulted in smaller spectroscopic factors. One possible explanation, apart from the different solution of the Dirac equation, is that we have not included contributions stemming from the  $1d_{5/2}$  and  $2s_{1/2}$  particle levels, which influence the experimental  $1p_{3/2}$  particle strength. In Ref. [89] the spectral function of the  $^{16}\text{O}(e, e'p)^{15}\text{N}$  was measured in quasielastic parallel kinematics, and it was found that a 28 % reduction of the valence  $1p$  shell strength was caused by the  $2s1d$  shell.

A striking feature of Fig. 6.1 is that the usage of optical potentials extends the applicability of the eikonal method to larger values of the proton angle. For the range considered here, the eikonal results using optical potentials provide a fair description of the data. The available amount of exclusive  $A(e, e'p)$  data at high  $Q^2$  and  $p_m$  is rather modest. Nonetheless, on the basis of our model calculations it appears safe to state that after implementing inelastic mechanisms in the description of the final state, the applicability of the eikonal method gets extended beyond the  $p_m \leq 250$  MeV/c limit which was observed in the CEA approach. This is also a justification of the Glauber method, which is basically a multiple-scattering extension of the eikonal approximation with complex scattering potentials.

As can be seen in Table 6.1 the Glauber and eikonal optical potential approach essentially give the same spectroscopic factors. The agreement between the eikonal and the Glauber calculations at low missing momenta is almost perfect; in the range  $-200 \text{ MeV}/c \leq p_m \leq 200 \text{ MeV}/c$ , the differences are negligible, apart from the region of parallel kinematics. For vanishing missing momenta the Glauber calculations follow more closely the trend set by the RPWIA results. This drop at low missing momenta is more pronounced for the  $1p_{1/2}$  level than for the deeper lying  $1p_{3/2}$  level, which proves that the longer the way that the struck proton has to travel to reach the surface of the nucleus, the more it gets distorted on its way out of the nucleus. At higher missing momenta the Glauber results gradually shift away from the eikonal ones in the direction of the data, thereby producing an even more accurate description of the experimental results than the eikonal results do. The trend set by the RPWIA curves is followed more closely, but the tendency to underestimate the data is still present, albeit very weakly.

The difference between the optical model and the Glauber predictions for the

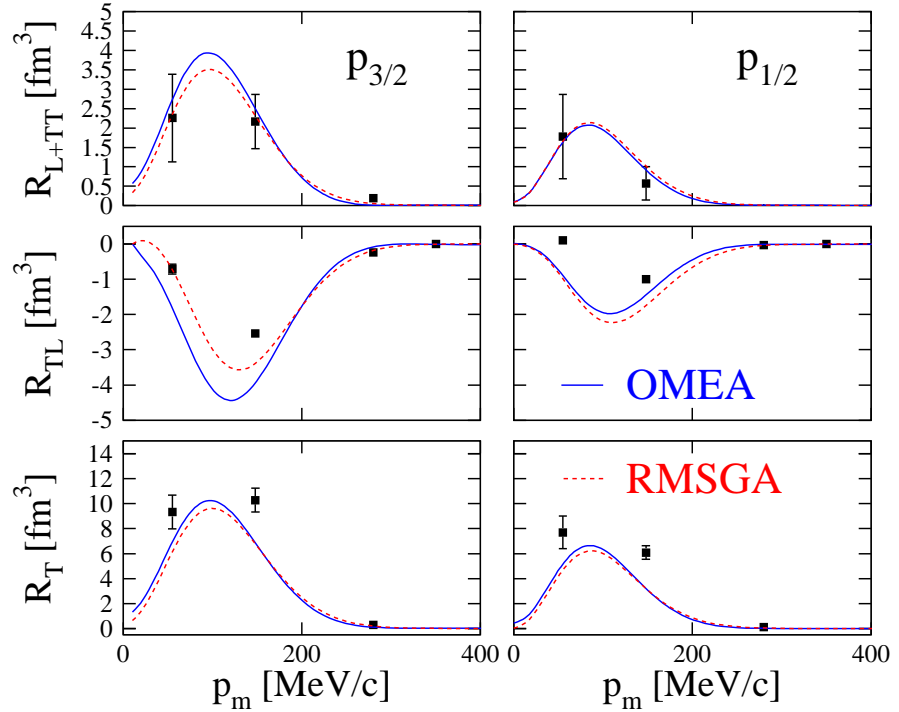


**Figure 6.4** Measured  $R_{L+TT}$ ,  $R_{TL}$  and  $R_T$  structure functions, and the corresponding eikonal (OMEA) and Glauber (RMSGGA) calculations. The data are taken from Ref. [15].

differential cross sections is rather modest. We will now turn to the different polarized structure functions of the JLAB experiment of Ref. [15]. In Fig. 6.4, the response functions  $R_{L+TT}$ ,  $R_{TL}$  and  $R_T$  are presented as a function of missing momentum for knockout from the p-shell levels. Since the cross sections were measured in perpendicular kinematics, it was not possible to isolate the longitudinal response function  $R_L$ . Instead, the combination  $R_{L+TT} = R_L + \frac{v_{TT}}{v_L} R_{TT}$  was extracted. We note that the conventions used for defining the response functions by the authors of Ref. [15] is somewhat different from ours. This difference is kinematical from origin and independent from the missing momentum  $p_m$ . We have applied the appropriate scaling factor ( $\sim 0.41$ ) to our calculations in Fig. 6.4.

We start by making a few general observations that apply to both methods. As can be seen in Fig. 6.4, both calculations are able to reproduce the necessary strength for the longitudinal response function; the agreement with the data is rather good. We note that the contribution of the  $R_{TT}$  structure function is small ( $< 10\%$ ).



defined by the following set of unit vectors and is shown in Fig. 6.5

$$\begin{aligned}\vec{l} &= \frac{\vec{k}_f}{|\vec{k}_f|} \\ \vec{n} &= \frac{\vec{q} \times \vec{k}_f}{|\vec{q} \times \vec{k}_f|} \\ \vec{t} &= \vec{n} \times \vec{l}\end{aligned}\tag{6.4}$$

Note that for coplanar kinematics  $\vec{n}$  determines the y-axis of the reference frame. The escaping nucleon polarization observables can be determined through measuring ratios. The induced polarization can be addressed with unpolarized electrons (i = n,l,t)

$$P_i = \frac{\sigma(s_N^i = \uparrow) - \sigma(s_N^i = \downarrow)}{\sigma(s_N^i = \uparrow) + \sigma(s_N^i = \downarrow)},\tag{6.5}$$

whereas the polarization transfer also requires polarized electron beams (i = n,l,t)

$$P'_i = \frac{[\sigma^+(s_N^i = \uparrow) - \sigma^-(s_N^i = \uparrow)] - [\sigma^+(s_N^i = \downarrow) - \sigma^-(s_N^i = \downarrow)]}{[\sigma^+(s_N^i = \uparrow) + \sigma^-(s_N^i = \uparrow)] + [\sigma^+(s_N^i = \downarrow) - \sigma^-(s_N^i = \downarrow)]},\tag{6.6}$$

where  $s_N^i = \uparrow (\downarrow)$  denotes that the ejected hadron is spin-polarized in the positive (negative) i direction (i = n,l,t) and where the plus (minus) sign in  $\sigma^\pm$  denotes the helicity  $h = \pm 1$  of the electron impinging on the target nucleus.  $\sigma^\pm(s_N^i)$  is then a shorthand notation for the differential cross section for an electrodisintegration process initiated by an electron with helicity  $h = \pm 1$  and for which the ejectile is detected with a spin polarization characterized by  $s_N^i$ . One distinct advantage of the polarization observables is that, unlike the response functions, they are independent of the applied spectroscopic factors, which cancel out in a natural way.

In Fig. 6.6, we have plotted the calculations for the  $P'_l$  and  $P'_t$  observables for the  $^{16}\text{O}(\vec{e}, e'\vec{p})$  experiment of Ref. [15]. We note that the  $P'_n$  is identically zero in the kinematics considered here. These polarization observables are expected to be rather insensitive to final-state interactions. This is confirmed by our calculations. For the  $P'_l$  observable the Glauber predictions are almost indistinguishable from the RPWIA ones. The OMEA prediction follows somewhat more closely the trends set by the data. At contrast, both methods predict equivalent trends for the  $P'_t$  observable, and there's no real preferred calculation. Both methods follow the trend set by the RPWIA curve, reflecting the fact that the  $P'_t$  is indeed rather insensitive to the effects of final state interactions.

The polarization observables can be combined to investigate nucleon form factors. For the free nucleon, the polarization transfer can be written in terms of the form

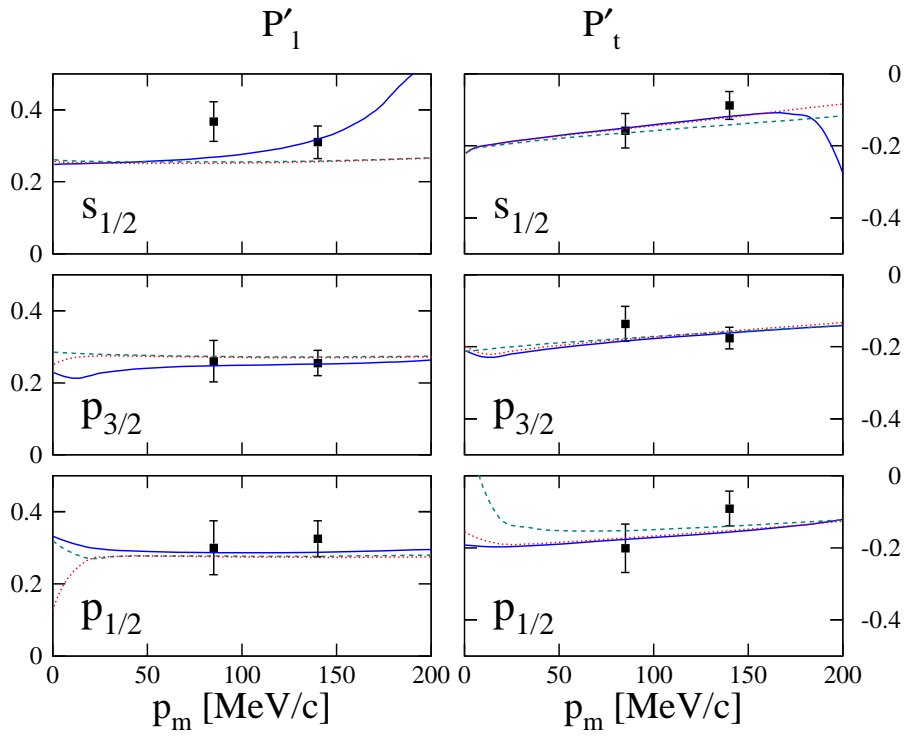


**Figure 6.6** Polarization transfers  $P'_l$  and  $P'_t$  for the  $^{16}\text{O}(e, e'p)$  experiment of Ref. [15]. Calculations for RPWIA (dashed line), eikonal (solid line) and Glauber (dotted line) approximations are plotted. The data are from Ref. [93].

factors as [94, 95]

$$I_0 P'_l = \frac{\epsilon + \epsilon'}{M_p} \sqrt{\tau(1 + \tau)} G_M^2 \tan^2(\theta_e/2), \quad (6.7)$$

$$I_0 P'_t = -2\sqrt{\tau(1 + \tau)} G_M G_E \tan(\theta_e/2), \quad (6.8)$$

$$I_0 = G_E^2 + \tau G_M^2 [1 + 2(1 + \tau) \tan^2(\theta_e/2)], \quad (6.9)$$

$$\tau = Q^2/4M_p^2 \quad (6.10)$$

The ratio of the transferred polarizations is then

$$\frac{P'_t}{P'_l} = \frac{-2M_p}{(\epsilon + \epsilon') \tan(\theta/2)} \frac{G_E}{G_M} \quad (6.11)$$

For a free proton target, the ratio of the polarizations can be used to determine the ratio of the form factors. This ratio is independent of beam polarization provided it is not zero of course. Pioneering work on this terrain was done in the early 90's at SLAC [96, 97]. For nuclear targets the polarization transfer also depends on the nuclear wave functions. In addition they are affected by the final state interactions of the outgoing proton, off-shell effects and relativity. In Fig. 6.7 the ratios of the polarization observables of Fig. 6.6 are compared to the data.

We have already mentioned the pronounced sensitivity of the  $R_{TL}$  response function to the different ingredients that enter into the model calculations. A quantity that reflects this sensitivity is the left-right asymmetry  $A_{LT}$

$$A_{LT} = \frac{\sigma(\phi = 0^\circ) - \sigma(\phi = 180^\circ)}{\sigma(\phi = 0^\circ) + \sigma(\phi = 180^\circ)} = \frac{v_{TL} R_{TL}}{v_L R_L + v_T R_T + v_{TT} R_{TT}}. \quad (6.12)$$

Also this ratio is independent of the spectroscopic factors. In Fig. 6.8 we have plotted the left-right asymmetry for both  $1p_{1/2}$  and  $1p_{3/2}$  knockout from  $^{16}\text{O}$  in the kinematics of Ref. [15]. When discussing the shape of the differential cross sections it was already stressed that the predicted asymmetry between the positive and negative  $p_m$  side was too large. This reflects itself in the calculations predicting too large a  $A_{LT}$  value. Note that above  $p_m \approx 250$  MeV/c the  $A_{LT}$  exhibits a strong sensitivity to FSI effects. Both the Glauber and optical-model approach, albeit showing very different  $p_m$  dependences, reproduce the trend set by the data at high  $p_m$ . Note that the inclusion of FSI effects is essential for an accurate description of the data points at  $p_m = 275$  and 350 MeV/c.

## 6.2 $^{12}\text{C}(e, e'p)^{11}\text{B}$

We also compare our predictions with data from a recent  $^{12}\text{C}(e, e'p)$  SLAC experiment (NE18 experiment) at  $Q^2 = 1.1$  (GeV/c)<sup>2</sup> [98, 99]. The differential cross

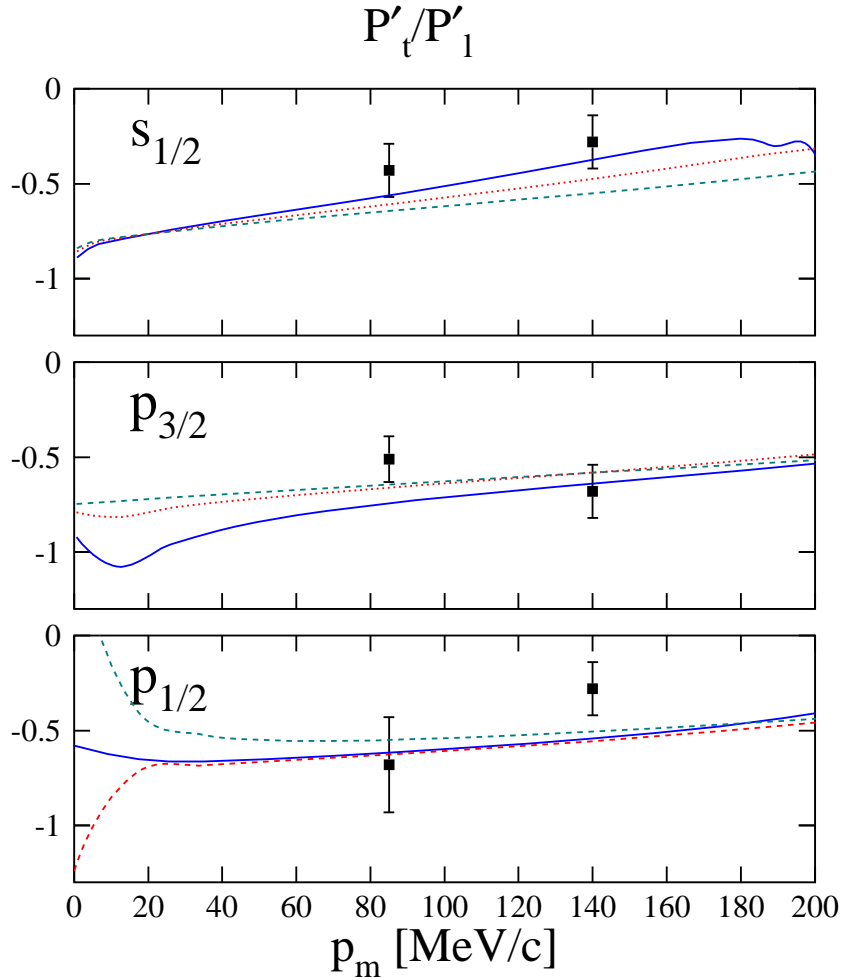


**Figure 6.7** The ratio of the polarization observables  $P'_t/P'_1$  for the  $^{16}\text{O}(\bar{e}, e'\bar{p})$  experiment of Ref. [15] as a function of the missing momentum for  $\epsilon = 2.4$  GeV,  $q = 1$  GeV/c, and  $\omega = 0.439$  GeV, in quasiperpendicular kinematics. The curves refer to predictions obtained within the RPWIA (dashed), the OMEA (solid) and RMSGA (dotted) framework. The data are taken from Ref. [93].

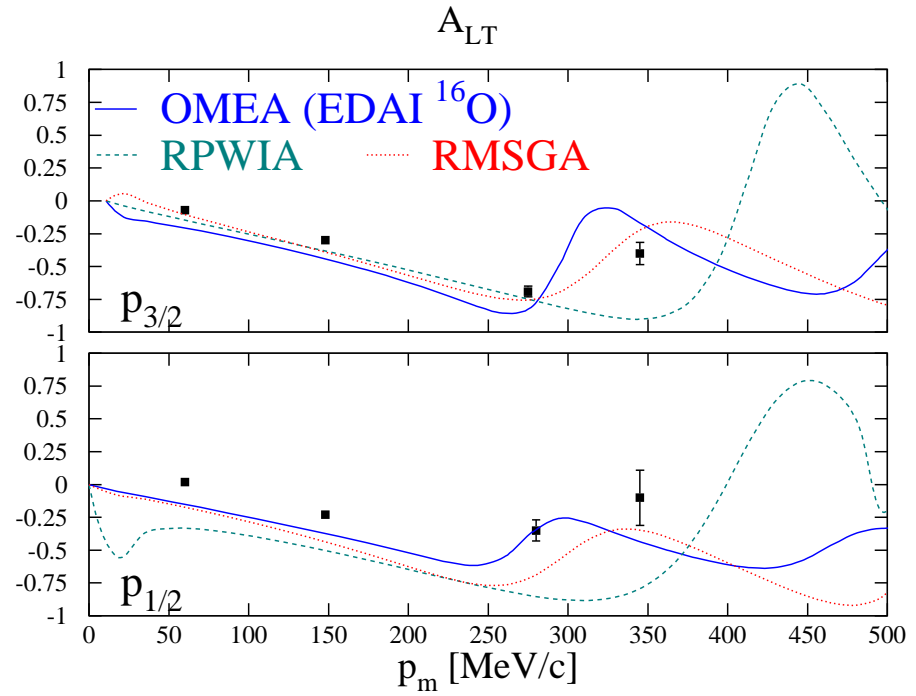


**Figure 6.8** The left-right asymmetry  $A_{LT}$  for both  $1p_{1/2}$  and  $1p_{3/2}$  knockout from  $^{16}\text{O}$  in the kinematics of Ref. [15]. The data were also taken from this reference.

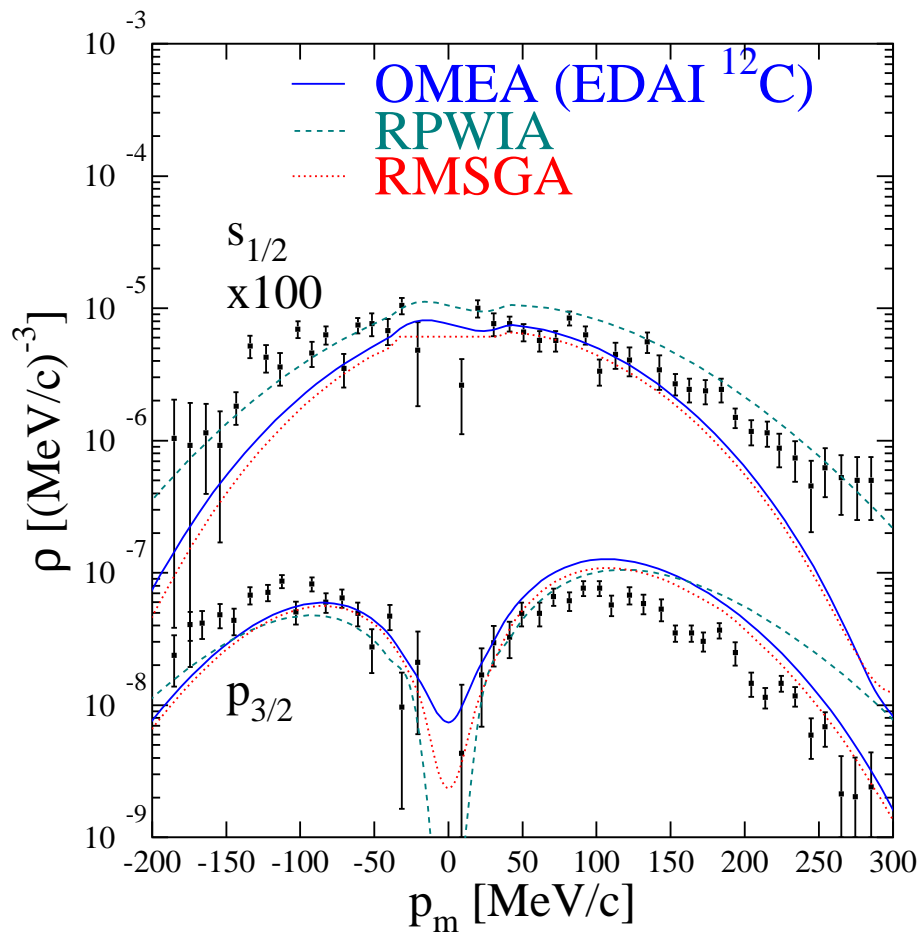


**Figure 6.9** Measured  $^{12}\text{C}(e, e'p)$  reduced cross sections compared to OMEA, RMSGA and RPWIA calculations at  $\epsilon = 2.015$  GeV,  $q = 1.2$  GeV/c, and  $\omega = 0.6$  GeV in quasiperpendicular kinematics. The calculations use the CC1 current operator. The data are from Refs. [98, 99].

section was measured in quasi-perpendicular kinematics for  $\epsilon = 2.015$  GeV,  $q = 1.2$  GeV/c, and  $\omega = 0.6$  GeV.

The same spectroscopic factors for the  $1p_{3/2}$  level were adopted as in Table 6.1, while the factor was kept unity for the deeper lying  $1s_{1/2}$  level. It is very apparent from Fig. 6.9 that a proton ejected from the  $1s_{1/2}$  level undergoes stronger final state distortion than those that are ejected from the  $1p_{3/2}$  level. This reflects the fact that the deeper lying  $1s_{1/2}$  nucleons encounter more obstacles in their way to reach the surface. However, the eikonal picture apparently overestimates this distortion, as the strength in the  $1s_{1/2}$  channel cannot be reproduced entirely, even with unity spectroscopic factors. It is worth remarking here that the data exhibit a negligible asymmetry for this  $^{12}\text{C}(e, e'p)$  reaction. In contrast, when looking back to Fig. 6.1, we see that the data there display a substantial asymmetry for the  $^{16}\text{O}(e, e'p)$  reaction, one of many indications that the  $^{12}\text{C}$  and  $^{16}\text{O}$  differ substantially, although both have a closed shell structure.

At higher missing energies, it can be witnessed that the calculations underestimate both the data and the RPWIA results; the cross section even falls steeper than the plane wave solutions do. The fact that there seems to be a much less adequate description of the deeper lying  $1s_{1/2}$  level, is not very surprising. The main reason for this is that many other processes compete with the proton knockout process, especially in the  $1s_{1/2}$  channel. For instance, two-nucleon knockout reactions generate part of the missing strength. As it is very difficult to experimentally disentangle these competing effects, one cannot expect to adequately describe the  $A(e, e'p)B(1s_{1/2}^{-1})$  reaction by just taking this exclusive one-nucleon knockout into account.

The first experiment measuring the induced proton polarization  $P_n$  on a “heavy” nucleus ( $A > 2$ ) was recently reported by Woo et al. [100]. In this  $^{12}\text{C}(e, e'\vec{p})$  experiment the  $P_n$  was determined at quasifree kinematics for energy and momentum transfer  $(\omega, q) = (294 \text{ MeV}, 756 \text{ MeV}/c)$ , and sampled a missing momentum range of 0 - 250 MeV/c. The results of these measurements for both knockout from the  $1s_{1/2}$  and the  $1p_{3/2}$  bound level are shown in Fig. 6.10, along with our theoretical results. The excellent agreement of the Glauber results with the experimental data is striking. This comes a bit as a surprise, since one would expect a potential model to be more adequate to describe reactions in the lower energy regime.

In the following sections we will more closely inspect the  $Q^2$  evolution of various effects. Special attention will be paid to the differences between the predictions obtained in the Glauber (RMSGGA) and the optical model (OMEA) approach. At higher energies, potential models do not appear to be appropriate as the NN scattering process becomes highly inelastic. We remind the reader that global optical potential fits to elastic proton-nucleus scattering data are not available for proton

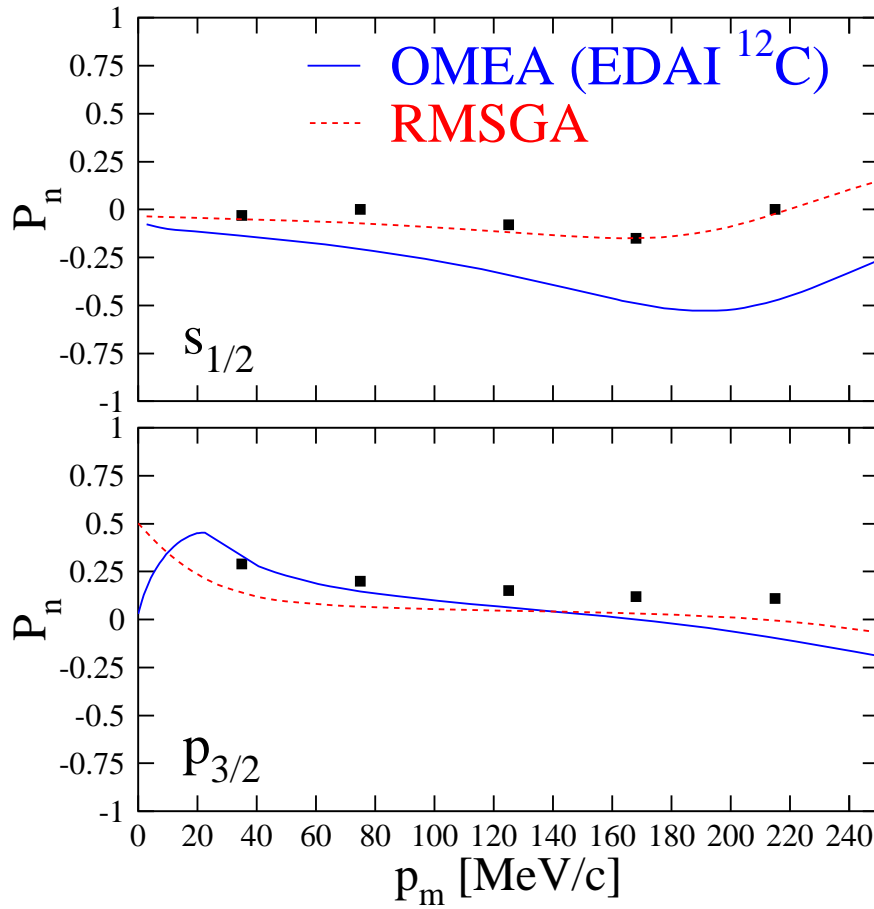


**Figure 6.10** Induced polarization of the knocked-out proton in the  $^{12}\text{C}(e, e'p)^{11}\text{B}$  reaction. The energy of the incident electron was 579 MeV, with constant  $q-\omega$  kinematics. The data are from Ref. [100].

kinetic energies larger than 1 GeV.

---

## Chapter 7

# Off-Shell Ambiguities

---

A major point of concern in any  $A(e, e'p)B$  calculation are the ambiguities regarding the off-shell electron-proton coupling. Most multi-body calculations do not obey current conservation and as outlined in Sec. 4, a variety of prescriptions have been proposed to partially cure this deficiency. Any attempt to address off-shell effects from the microscopic point of view seems to fail at some point.

In this section we will attempt to quantify the ambiguities caused by the use of different current operators and the methods employed to restore current conservation. Hereby, we will concentrate, not only on differential cross sections and structure functions, but also on polarization observables and left-right asymmetries. A key issue in these considerations will be the  $Q^2$  dependence of the off-shell ambiguities. We adopt a heuristic view and estimate the sensitivity of the calculated observables by comparing the results obtained with different viable prescriptions for the electron-proton coupling. These investigations will allow us to put forward favorable choices for the current operators that produce reaction observables which are reasonably stable against minor changes.

We start our investigations into the role of off-shell ambiguities by considering the  $^{16}\text{O}(e, e'p)$  differential cross section at  $Q^2 = 0.8 \text{ (GeV/c)}^2$  and  $\omega = 0.439 \text{ GeV}$ , in quasi-perpendicular kinematics. Fig. 7.1 compares the predictions for the differential cross section for various choices of the current operator. This is done by comparing the predictions relative to the CC2 results. In line with other investigations [41, 42, 101], we find that the ambiguities grow with increasing missing momenta. This is not so surprising and can be understood in the following sense. Short-range and tensor forces give rise to strong nucleon correlations among the nucleons in the mean field, with the result that the Fermi surface is smeared out significantly. This means that relatively high excited states are present and contribute to the high missing

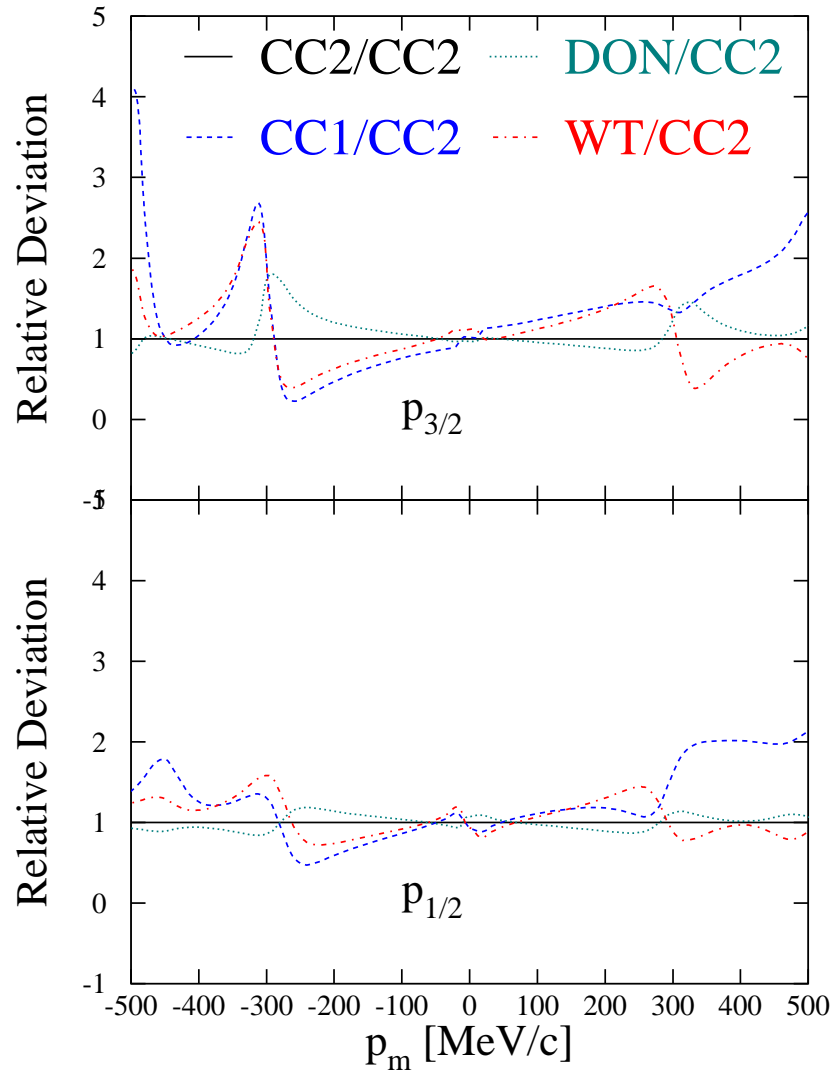


**Figure 7.1** The sensitivity of relativistic eikonal calculations for the  $^{16}\text{O}(e, e'p)$  experiment of Ref. [15]. Plotted are the ratios of the differential cross sections relative to the cross section obtained with the CC2 current operator.

momentum region. Since these excited states are expected to be largely off-shell, it is only natural that the off-shell ambiguities manifest themselves more strongly in this region of phase space. One can estimate the off-shellness of a particle as follows. The actual energy transfer to the nucleon  $\omega$  is determined by the electron kinematics. Assuming that the struck nucleon was on its mass shell, it would have an energy  $E_{on}$  equal to  $(\vec{p}_m^2 + M^2)^{1/2}$ . The energy transfer  $\omega'$  which one would have in that case is given by

$$\omega' = E_f - E_{on} , \quad (7.1)$$

where  $E_f$  is the escaping particle's energy. The difference,  $\delta\omega$

$$\delta\omega = \omega - \omega' \quad (7.2)$$

is a measure for the off-shellness and a quantity which grows with increasing  $p_m$ .

Figs. 7.2 and 7.3 show the predictions for the structure functions that contribute to the differential cross sections shown in Fig. 7.1. The results are obtained within the framework of the relativistic eikonal model and utilize the EDAI  $^{16}\text{O}$  optical potentials of Ref. [56]. Among the infinite number of possible recipes for the off-shell proton-electron coupling we have selected four that are frequently used in literature. They are the commonly used CC1 (Eq. (4.2)) and CC2 (Eq. (4.3)) current operators, the operator proposed by Donnelly et al. (Eq. (4.10)), and the operator that was constructed via the Ward-Takahashi identity (Eq. (4.11)). Current conservation was imposed by either modifying the longitudinal component of the vector current operator (hereafter denoted as the ‘‘J0 method’’), or by modifying the charge operator (hereafter denoted as the ‘‘J3 method’’), along the lines of Eqs. (4.5) and (4.7), respectively. Note that for the operator of Eq. (4.10), both methods yield the same results, since, by construction, this operator is current conserving, regardless of the method adopted to compute the initial and final wave functions.

Turning one's attention to the results of Figs. 7.2 and 7.3, one immediately observes that the calculated  $(e, e'p)$  observables are far from independent from the choices made with regard to the electron-proton coupling. We first look at the differences between the J0 and the J3 method. Obviously, the transverse  $R_T$  and  $R_{TT}$  structure functions are insensitive to whether the J0 or J3 scheme is adopted, as they only involve a modification of the purely longitudinal and the charge component. Looking at the  $R_L$  response function, we see that the CC1 current operator, for example, produces results in the J3 method that are much bigger than the ones in the J0 method. A similar observation applies to the ‘‘WT’’ operator. For the  $R_L$  response all current operators produce comparable results in the J0 scheme. The deviations become sizeable though in the J3 scheme, favoring the  $J_z \rightarrow (\omega/q)J_0$  substitution, as it turns out that the purely longitudinal channel is then insensitive to the choice of the adopted operator.

In the transverse responses  $R_T$  and  $R_{TT}$ , all couplings but the CC1 one produce the same results. The CC1 results are identical in the J0 and J3 scheme. A response

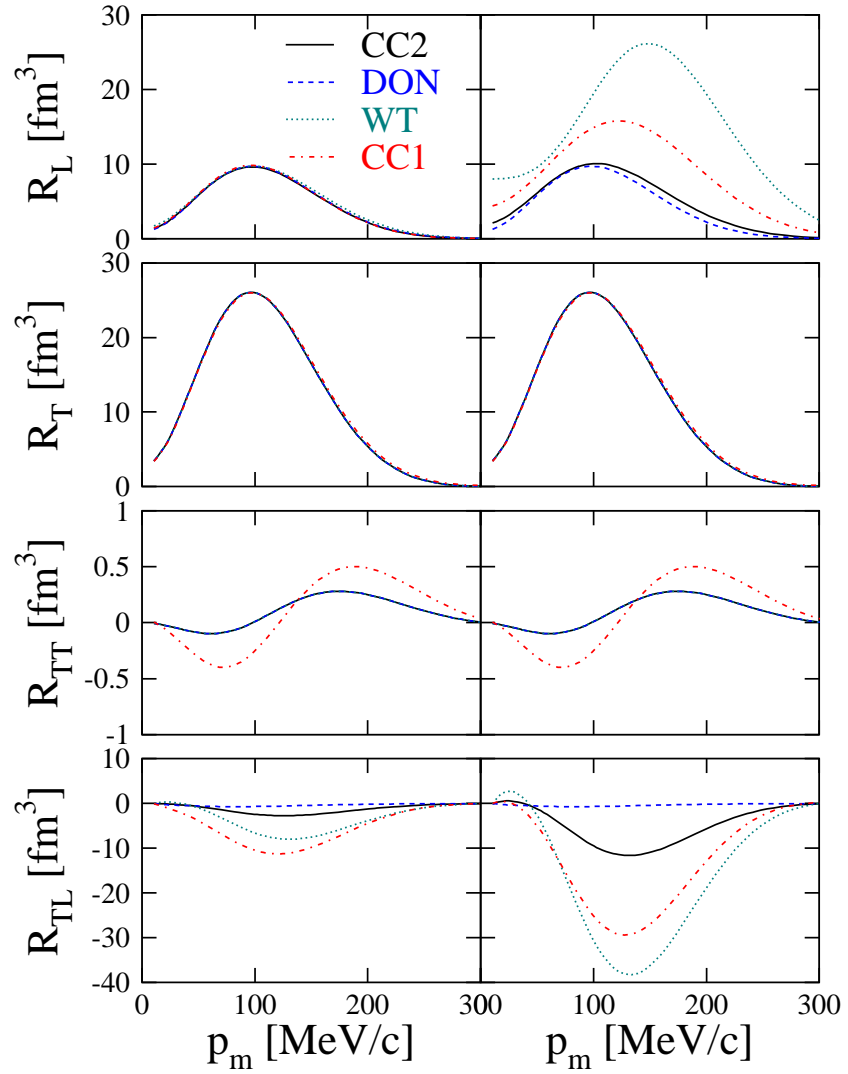


**Figure 7.2** The different structure functions versus missing momentum for  $1p_{3/2}$  knockout from  $^{16}\text{O}$  in the kinematics of Ref. [15]. The calculations in the left column imposed current conservation by replacing the longitudinal component of the vector current operator (Eq. (4.5)), while for the results in the right column the charge density operator was modified according to Eq. (4.7). The curves refer to the different off-shell prescriptions as they were introduced in Sec. 4.

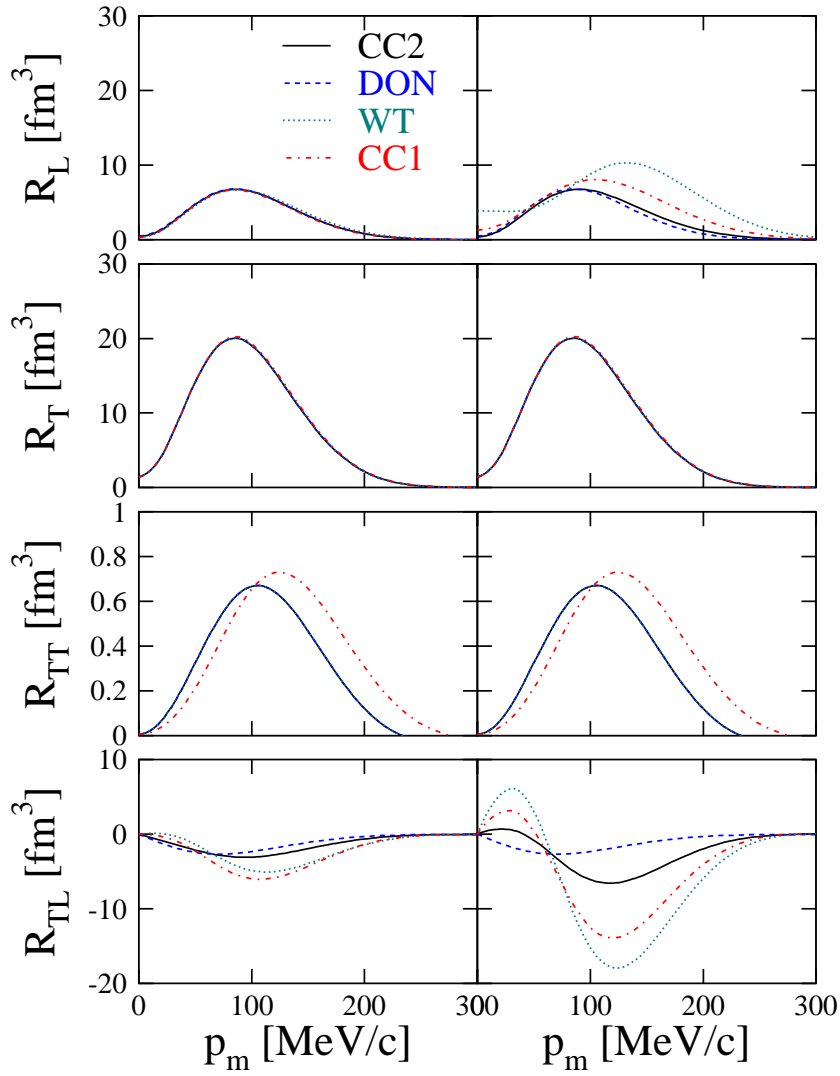


**Figure 7.3** Same as in Fig. 7.2, but for  $1p_{1/2}$  knockout.

function of particular interest here is the longitudinal-transverse one. As we have stressed several times before, of all structure functions the  $R_{TL}$  response function exhibits the greatest sensitivity to any change in the theoretical framework in which it is calculated. It can be inferred from Figs. 7.2 and 7.3, that ambiguities are now introduced in both schemes, although they are (again) much larger in the J3 scheme. The large values for the  $R_{TL}$  response function obtained with the CC1 and the WT current operator confirms the somewhat odd behaviour of the differential cross section at high missing momenta in Fig. 7.1.

Combining the above comments on the gauge sensitivity of the operators, we are inclined to give preference to the J0 scheme. Indeed, within the J0 scheme, the results for different operators stay in one another's proximity. When comparing J0 and J3 calculations for one particular operator, we can only attribute a more robust behaviour to the most-widely used CC2 current operator. Evidently the current operator of Eq. (4.10) is insensitive to gauge restoration schemes.

With increasing  $Q^2$  and the corresponding decreasing distance scale, the off-shell ambiguities in the photon-nucleus coupling are expected to decline and the impulse approximation is believed to become increasingly accurate. In an attempt to make these statements, which are based on physical intuition, more quantitative, we have calculated  $^{12}\text{C}(e, e'p)$  structure functions corresponding with a quasi-elastic situation of really high four-momentum transfer :  $\epsilon = 5120$  MeV/c,  $q = 4490$  MeV/c and  $\omega = 3664$  MeV. Global parametrizations of the complex potential model are only available for proton kinetic energies up to  $\sim 1$  GeV/c. Therefore, the only available framework for treating the final state interactions is the Glauber method. In Figs. 7.4 and 7.5 our predictions for the four unpolarized structure functions are shown for calculations using different current operators and gauge restoring schemes.

Figs. 7.4 and 7.5 illustrate that the off-shell ambiguities are indeed modest as one moves into kinematic regimes where  $Q^2$  is large. Not only produce all four current operators within one scheme almost identical results, the differences between the J0 and the J3 approach are almost vanishing. For the  $R_L$  and  $R_T$  structure functions, all calculations, but the "WT" one, produce analogous results. At higher energies, calculations using the "WT" current operator of Eq. (4.11) predict unrealistically high cross sections and structure functions. This should be attributed to the fact that the operator of Eq. (4.11) is plagued by the occurrence of a term which lacks an electromagnetic form factor. Hence, the operator of Eq. (4.11) does not account for the decreasing nucleon elastic form factor when smaller distance scales are probed. Consequently, we will dismiss the operator of Eq. (4.11) as a viable alternative for the description of the electron-nucleon coupling. For the  $R_{TT}$  and  $R_{TL}$  responses, the predictions obtained with the other six operator combinations are rather close. Again, the greatest ambiguities persist in the TL response. As was already the case in Figs. 7.2 and 7.3, the "DON" current predicts very low values for the  $R_{TL}$ . Calculations at even higher energies confirm this behaviour. Based on this observation, and on the fact that the operator of Eq. (4.10) was constructed in a rather artificial

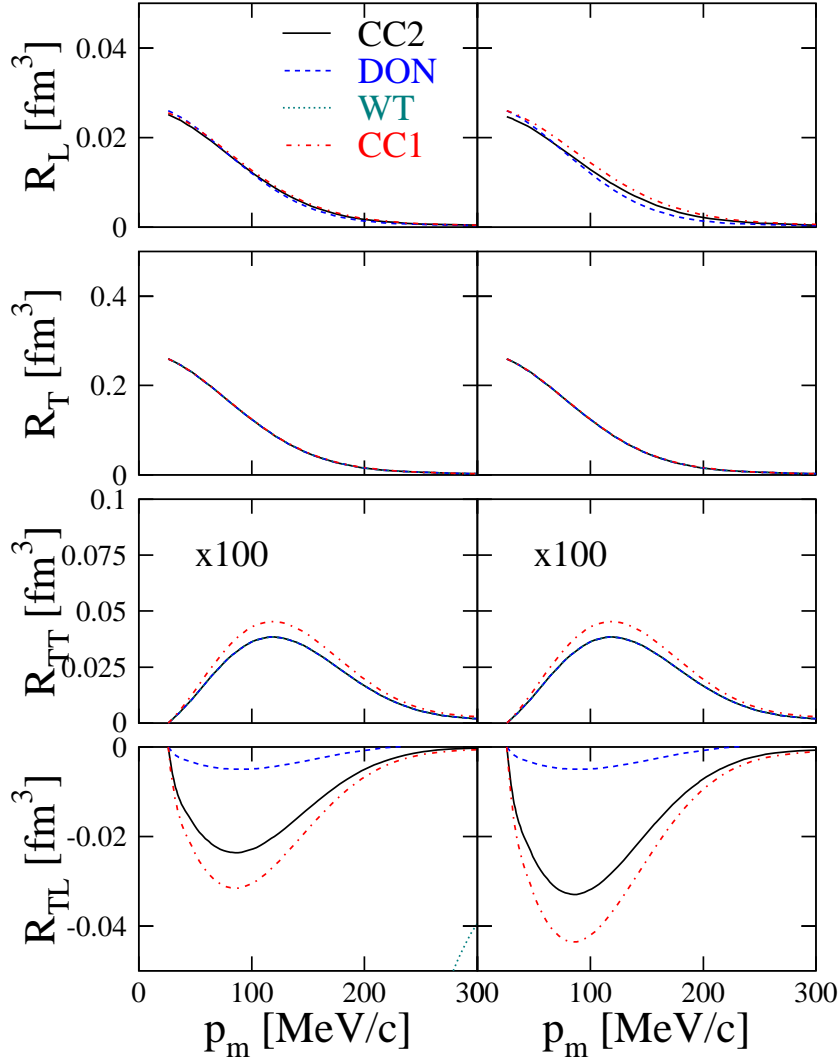


**Figure 7.4** The different structure functions versus the missing momentum for  $1s_{1/2}$  knock-out from  $^{12}\text{C}$  for  $\epsilon = 5120$  MeV/c,  $q = 4490$  MeV/c and  $\omega = 3664$  MeV, under quasi-elastic conditions. The calculations in the left column imposed current conservation by replacing the longitudinal component of the vector current operator (Eq. (4.5)), while for the results in the right column the charge density operator was modified according to Eq. (4.7). The curves refer to the different off-shell prescriptions as they were introduced in Sec. 4.

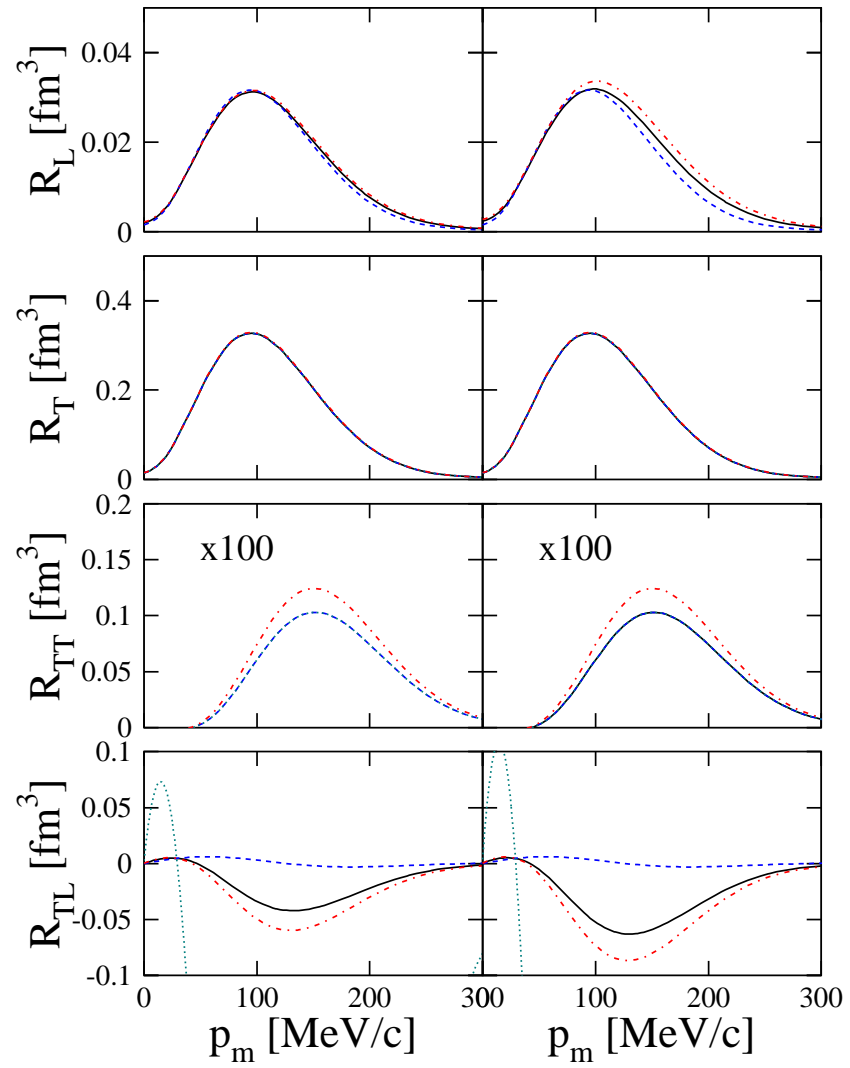


Figure 7.5 Same as in Fig. 7.4, but for  $1p_{3/2}$  knockout.

manner, we will from here on only consider the CC1 and CC2 current operators.

The results shown in Figs. 7.4 and 7.5 suggest that the impulse approximation becomes increasingly accurate. In order to investigate the degree and rate to which this virtue may be realized, we have performed calculations in a wide  $Q^2$  range of  $0.15 \leq Q^2 \leq 20$  (GeV/c)<sup>2</sup>. We use two techniques to estimate the sensitivity to off-shell ambiguities as a function of  $Q^2$ . First, results computed with the J0 and J3 method are compared. Second, predictions with various choices for the electron-proton coupling are confronted with one another. The validity of the impulse approximation is then established whenever the final result happens to become independent of the adopted choice for the electron-nucleon coupling. In order to assess the degree to which this independence is realized, we have considered ratios of structure functions for some fixed kinematics but calculated with different choices for the electron-proton coupling. As a benchmark calculation, we have computed  $^{12}\text{C}(e, e'p)^{11}\text{B}(1p_{3/2}^{-1})$  observables in quasielastic kinematics for several values of the four-momentum transfer.

Fig. 7.6 shows for several observables the ratio of the values obtained with the J3 scheme to the corresponding predictions with the J0 method. Fig. 7.7 shows the ratio of the strengths obtained with the CC1 vertex function compared to the corresponding predictions with the CC2 form. We have chosen to perform these kind of calculations for the peaks in the missing momentum range,  $p_m \sim 100$  MeV/c, where the relative differences are large. We remark that in the limit of vanishing off-shell effects, these ratios should equal one. It is indeed found that the calculations that are based on the substitution  $J_z \rightarrow (\omega/q)J_0$  tend to converge to those based on the substitution  $J_0 \rightarrow (q/\omega)J_z$  with increasing energy transfer. The predictions with the different prescriptions also converge to each other as the energy is increased. This feature is most apparent in the transverse response  $R_T$ , which dominates the cross section at sufficiently high energies. *It appears thus as if off-shell ambiguities, speaking in terms of strengths and absolute cross sections, are of far less concern at higher  $Q^2$  than they used to be in the  $Q^2 \leq 1$  (GeV/c)<sup>2</sup> region, where most of the data have been accumulated up to now.* The interference structure functions  $R_{TT}$  and  $R_{TL}$  on the other hand, are subject to off-shell ambiguities that are apparently extending to the highest four-momentum transfers considered here. This feature was already established in Ref. [47] and explained by referring to the large weight of the negative energy solutions in the interference structure functions  $R_{TL}$  and  $R_{TT}$ . For any structure function one can write that

$$R = R_P + R_N + R_C , \quad (7.3)$$

where  $R_P$  ( $R_N$ ) stems from the contribution from the positive (negative) energy projections only, while  $R_C$  is a crossed term containing products of both positive and

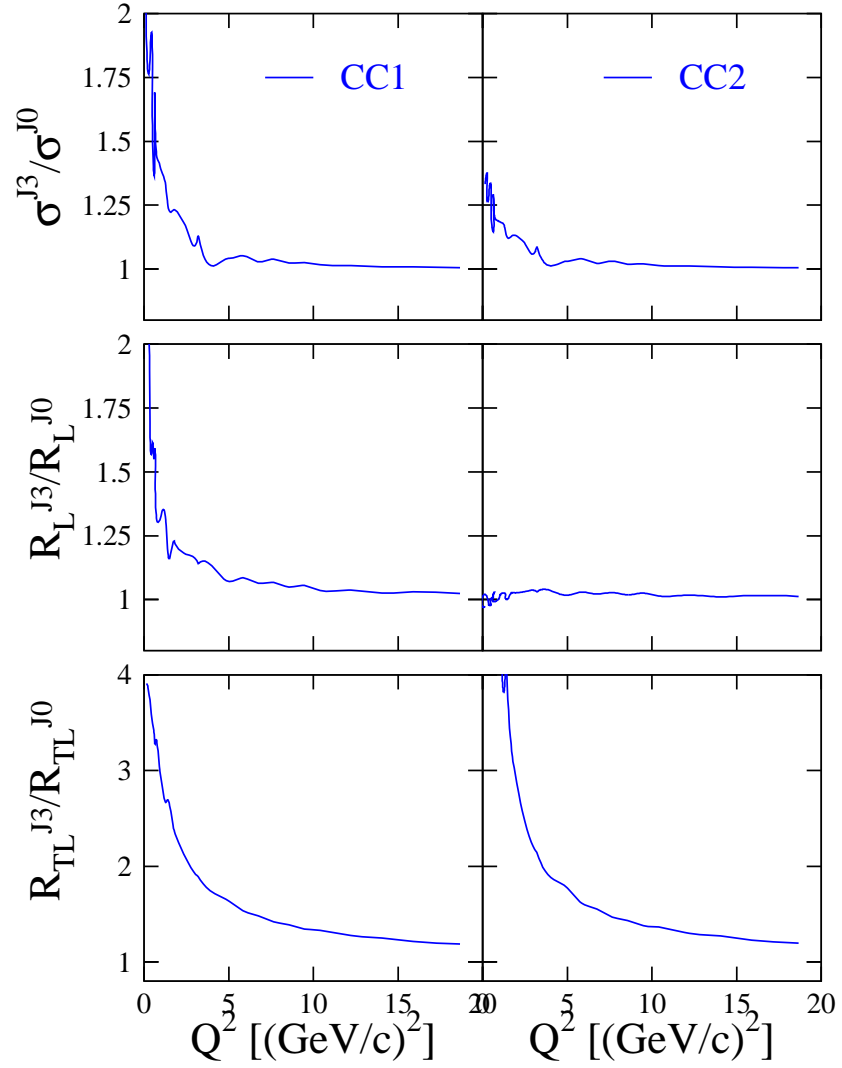


**Figure 7.6** The  $Q^2$  dependence of the sensitivity of the calculated  $(e, e'p)$  structure functions to the choice for the electron-nucleus vertex for  $1p_{3/2}$  knockout from  $^{12}\text{C}$  in quasielastic kinematics. The curves show for the various observables the ratio of the predictions with the J3 method to those obtained with the J0 method. These calculations were performed within the relativistic multiple-scattering Glauber framework for missing momenta of  $p_m \sim 100$  MeV/c, where most of the strength is situated.

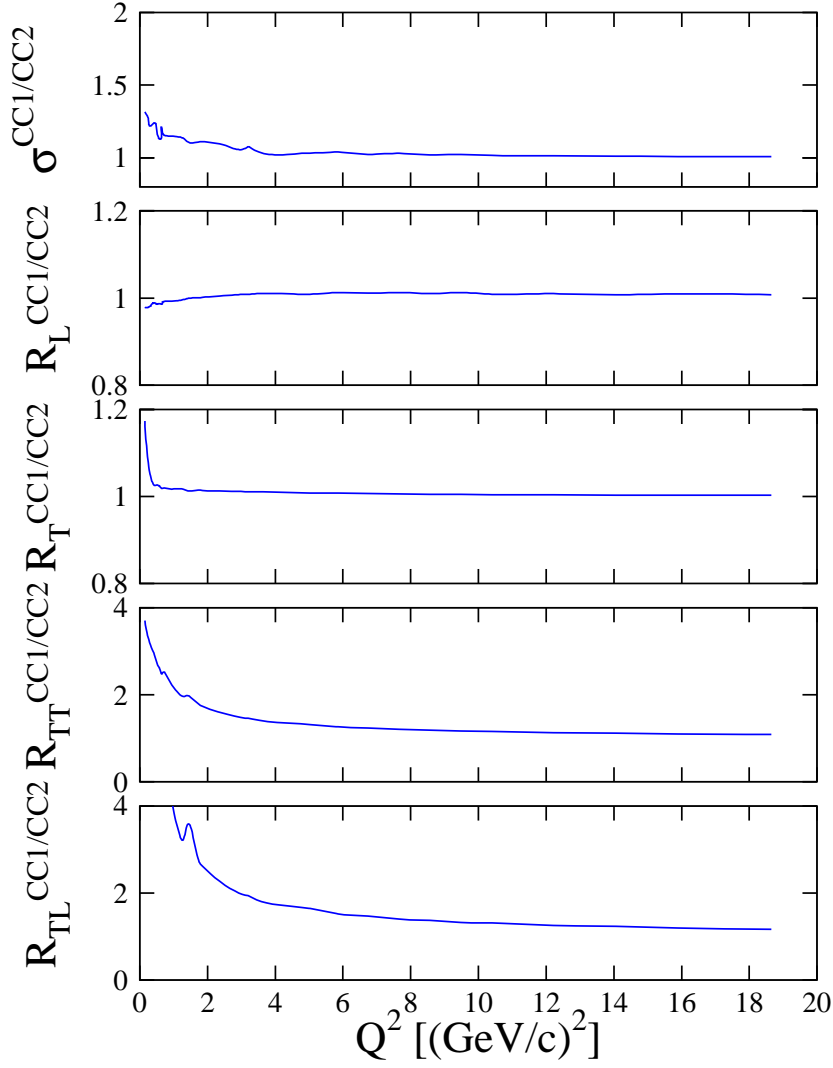


**Figure 7.7** The  $Q^2$  dependence of the sensitivity of the  $(e, e'p)$  structure functions to the choice for the electron-nucleus vertex for  $1p_{3/2}$  knockout from  $^{12}\text{C}$ . The curves display the ratio of the predictions using the vertex function  $\Gamma_{\mu}^{CC1}$  to those using  $\Gamma_{\mu}^{CC2}$ . These calculations were performed within the relativistic multiple-scattering Glauber framework for missing momenta of  $p_m \sim 100$  MeV/c, where most of the strength is situated.

negative energy projections. The  $R_L$  and  $R_T$  structure functions are mainly governed by their positive energy projection, while for the  $R_{TT}$  and  $R_{TL}$  response functions the cross term  $R_C$  can be larger than the positive energy projection  $R_P$ . As the differences between the CC1 and CC2 current operators and the gauge restoration schemes are mainly concentrated in their action upon the lower components of the wave functions, it should not come as a surprise that the ambiguities will be much larger in the responses that generate a significant part of their strength from these negative energy projections.

The observed feature that the cross sections are only marginally sensitive to gauge ambiguities at higher energies can be explained on the basis of the following considerations. A measure for the violation of current conservation is given by [102]

$$q_\mu J^\mu = \omega J_0 - \vec{q} \cdot \vec{J} \equiv \chi, \quad \chi = \delta\omega[J], \quad (7.4)$$

where the quantity  $[J]$  denotes (part of) the nuclear current density (i.e.  $\bar{u}_f \gamma^0 u_i$ ). This can be understood by considering the explicit expression for the CC2 current operator (Eq. (4.3)) for example :

$$\begin{aligned} q_\mu J_{CC2}^\mu &= q_\mu \bar{u}_f \Gamma_{CC2}^\mu u_i, \\ &= F_1 \bar{u}_f (\omega \gamma^0 - \vec{q} \cdot \vec{\gamma}) u_i, \\ &= F_1 (\omega - \omega') \bar{u}_f \gamma^0 u_i, \end{aligned} \quad (7.5)$$

where we have used the definition (7.1) of  $\omega'$ . Rewriting now the matrix element in the Coulomb gauge of Eq. (4.15) in terms of  $\chi$ , leaves us with

$$M_{\text{Coulomb}} = \frac{i}{Q^2} j_\mu J^\mu - \frac{i}{Q^2} \left( \frac{\omega j_0 \chi}{q^2} \right). \quad (7.6)$$

Along similar lines the matrix element in the Weyl gauge of Eq. (4.16) can be rewritten as

$$M_{\text{Weyl}} = \frac{i}{Q^2} j_\mu J^\mu - \frac{i}{Q^2} \left( \frac{j_0 \chi}{\omega} \right). \quad (7.7)$$

With these two expressions we can estimate the relative differences between the cross sections obtained in the J0 and J3 scheme, respectively :

$$\frac{M_{\text{Weyl}}}{M_{\text{Coulomb}}} = \frac{\frac{i}{Q^2} j_\mu J^\mu - \frac{i}{Q^2} \left( \frac{j_0 \delta\omega[J]}{\omega} \right)}{\frac{i}{Q^2} j_\mu J^\mu - \frac{i}{Q^2} \left( \frac{\omega j_0 \chi}{q^2} \right)}. \quad (7.8)$$

For the purpose of getting order of magnitude estimates, we approximate  $j_0[J] \simeq j_\mu J^\mu$  and find

$$\frac{M_{\text{Weyl}}}{M_{\text{Coulomb}}} \simeq \frac{1 - \frac{\delta\omega}{\omega}}{1 - \frac{\omega \delta\omega}{q^2}} \sim \frac{\sigma^{\text{CC1}}}{\sigma^{\text{CC2}}}. \quad (7.9)$$

The relation obtained in Eq. (7.9) illustrates two important findings. First, it shows that for low missing momenta (small  $\delta\omega$ ) the degree of off-shellness will be smaller than for the higher missing momentum range. Second, it indicates that the ambiguities decrease as  $q$  and  $\omega$  increase, thereby making the ratio equal to one.

An interesting physical observable in the context of off-shell effects is the left-right asymmetry, whose  $Q^2$  evolution also confirms the above behaviour. This particular observable is interesting in that it reflects the behaviour of the  $R_{TL}$  response function. Fig. 7.8 shows the left-right asymmetry for the  $^{12}\text{C}(e, e'p)^{11}\text{B}(1p_{3/2}^{-1})$  reaction at four different energies under quasielastic conditions. Indeed, the ambiguities decrease with increasing momentum transfers, and are more significant for higher missing momenta. This concurs with the findings of Ref. [42]. The left-right asymmetry does not depend on spectroscopic factors and has frequently been illustrated to be extremely sensitive to the various ingredients that enter the model calculations. As such it is an interesting variable for discriminating for example between the different gauge choices. Fig. 7.9 shows our predictions for  $A_{LT}$  at  $Q^2 = 0.8$  (GeV/c)<sup>2</sup>. We have performed optical potential and Glauber calculations, considering both the CC1 and CC2 current operator. At first sight, it appears that the data favor the calculations using the CC2 current operator. The CC1 calculations tend to overestimate the measured left-right asymmetry. For the  $1p_{1/2}$  knockout the overall agreement is satisfactory. It is remarkable that for a particular choice for the current operator, the Glauber and optical potential model produce  $A_{LT}$ 's that are close at missing momenta below the Fermi momentum. Once again, it emerges that the optical potential and the Glauber model, despite their very different starting points, yield results that are remarkably similar.

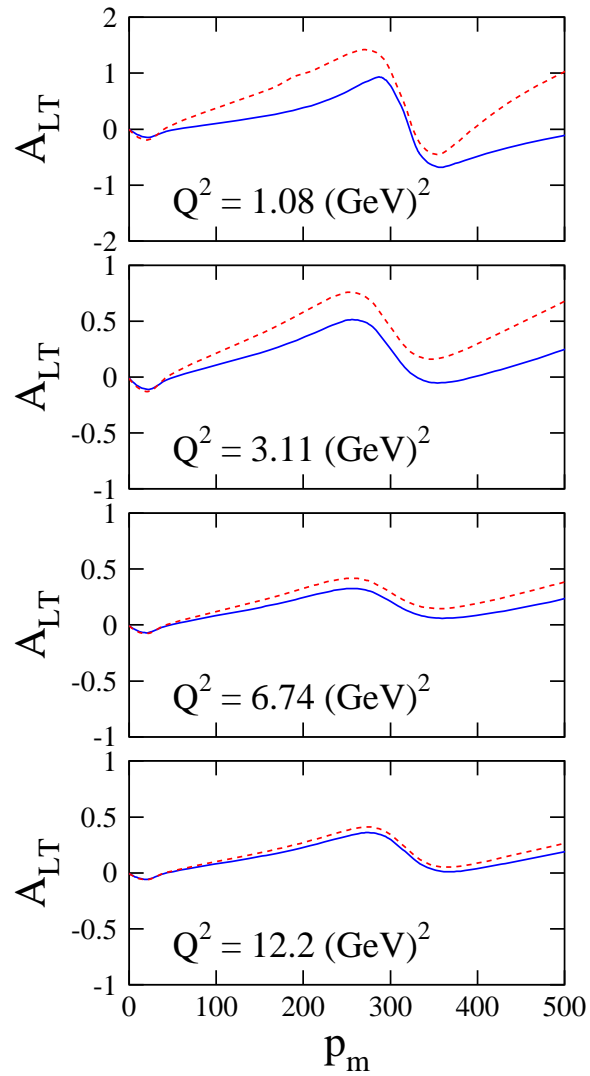


**Figure 7.8** The left-right asymmetry for the  $^{12}\text{C}(e, e'p)^{11}\text{B}(1p_{3/2}^{-1})$  reaction at four different energies, calculated in a Glauber framework. The solid (dashed) curves are obtained with the CC2 (CC1) current operator.

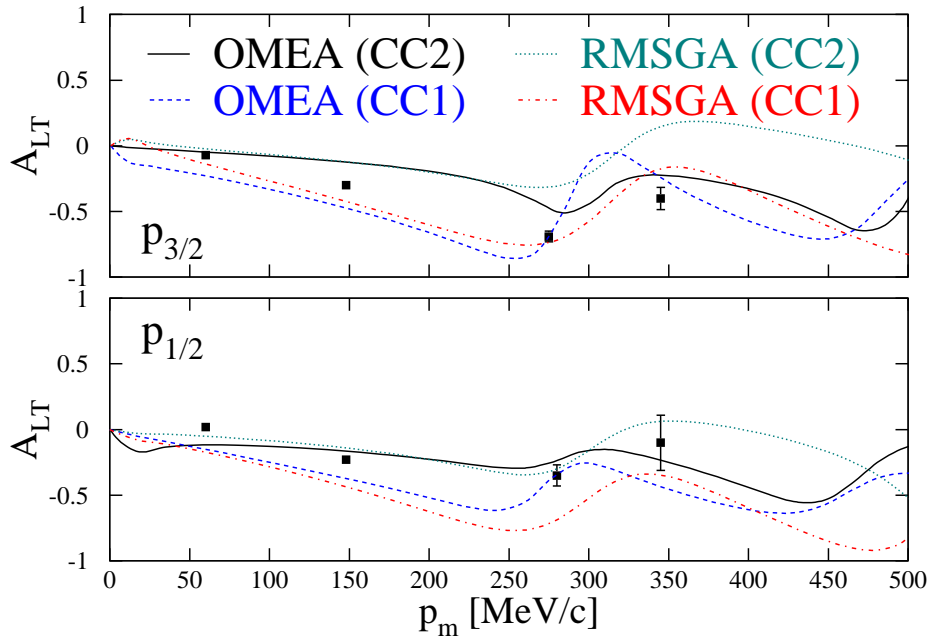


**Figure 7.9** The left-right asymmetry  $A_{LT}$  for both  $1p_{3/2}$  and  $1p_{1/2}$  knockout from  $^{16}\text{O}$  in the kinematics of Ref. [15].



---

## Chapter 8

# Relativistic Effects

---

Recently, there have been several claims for strong indications for genuine (or, “dynamic”) relativistic effects in  $A(\vec{e}, e'\vec{p})$  observables [15, 86, 90, 103]. In an attempt to implement some of these effects in calculations based on a Schrödinger picture, several techniques to obtain a “relativized version” of the electron-nucleus vertex have been developed. In leading order in a  $p/M$  expansion these “relativized” electron-nucleus vertices typically miss the coupling between the lower components in the bound and scattering states. For that reason, we interpret the effect of the coupling between the lower components in the bound and scattering states as a measure of the impact of the relativistic effects.

In Fig. 8.1 the unpolarized structure functions for the  $^{12}\text{C}(e, e'p)$  experiment of Ref. [98] are plotted. It follows from Fig. 8.1 that the effects of relativity are mostly confined to the  $R_{TL}$  and  $R_{TT}$  interference structure functions. The effect of removing the coupling between the lower states is a reduction of the strength in the  $R_{TL}$  and  $R_{TT}$  interference structure functions. At first sight, the dominant  $R_L$  and  $R_T$  channels remain unaffected.

In order to check these findings for other kinematics we have performed a series of calculations for varying  $Q^2$ . We consider quasielastic conditions and study the  $Q^2$  evolution of the structure functions at a fixed value of the missing momentum. We have selected  $p_m = 100$  MeV as this coincides with the situation where the reduced cross section reaches its maximum. Moreover,  $p_m = 100$  MeV corresponds with small proton angles with respect to the direction of the momentum transfer, so that one can safely apply the eikonal approximation. The results of our investigations into the  $Q^2$  evolution of the relativistic effects are contained in Fig. 8.2. It becomes clear that the  $Q^2$  evolution of the relativistic effects is not smooth and some oscillatory behaviour emerges.

Looking first at the results for the total cross section, we observe that the impact of the coupling amongst the lower components first increases, and then tends to converge to zero when higher values of  $\omega$  are reached. Omitting dynamical relativistic

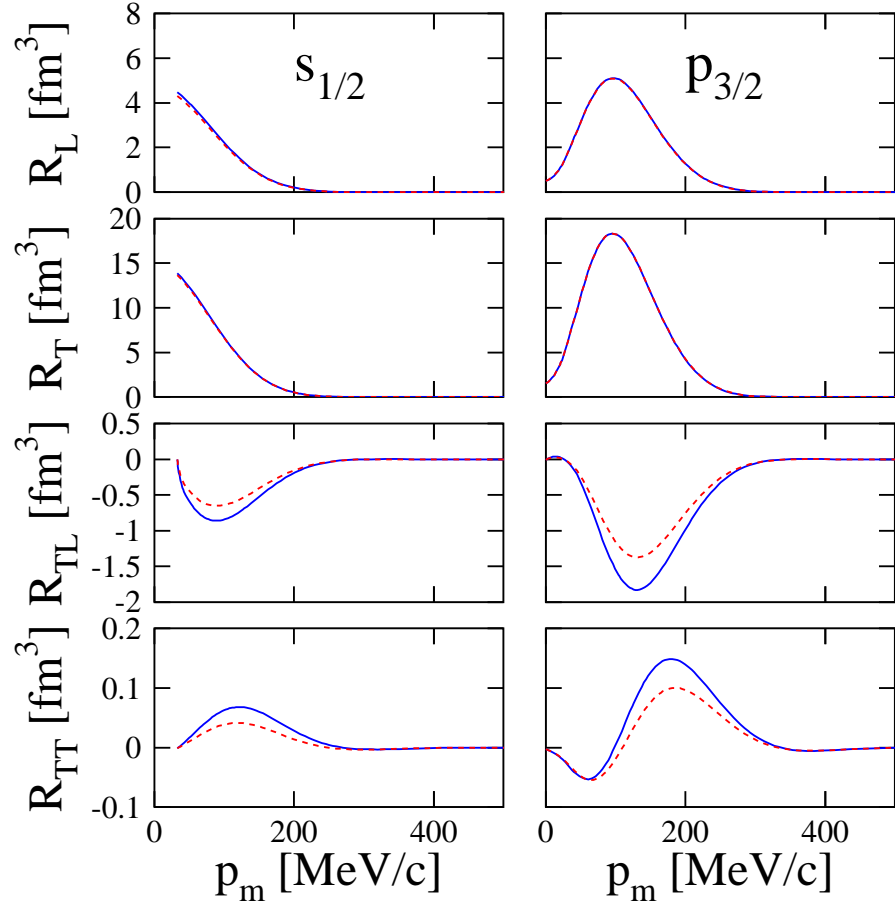


**Figure 8.1** The unpolarized structure functions for the  $^{12}\text{C}(e, e'p)$  knockout experiment of Ref. [98]. The solid line presents fully relativistic eikonal calculations with Cooper optical potentials, while for the dashed results, the coupling between the lower components of the bound and scattering state has been reduced to zero.

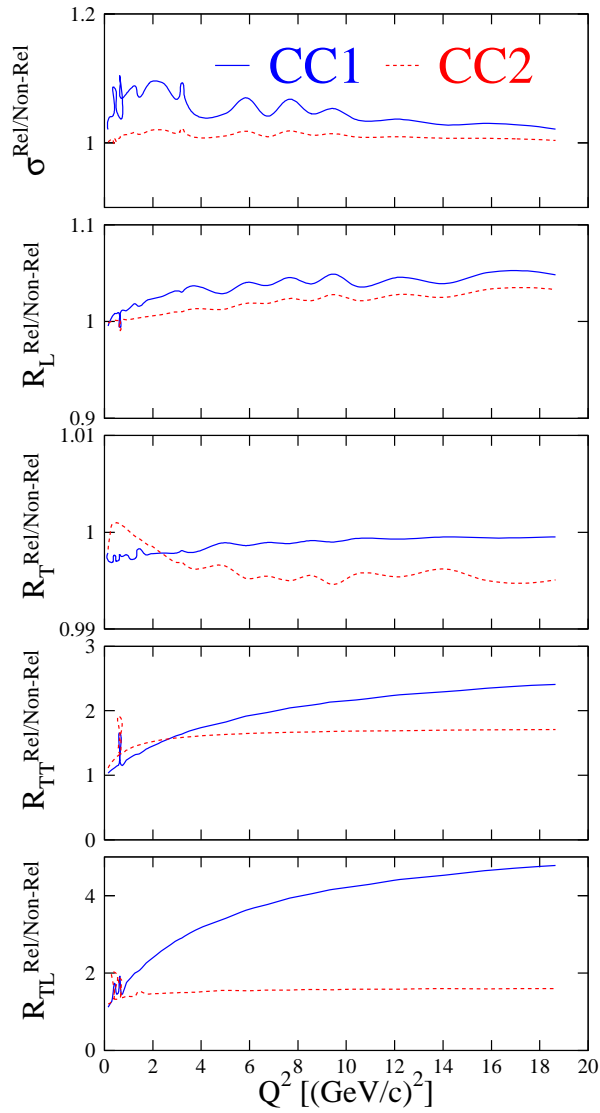


**Figure 8.2** The  $Q^2$  dependence of the sensitivity of the  $(e,e'p)$  structure functions to dynamical relativistic effects. The curves show for  $1p_{3/2}$  knockout from  $^{12}\text{C}$  the ratio of the fully relativistic results to the predictions when the coupling between the lower components has been omitted. These calculations were performed in the maximum of the  $1p_{3/2}$  momentum distribution ( $p_m \simeq 100 \text{ MeV}/c$ ). Calculations are performed for both the CC1 and CC2 current operator in the Glauber framework.

effects, in terms of our definition, introduces more absorption, resulting in higher spectroscopic factors. In contrast with other studies [45, 53, 90, 91] that have estimated the effect of relativity, we find an overall enhancement of the differential cross section due to coupling of the lower components in the bound and scattering wave function. This should be attributed to the fact that these other studies explicitly made a comparison of a non-relativistic Schrödinger approach with their fully relativistic models, while we estimate the effect of relativity by omitting the coupling term of the lower components in the fully relativistic expression of the transition matrixelement.

The genuine relativistic effect stemming from this coupling is larger in the longitudinal than in the transverse channel. It is noteworthy that in the cross section the impact of the “relativistic dynamical effects” never exceeds the 10 % level. This also applies to the longitudinal structure function  $R_L$ . In the transverse response  $R_T$  the magnitude of the effects is at the percent level. However, in this channel, the net effect of introducing relativity into the calculation is a reduction of the strength. If we turn our attention to the interference structure functions  $R_{TL}$  and  $R_{TT}$ , the relativistic effects grow in importance. Especially for the  $R_{TL}$  structure function the effects are large and extend to the largest values of  $Q^2$  considered here. This enhanced sensitivity of the  $R_{TL}$  response to relativistic effects, even when relatively low values of  $Q^2$  are probed, complies with the conclusions drawn in other studies [45, 90, 104, 105, 106]. The enhancement of the  $R_{TL}$  structure function after including the dynamical coupling between the lower components in the nucleon spinors, gives rise to an enhanced left-right asymmetry in quasi-perpendicular kinematics. This enhancement of the  $R_{TL}$  structure function makes that the relativistic predictions for the differential cross section are less symmetric than the nonrelativistic predictions.

We conclude the discussion of Fig. 8.2 with remarking that the enhanced sensitivity to relativistic effects when using the CC1 version of the off-shell electron-nucleon coupling (Eq. (4.2)), can be attributed to the momentum-dependent part of that operator. The contribution of this term in the matrixelement  $\langle k_f s_f | J_{cc1}^\mu | k_i s_i \rangle$  experiences severe reductions when neglecting the coupling between the lower components.

A quantity that can be relatively easy accessed experimentally, and, at the same time, depends heavily upon the  $R_{TL}$  structure function is the left-right asymmetry  $A_{LT}$  that was defined earlier in Eq. (6.12). The role played by the lower components in this dynamical enhancement of the left-right asymmetry can be further clarified by looking at the results of Fig. 8.3. In this figure, we plot the left-right asymmetry for  $1p_{3/2}$  knockout from  $^{12}\text{C}$ , for different  $Q^2$  and quasi-elastic conditions. Looking at the fully relativistic curves, we observe a gradual decrease of the asymmetry with increasing  $Q^2$ . At the same time, the relative contribution of the “non-relativistic” contribution to  $A_{LT}$  diminishes. This indicates that the asymmetry is almost exclusively generated by the coupling between the lower components as  $Q^2$  increases.

A quantity similar to the left-right asymmetry  $A_{LT}$  is the  $A_{LT'}$  observable

$$A_{LT'} = \frac{2v_{TL'}R_{TL'}}{v_L R_L + v_T R_T + v_{TL}R_{TL} + v_{TT}R_{TT}}, \quad (8.1)$$

and can be measured by taking the electron's helicity into account. At high energies the reaction process becomes independent of the electron's helicity and therefore it is expected that  $A_{LT'}$  will fall to zero if higher and higher energies are probed. In Fig. 8.4 we display  $A_{LT'}$  for a number of  $Q^2$  for scattering in a plane that is perpendicular to the electron scattering plane. This choice maximizes the contribution from the  $R_{TL'}$  structure function which has a  $\sin \phi$  dependence. Several observations emerge from Fig. 8.4. First, the asymmetry  $A_{LT'}$  decreases as  $Q^2$  increases. Second, we observe relativistic effects only at higher momenta, a feature that was already established in literature [45, 90, 91, 92, 103]. Third, in line with the left-right asymmetry  $A_{LT}$ , the nonrelativistic calculations predict much smaller asymmetries than the fully relativistic ones, indicating that the asymmetry is again mainly generated by this dynamical coupling of the lower components.

If one assumes equivalent central and spin-orbit potentials in a Schrödinger and a Dirac approach, another relativistic effect stems from the so-called Darwin term. Recalling the eikonal phase of Eq. (5.16)

$${}_iS(\vec{b}, z) = -{}_i\frac{M}{K} \int_{-\infty}^z dz' [V_c(\vec{b}, z') + V_{so}(\vec{b}, z')[\vec{\sigma} \cdot (\vec{b} \times \vec{K}) - {}_iKz']], \quad (8.2)$$

it is the impact of the last term in this expression on the cross section and structure functions that we want to measure. For that reason, we have performed calculations for the  $^{16}\text{O}(e, e'p)$  experiment of Ref. [15]. In Fig. 8.5 we present results for a fully relativistic eikonal model with Cooper potentials, once with and once without the Darwin term included. As a comparison, we have also plotted results where both the spin-orbit and Darwin term were set to zero. These results are also interesting to compare with Glauber calculations, which typically only incorporate a central scattering part. As expected, the effects of the entire spin-dependent term (i.e. including the Darwin term) on the relatively spin-insensitive response functions  $R_L$  and  $R_T$  is minimal. A slight reduction of the response functions is observed when spin-orbit and Darwin terms are taken into account. The effects on the interference structure functions  $R_{TL}$  and  $R_{TT}$ , on the other hand, are significant as far as the spin-orbit term is concerned. The net effect of the Darwin term is rather modest, and more pronounced in the  $1p_{1/2}$  knockout reaction than in the  $1p_{3/2}$  knockout reaction. In the  $1p_{1/2}$  knockout reaction, the exclusion of the Darwin term causes a modest enhancement of the interference structure functions, while omitting the spin-orbit part results in a rather large decrease of strength in the  $R_{TL}$  and  $R_{TT}$  response

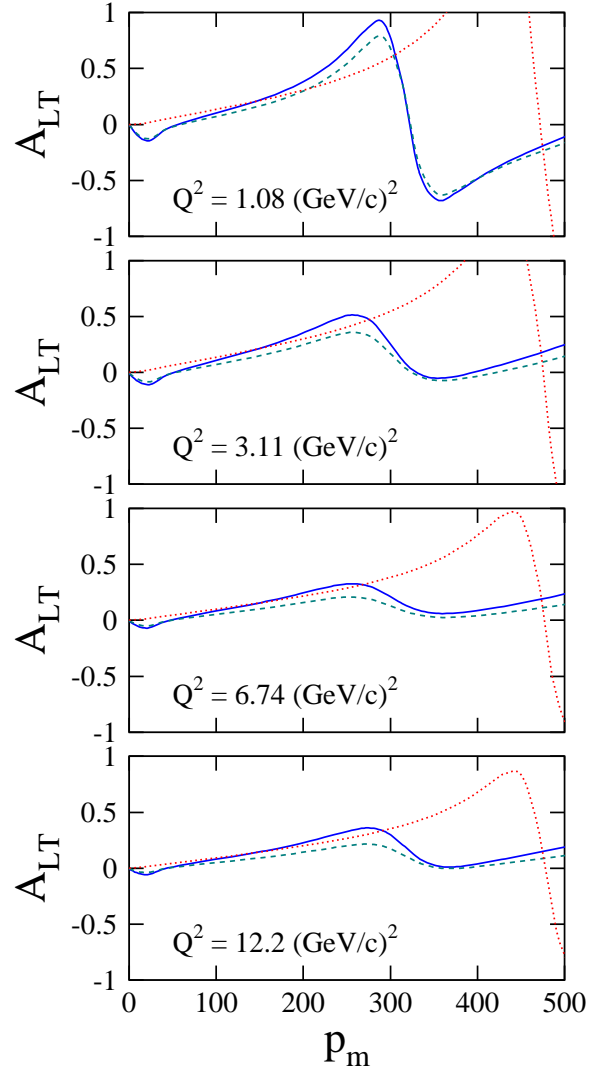


**Figure 8.3** The left-right asymmetry  $A_{LT}$  for  $1p_{3/2}$  knockout from  $^{12}\text{C}$  for different  $Q^2$ . The Glauber calculations were performed for quasielastic conditions and a fixed value of  $p_m = 100$  MeV/c. Results are shown for the full Glauber calculation (solid line), for a Glauber calculation where the coupling between the lower components has been set to zero (dashed line) and for RPWIA calculation (dotted line).

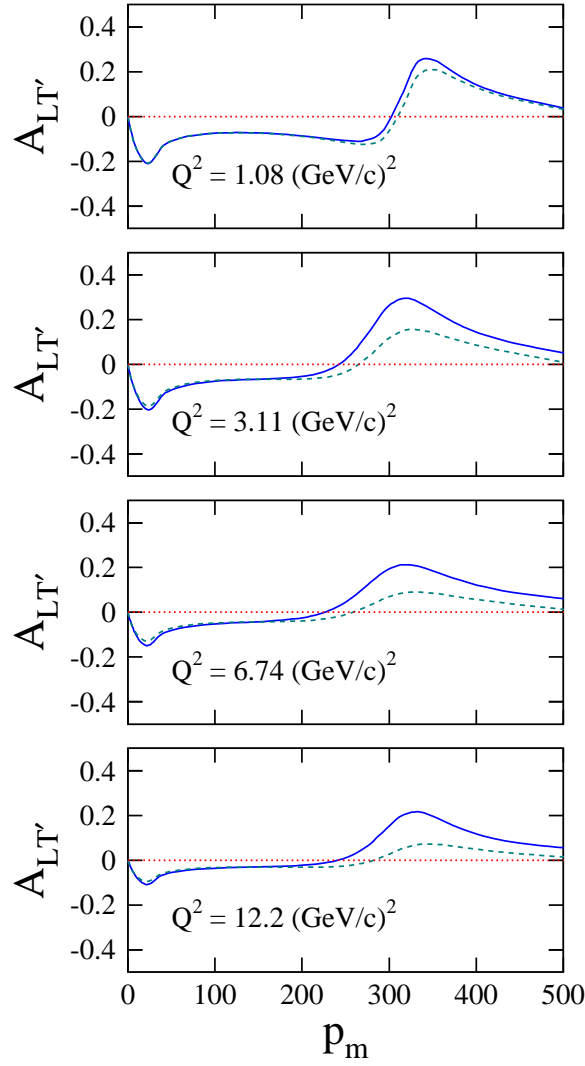


**Figure 8.4** The helicity asymmetry  $A_{LT'}$  for  $1p_{3/2}$  knockout from  $^{12}\text{C}$  for different  $Q^2$ . The calculations were performed under quasielastic conditions in the reaction plane that is perpendicular to the scattering plane (i.e.  $\phi = 90^\circ$ ). Shown are fully relativistic Glauber results (solid line), Glauber calculations in which the coupling of the lower components was set to zero (dashed line), and the plane wave results (dotted line).

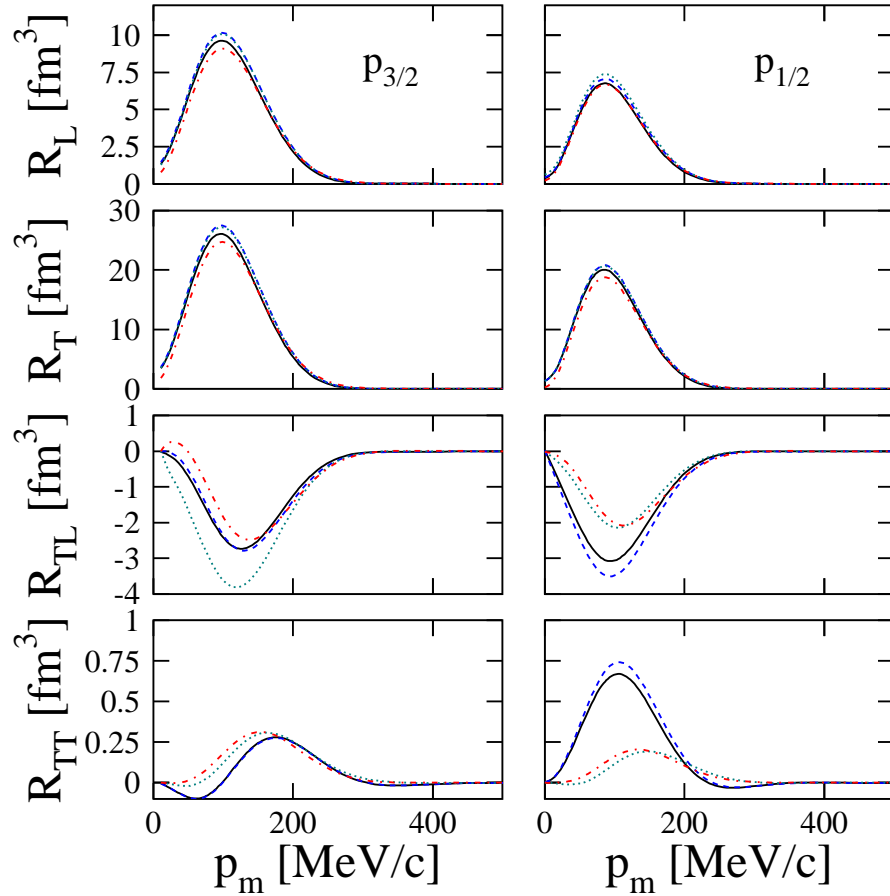


**Figure 8.5** The unpolarized structure functions for the  $^{16}\text{O}(e, e'p)$  reaction for  $\epsilon = 2.4$  GeV,  $q = 1$  GeV/c, and  $\omega = 0.439$  GeV. Shown are the results for the full eikonal calculation (solid line), the full eikonal calculation with the Darwin term neglected (dashed line), the full eikonal calculation with the spin-orbit and Darwin part turned off (dotted line) and the multiple-scattering Glauber calculations (dash-dotted line). The calculations made use of the CC2 operator, and are normalized for spectroscopic factors  $S_{1p} = 2j + 1$ .

functions. Major differences are observed for the spin-orbit partners  $1p_{1/2}$  and  $1p_{3/2}$ . The interference structure functions are thus highly sensitive to the spin-dependent terms in the optical potential. Furthermore, the spin-orbit term has the largest impact at low missing momenta, which concurs with other studies [86]. In Fig. 8.5, the Glauber curves closely follow the predictions of the optical potential calculations after turning off the spin dependent terms (with an exception for the  $R_{TL}$  response function for knockout from the  $1p_{3/2}$  level). This illustrates that if one would also include a spin-orbit scattering amplitude in the Glauber formalism, one would most certainly dismiss some of the discrepancies observed between the Glauber model and the eikonal model. This effect was already studied for the deuteron in Ref. [7].

In conclusion, we can say that the relativistic effects stemming from the Darwin term are rather modest, especially if they are compared to the dynamical effects resulting from the coupling between the lower components of the bound and final state.



---

## Chapter 9

# Nuclear Transparency

---

The issue of nucleon propagation through the nuclear medium has received much attention during the last few decades. For large enough energies, perturbative QCD predicts the so-called phenomenon of color transparency. The possible occurrence of this effect was predicted by Brodsky and Mueller in the early 1980s [107, 108]. In the context of exclusive  $A(e, e'p)$  reactions this phenomenon causes the struck nucleon to undergo minimal interactions with the surrounding nuclear environment, thereby making the nucleus more “transparent” for the emission of the proton.

In Sec. 9.1 we outline the theoretical assumptions which underly the color transparency (CT) phenomenon. These assumptions are actually predictions by different non-perturbative QCD-models which in themselves await experimental verification. The onset of CT in  $(e, e'p)$  processes can only be observed provided that realistic models for proton transparency can determine the baseline for standard final-state interactions. In Secs. 9.2 and 9.3, we present a brief overview of experimental results so far. As we will see, there remain a lot of unsolved or not so-well understood facets of this phenomenon. In Sec. 9.3 we present our calculations for the nuclear transparency in the  $^{12}\text{C}(e, e'p)$  reaction. These calculations cover quasielastic kinematics in a wide kinematic range [ $0.1 (\text{GeV}/c)^2 \leq Q^2 \leq 20 (\text{GeV}/c)^2$ ]. In comparison with other nuclear transparency calculations which are available in literature, our calculations are unfactorized and account for relativistic effects. In the  $Q^2 \leq 2 - 3 (\text{GeV}/c)^2$  regime, we will compare calculated transparencies obtained within the optical potential model (OMEA) and the Glauber (RMSGGA) approach.

### 9.1 Theoretical Background

For color transparency to occur in semi-exclusive  $(e, e'p)$  reactions, basically three requirements have to be fulfilled [2, 3, 4]

**Requirement 1 : Small objects are produced at high  $Q^2$  collisions.**

Consider a highly energetic virtual photon impinging upon a bound nucleon in the nucleus. On the basis of the qualitative features of the nucleon-nucleon cross sections at high energies (see Fig. 5.5) one would expect the struck proton to be scattered into the inelastic channels. However, as high momentum transfer is associated with small wavelengths, the virtual photon can probe the subnucleonic degrees of freedom. Suppose now that the incoming photon hits one of the confined color quarks. As the quark is now in a highly excited state, it will move very rapidly in some direction. According to the uncertainty principle, the excited quark which now has an energy surplus of  $\delta E \sim \omega$ , will decay by emitting gluons in a time  $\tau \sim 1/\omega$ . A single quark is colored, and colored objects are not allowed to exist freely according to the confinement principle. Hence, the struck quark will hadronize unless it is followed by its two companion quarks. In order now for these two quarks to be able to follow the escaping quark, they must have been close together initially. On average the radiated gluons must be absorbed by quarks which are a distance less than  $r = \tau \sim 1/\omega$  away. This means that the struck proton must have been in a small-sized fluctuation. Note that one has to make a distinction between the initially bound nucleon and the “object” which moves through the nucleus which should not really be looked upon as a nucleon.

QCD lattice calculations indicate that hadrons are bound states of strongly interacting quarks and gluons. The hadron can be described in terms of an infinite number of configurations, and different configurations are expected to have different sizes :

$$|N \rangle = |qqq \rangle + |qqq + \pi \rangle + \dots \quad (9.1)$$

For example, a configuration containing a  $\pi$  meson cloud will have a maximal radius due to the light mass of the pion. As in ordinary quantum mechanics, this system fluctuates between its different configurations. Consequently, images of a hadron taken at different times would reveal both small and large-sized configurations. One refers to this phenomenon as color fluctuations. The average time it takes to fluctuate between two configurations can be estimated on the basis of the uncertainty principle. As the time scale is inversely proportional to the energy (or mass) difference between the two configurations one can write that  $\tau \sim 1/(m - M)$ . As the mass differences are of the order of a few hundreds of MeV, the fluctuation time is very small, and of the order of 1 fm. Some hadronic models predict that these small, point-like configurations (PLC) could already be produced for momentum transfers as low as 1-2 GeV/c.

### **Requirement 2 : Small objects experience reduced interactions**

The second condition which has to be fulfilled for CT to exist, is that the “small object” interacts in an anomalously weak manner with the surrounding nuclear medium. This situation is somewhat comparable to the charge screening effect in QED where two neutral atoms interact with one another through their electric dipole moment. In QCD the electric charges are now the color charges, and the hadrons now play the role of charge neutral objects, i.e. color singlets. A small object will have a small color dipole moment, and will interact in a much weaker way than a normal sized singlet. This assumption arises naturally from a two-gluon exchange model between color singlets. As gluons carry color, single gluon exchange is forbidden. This model can be considered plausible as it proves the approximate constancy of the hadronic total cross sections, and also explains why the imaginary part of the forward scattering amplitude is much larger than the real part.

### **Requirement 3 : Small objects escape the nucleus before expanding**

Since the ejectile is not a stationary state of the QCD-Hamiltonian, it will undergo time evolution, which can only happen by increasing its size and restoring the soft quark-gluon fields. As it moves through the nucleus, the PLC expands and, if this expansion is rapid enough, it will become normal-sized before leaving the nucleus and will start interacting in a “normal” way with the surrounding nucleons, as shown in Fig. 9.1.

Suppose the hadron has a large laboratory momentum  $k$ , with  $v \sim c = 1$ . The energy difference between configurations of mass  $m$  and  $M$  becomes  $\sqrt{k^2 + M^2} - \sqrt{k^2 + m^2}$ . If  $k$  is very large, the energy denominator  $(M^2 - m^2)/2k$  can be small, and the time scale for fluctuation is long. The configuration of mass  $M$  can move for a long distance

$$l_c = \frac{2k}{M^2 - m^2}, \quad (9.2)$$

before decaying. Coherent, constructively interfering interactions occur between the excited configuration and the target material over this length  $l_c$ , the so-called coherence length. This length grows with increasing energy and can thus become greater than the nucleus’ radius. The time  $\tau$  it takes for a PLC to evolve into an object of normal hadronic size is then evidently given by  $\tau = 2k/(M^2 - m^2)$ . The bare mass  $M$  of the PLC is an undetermined parameter in estimating this expansion time. However, for sufficiently large energies,  $\tau$  will be long enough so that the object can leave the nucleus without any interactions. Different estimates based on quark models lead to values of  $\tau$  of 0.4 - 1.0 (E/GeV)fm. So with current values of  $E$  up to 5 GeV, expansion will occur and final-state interactions are not completely suppressed. It should however be possible to estimate this rate of expansion in the

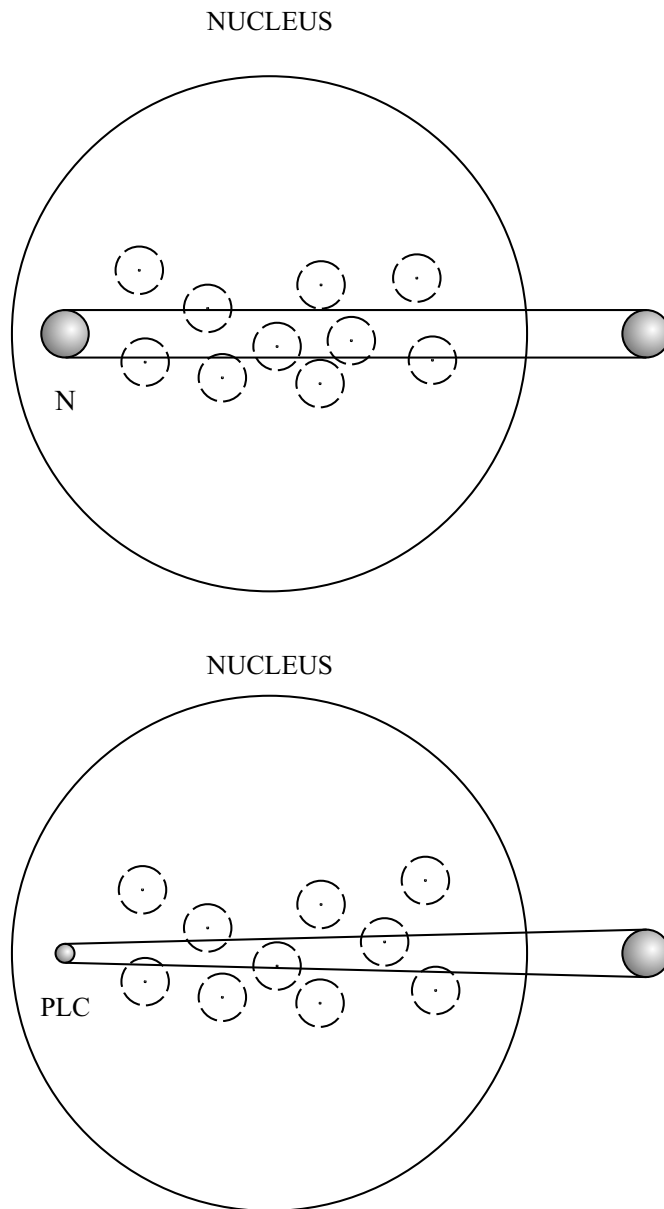


**Figure 9.1** Schematic representation of the interaction of a “normal-sized” nucleon (upper panel) and an expanding PLC (lower panel) with the surrounding nucleons.

few GeV energy range.

In brief, CT can only exist if one assumes that at high momentum transfer small color singlet objects (PLC's) are produced, which experience little interaction with the surrounding nucleons. This system expands and interacts as it moves through the nucleus.

To implement CT effects in the description of  $(e, e'p)$  processes, it is mandatory to adjust the interaction matrix elements. In the energy regime of interest here, the expansion distance, or coherence length, is still rather small. In an optical potential model one has that the imaginary part of the optical potential  $U_{opt}$  is roughly proportional to the total proton-nucleon cross section  $U_{opt} \simeq -i\sigma^{tot}\rho(r)$ , where  $\rho(r)$  is the nuclear density. Only the imaginary part of the optical potential is retained here. Indeed, at high energies the real part of the nucleon-nucleon forward scattering amplitude is small. Equivalently, from Eq. (5.38) it is clear that in a Glauber formalism, the magnitude of the final-state interactions is proportional to the total cross section. Since a point-like configuration cannot be treated as a nucleon, it becomes inaccurate to use the proton-nucleon cross sections as a measure for the interactions that the PLC is subject to in the medium. The simplest way to implement color transparency is to replace the free proton-nucleon cross section  $\sigma_{pN}^{tot}$  by a new quantity  $\sigma_{PLC}^{eff}$ , that describes the interaction of the PLC with the medium. This effective cross section should take into account both the suppression of interaction in the point where the PLC is produced and the restoration of soft final state interactions with the nucleons as it moves through the nuclear medium. The need to include this expansion was recognized by Farrar et al. [109], who argued that the square of the transverse size is approximately proportional to the distance travelled from the point where the PLC is formed. Thus, the cross section  $\sigma$  that appears in the optical potential, or, equivalently, in the Glauber profile function, is replaced by one that grows as the ejectile moves in the  $z$  direction [3, 4] :

$$\sigma_{PLC}^{eff} = \sigma_{pN}^{tot} \left\{ \left[ \frac{z}{l_c} + \frac{\langle n^2 k_T^2 \rangle}{Q^2} \left( 1 - \frac{z}{l_c} \right) \right] \theta(l_c - z) + \theta(z - l_c) \right\}. \quad (9.3)$$

Here,  $z$  is the distance moved by the expanding color singlet along the trajectory from its point of formation,  $n$  is the number of constituents in the proton (i.e.  $n = 3$ ), and  $k_T^2$  is the average transverse momentum of the proton's constituents [ $k_T^2 \simeq (0.35 \text{ GeV}/c)^2$ ]. The linear dependence of the cross section follows from analyses of perturbative Feynman diagrams. Moreover, it is commonly assumed that the size of the object's configuration decreases inversely proportional with  $Q^2$ . This assumption is legitimized by the fact that this reproduces the correct  $Q^2$  dependence of the transverse size of nucleons found in realistic models of the nucleon form factor. The coherence length  $l_c$  depends upon the squared mass difference of the initial PLC and

the final hadron. Obviously, its value is very important as it defines the scale at which the onset of CT effects occurs. Based on several constituent quark models this squared difference is usually bound in the range of  $0.7 \leq \delta M^2 \leq 1.1$  (GeV/c<sup>2</sup>)<sup>2</sup>. This lowest value of  $0.7$  (GeV/c<sup>2</sup>)<sup>2</sup> would allow to witness the effects of color transparency for energies as low as  $Q^2 \geq 5$  (GeV/c)<sup>2</sup>.

Unfortunately, the color transparency phenomenon is suppressed at intermediate  $Q^2$  by a QCD effect that is called the nuclear color screening effect. This effect causes the probability to create a color singlet in a bound nucleon to be smaller than in a free nucleon. Since the potential for the interaction of a bound nucleon in a small-size configuration with nearby nucleons is smaller than for a nucleon which resides in an “average” configuration, the creation of a PLC would lead to smaller binding energies. Energywise this is not a preferred configuration. Therefore, this mechanism is suppressed by a factor  $\delta(k)$  which modifies the momentum distribution. For sake of completeness we give the expression for  $\delta(k)$  as it was derived in Ref. [110] :

$$\delta k = \delta(Q_0^2 - Q^2) + \delta(Q^2 - Q_0^2) \left[ 1 + \left( 1 - \frac{Q_0^2}{Q^2} \right) \frac{\frac{k^2}{m_p} + 2\epsilon_A}{\delta E} \right]^{-2}. \quad (9.4)$$

An analysis of the <sup>2</sup>He(e,e') SLAC data in Ref. [110] indicate a value of  $Q_0^2 \sim 2$  (GeV/c)<sup>2</sup>. Its effect is illustrated in Fig. 9.2 that was taken from Ref. [4]. We conclude this section by remarking that other and more complicated procedures to describe the reduced interaction of the PLC with the surrounding nuclear medium have been developed. Because of its relative simplicity, the procedure of Eq. (9.3) is most widely used.

## 9.2 Review of Experimental Results

The first transparency experiment looking for CT effects was performed by Carroll et al. [111]. In this experiment large-angle  $pp$  elastic and quasielastic ( $p, 2p$ ) scattering cross sections were measured simultaneously in hydrogen and several nuclear targets (Li, C, Al, Cu, Pb) at incident proton momenta of 6, 10 and 12 GeV/c. The nuclear transparency was measured as the ratio of the obtained cross sections with the free  $pp$  cross section. These data showed a color transparency-like increase for  $Q^2 \sim 3 - 8$  (GeV/c)<sup>2</sup>, followed by a decrease for  $Q^2 \sim 8 - 11$  (GeV/c)<sup>2</sup>. This decrease occurs in a region where the free proton-nucleon cross section exhibits very little energy dependence. These results were interpreted by the so-called Landshoff process [112], a process which does not occur in  $A(e, e'p)$  reactions.

A few years ago, the A-dependence of the quasi-elastic  $A(e, e'p)$  reaction has been studied at SLAC with <sup>2</sup>H, C, Fe and Au nuclei as targets [98, 99]. In this experiment the nuclear transparencies were extracted at momentum transfers  $Q^2 = 1, 3, 5$  and  $6.8$  (GeV/c)<sup>2</sup>. Recalling the discussion of Sec. 9.1, one can expect to see the onset of CT in the highest  $Q^2$  part of the data.

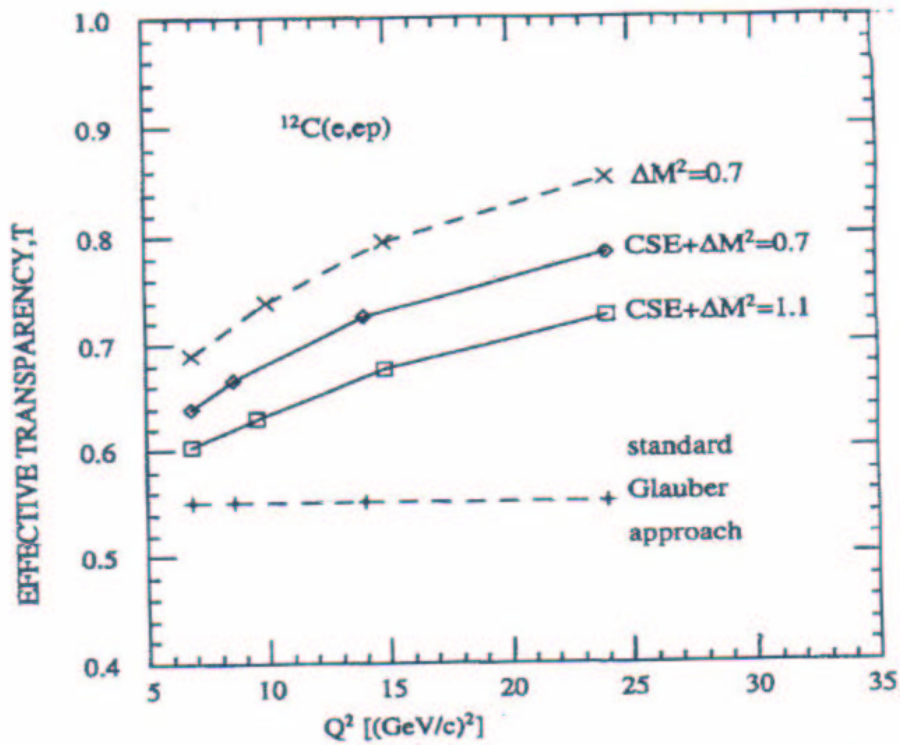


**Figure 9.2** Effective transparency as a function of  $Q_0^2$  for the  $^{12}\text{C}(e, e'p)$  reaction, calculated in a quantum diffusion model with different values of  $\delta M^2$ . The curves labeled CSE include the color screening effect of suppression of small-size configurations in bound nucleons. This picture was taken from Ref. [4].

In  $A(e, e'p)$  processes the nuclear transparency is determined as the ratio of the measured to the plane wave impulse approximation cross section. Hereby both the data and the PWIA results are integrated over that region of phase space where the IA approximation is established to be a valid approximation. One has

$$T_{exp} = \frac{\int_{\Delta^3k} d\vec{k} \int_{\Delta E} dE S_{exp}(\vec{k}, E)}{\int_{\Delta^3k} \int_{\Delta E} dE S_{PWIA}(\vec{k}, E)}, \quad (9.5)$$

where  $S_{exp(PWIA)}$  is the measured (plane wave) cross section divided by a kinematic factor and the off-shell elastic electron-proton scattering cross section  $\sigma_{cc1}^{ep}$  of Ref. [39]. For the SLAC experiment, the boundaries in the above integrals were fixed at  $-30 < E_m < 100$  MeV for the missing energy and  $0 < p_m < 250$  MeV/c for the missing momentum.

Studying the A-dependence of the experimental nuclear transparency is a very efficient tool to search for CT effects. Indeed, CT implies that the ejectile experiences a reduced attenuation through the presence of the other nucleons over a distance comparable to the nuclear radius. Evidently, this means that the onset of CT effects in heavier nuclei should be slower, and, hence, a change in the shape of the A-dependence with increasing  $Q^2$  could indicate the onset of CT. If one simply parametrizes this A-dependence as  $T(Q^2) = c(Q^2)A^{\alpha(Q^2)}$ , then complete CT would correspond to  $\alpha = 0$ , or, a vanishing dependence on the radius of the nucleus.

The results of such A-dependence measurements of the nuclear transparency are displayed in Figs. 9.3 and 9.4. Fig. 9.3 shows the measured transparency as a function of  $Q^2$ . The hypothesis of color transparency predicts an increase of T with increasing  $Q^2$ . The data in Fig. 9.3 show no evidence for this. Inspecting Fig. 9.4 which shows T as a function of A, a similar conclusion has to be drawn. Indeed, within experimental errors the  $\alpha$  values from the fit of the data to  $T = cA^\alpha$  are independent of  $Q^2$ , pointing towards the absence of CT effects. A calculation based on a classical attenuation model for protons propagating in the nucleus basically reproduces the A-dependence of the results.

It would be too simplistic to claim that CT has been ruled out by experiment. On the other hand, there are strong indications that color transparency is a small effect in the few-GeV regime. Another possibility is that CT effects are suppressed in this energy regime by a yet unknown QCD effect. One could also argue that the underlying model to determine the ‘‘normal’’ hadronic attenuation of the struck proton through the medium is too crude. For example, to our knowledge all Glauber calculations that have been done up to now adopt a factorized approach separating the photon-nucleus physics from the nuclear dynamics and ignore relativistic effects. In the preceding sections we have shown that the unfactorized Glauber model is fairly accurate in describing all major  $A(\vec{e}, e'\vec{p})$  observables. In what follows we will put our unfactorized and relativistic Glauber approach to test by comparing its calculated transparencies to the  $^{12}\text{C}$  data.

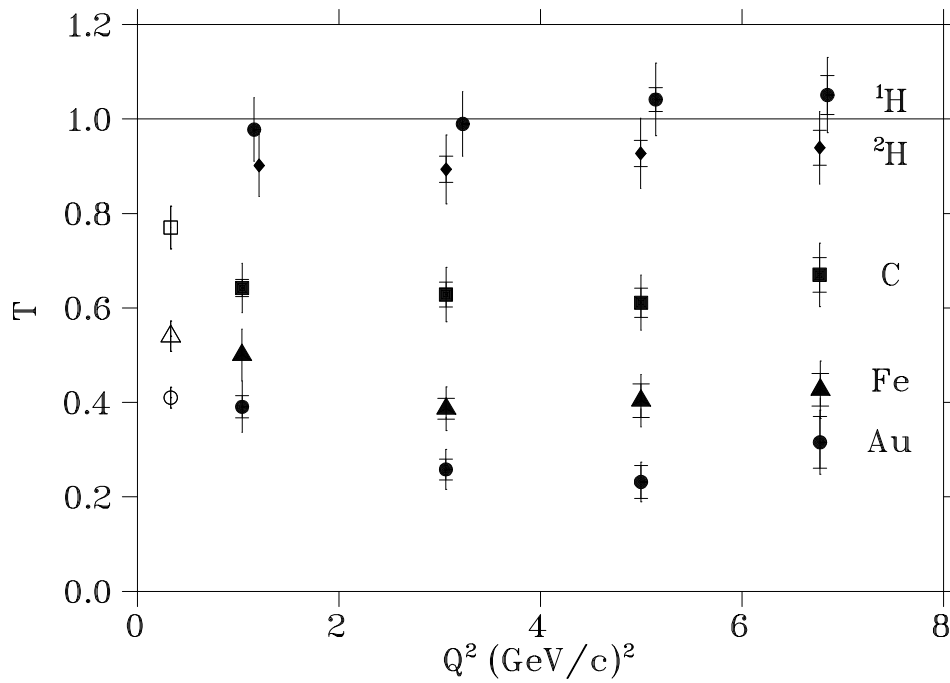


**Figure 9.3** Nuclear transparency for  $A(e, e'p)$  quasielastic scattering as a function of  $Q^2$ . The inner error bars are the systematic uncertainties, and the outer error bars are the statistical and systematic uncertainties added in quadrature. The open points at  $Q^2 = 0.33$   $(\text{GeV}/c)^2$  are from Refs. [113] and [114] for C, Ni and Ta targets. This figure was taken from Ref. [99].

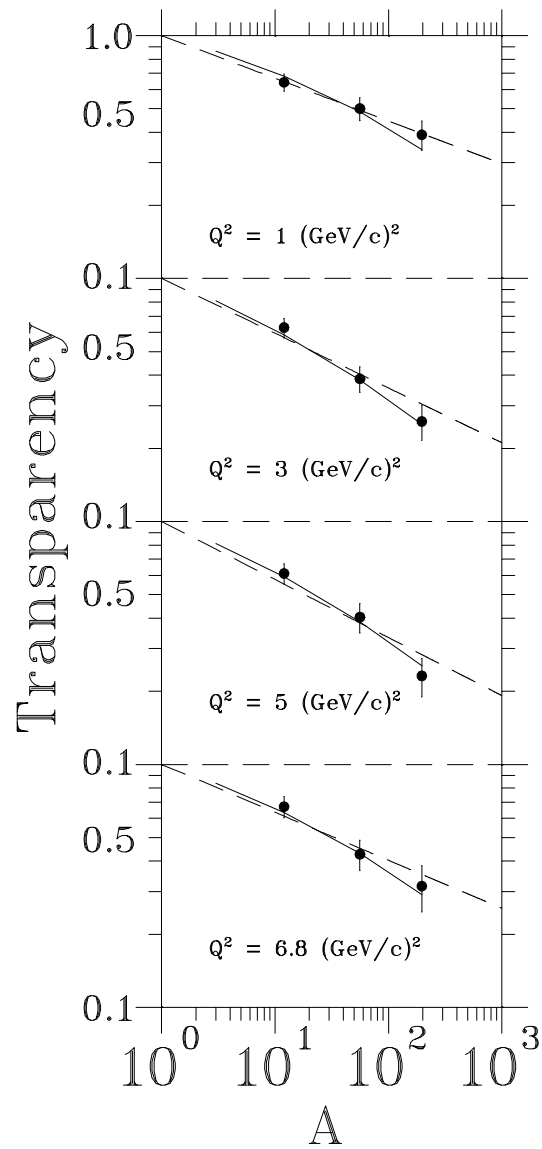


**Figure 9.4** Nuclear transparency (with total errors) as a function of  $A$  at various values of  $Q^2$ . The curves are fits to the C, Fe and Au data using the classical attenuation model discussed in Ref. [99] (solid line) and  $T(Q^2) = cA^{\alpha(Q^2)}$  (dashed line). This figure was taken from Ref. [99].

### 9.3 Nuclear Transparency Calculations

In this section we will study the nuclear transparency in the quasi-elastic  $^{12}\text{C}(e, e'p)$  reaction in a wide  $Q^2$  range of  $0.3 \leq Q^2 \leq 20$   $(\text{GeV}/c)^2$ . We will compare the results of our theoretical predictions with experimental results that were recently obtained at the Stanford Linear Accelerator (SLAC) [98, 99] and Jefferson Lab (JLAB) [115].

The results of our nuclear transparency calculations in  $^{12}\text{C}$  are contained in Fig. 9.5. We have performed calculations within the Glauber framework and the eikonal model with the optical potentials of Ref. [56]. We remind the reader that the optical potential model is only applicable up to values of  $T_p \sim 1$  GeV. As for the Glauber results, we have also performed calculations that included the effect of short-range correlations. Each of these calculations was done with the CC1 and CC2 current operator.

The measurements of the differential cross section in Refs. [98, 99, 115] were performed in a limited region of the available phase space, dictated by the requirement that quasi-elastic conditions are met. Analogously, we have constrained our calculations to the same portion of phase space. In general, the experimental results are reported in terms of the experimental transparency  $T_{exp}$ , defined as

$$T_{exp} = \frac{\int_{\Delta^3 k} d\vec{k} \int_{\Delta E} dE S_{exp}(\vec{k}, E)}{c_A \int_{\Delta^3 k} \int_{\Delta E} dE S_{PWIA}(\vec{k}, E)}. \quad (9.6)$$

The A-dependent factor  $c_A$  renormalizes the PWIA results to take corrections induced by SRC into account. This factor grows with increasing mass number A. For the  $^{12}\text{C}(e, e'p)$  a correction factor of  $0.901 \pm 0.024$  was adopted by the authors of Refs. [98, 99, 115]. As the implementation of SRC can be done in numerous ways, we have removed this factor from the data of Refs. [98, 99, 115], as in Eq. (9.5). These ‘‘corrected’’ data points are shown in Fig. 9.5. Although the JLAB data points suggest somewhat smaller nuclear transparencies than the SLAC data, they are consistent with each other.

In line with Eq. (9.5) we have calculated the theoretical nuclear transparency  $T_{theo}$ , according to

$$T_{theo} = \frac{\int_{\Delta^3 k} d\vec{k} \int_{\Delta E} dE S_{theo}(\vec{k}, E)}{\int_{\Delta^3 k} \int_{\Delta E} dE S_{PWIA}(\vec{k}, E)}. \quad (9.7)$$

From the results contained in Fig. 9.5 it is clear that in a particular scheme, the transparencies computed with the CC1 current operator converge to those obtained with the CC2 form of the electron-proton coupling. Accordingly, the theoretical transparencies are relatively free of ambiguities with respect to off-shell prescriptions in the  $Q^2 > 3 - 4$   $(\text{GeV}/c)^2$  range. For these high  $Q^2$  values the difference between the CC1 and CC2 predictions drop to percent levels. The oscillations in our theoretical curves at high  $Q^2$  reflect the energy dependencies in the pp and pn scattering data

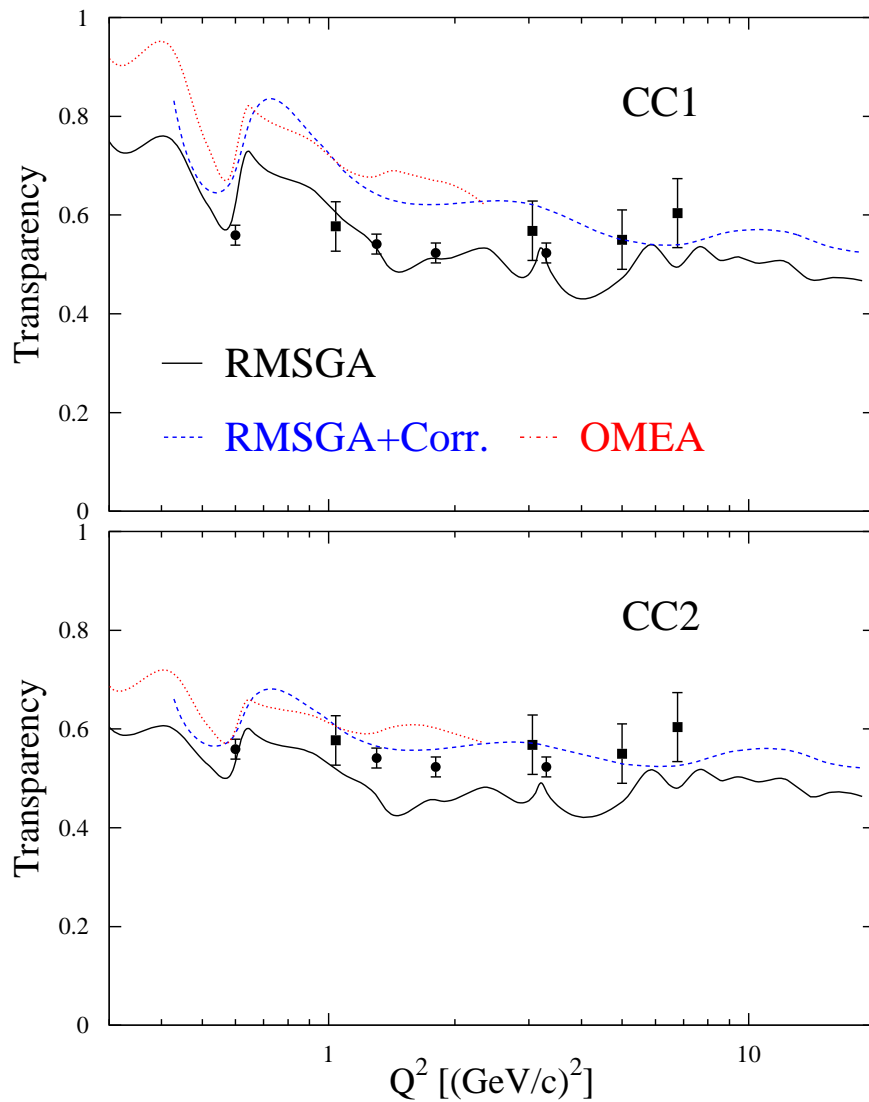


**Figure 9.5** Nuclear transparency for  $^{12}\text{C}(e, e'p)$  as a function of  $Q^2$ . The theoretical curves present calculations done within the Glauber framework and the eikonal model with optical potentials. Glauber calculations were done once including the effects of SRC, and once without. The calculations presented in the upper panel used the CC1 current operator, while the bottom panel used the CC2 current operator. The square data points are from SLAC [98, 99], and the round data points are from JLAB [115].

which serve as input parameters in the Glauber calculations. Most Glauber calculations which are available in literature adopt a “smooth” parametrization. In our calculations, we have chosen to insert the values as obtained by pN experiments at selected values of  $T_p$ . Referring to Fig. 5.10, we have estimated the effect induced by the experimental uncertainties of the pN scattering data on the nuclear transparency to be of the order of 5 %.

If we examine the standard RMSGA results that have not included the effects of SRC, we can infer from Fig. 9.5 that the calculations using the CC1 current operator reproduce the experimental data at lower  $Q^2$  rather well. At higher  $Q^2$  [ $Q^2 \geq 3 - 4$  (GeV/c)<sup>2</sup>], where the differences caused by the adoption of the CC1 or CC2 current operator are negligible, our Glauber predictions undershoot the observed experimental transparencies by about 10 - 15 %.

This deficiency, which is more pronounced for the calculations using the CC2 current operator, can be cured by the inclusion of short-range correlations. The effect of short-range correlations on transparencies has been studied extensively in literature [8, 72, 77, 76, 116, 117, 118, 119], and effects of the order of 10 % have been reported. We have adopted the central correlation function of Gearheart and Dickhoff [78, 79] along the lines of Eq. (5.53). As can be seen from Fig. 9.5 the effects of SRC increase the calculated transparencies by about 10 %. It is interesting to note that this overall enhancement of the nuclear transparency due to the effects of SRC is independent of  $Q^2$ ; the correlated Glauber calculations follow a trend very similar to the uncorrelated Glauber results. This can be explained by the fact that the adopted short-range correlation function does not have any  $Q^2$  dependence, and, hence, one can expect a relative enhancement of the nuclear transparency which is independent of  $Q^2$ . That is also the reason why the factor  $c_A$  in Eq. (9.6) is a function of the mass number  $A$  only. This also means that the effects caused by pure color transparency can still be disentangled from the effects stemming from short-range correlations. It was already discussed in Sec. 9.2 that CT effects can be revealed through their  $Q^2$  dependence. Inspecting Fig. 9.5 we observe that the correlated RMSGA results for both the CC1 and CC2 current operator, are now able to describe the high  $Q^2$  data. Furthermore, the correlated RMSGA calculations using the CC2 current operator provides us with a fair description of all the transparency data, both at low and high  $Q^2$ .

When we restrict ourselves to the lower  $Q^2$  regime, we can also compare the results of an optical potential model with the experimental results and the corresponding Glauber calculations. It is very clear from Fig. 9.5 that the OMEA results exhibit a behaviour very similar to the correlated Glauber results. This might come as a surprise since these models handle the final state interactions in a rather different way. The good agreement between the OMEA and the correlated RMSGA results is also a very interesting result in the sense that this demonstrates that the gap between the low  $Q^2$  regime, described in terms of a potential model, and the higher  $Q^2$  regime, described in terms of a multiple-scattering Glauber framework,

can actually be bridged in a satisfactory manner. We consider this an important finding. In what follows, it will be shown that this smooth transition from the low to the high  $Q^2$  regime has its consequences for the  $Q^2$  evolution of the spectroscopic factors in  $^{12}\text{C}$ .

The transparency results of Fig. 9.5 can be placed in a totally different context if we make the connection between the obtained nuclear transparencies and the summed spectroscopic strength of the independent-particle levels in  $^{12}\text{C}$ . In what follows we will examine this relationship more closely and demonstrate how a summed spectroscopic factor  $S_{12C}$  for the  $^{12}\text{C}$  nucleus can be extracted from the results presented in Fig. 9.5. With the term ‘‘summed’’ we refer to the fact that the spectroscopic factors  $S_{1s}$  and  $S_{1p}$  of the 1s and 1p levels in  $^{12}\text{C}$ , respectively, can not be extracted separately from the nuclear transparency results. In fact, one averaged spectroscopic factor  $S_{12C}$ , related to the total number of IPM protons, for the entire  $^{12}\text{C}$  nucleus will be determined according to

$$S_{12C} = \frac{2S_{1s} + 4S_{1p}}{6} . \quad (9.8)$$

We remind the reader that our spectroscopic factors are normalized to unity for each individual level characterised by an angular momentum  $j$  and principal quantum number  $n$ . Consequently, the summed spectroscopic factor  $S_{12C}$  of Eq. (9.8) is also normalized to unity.

In the calculations presented in Fig. 9.5 we have assumed a full occupancy of the proton levels. In other words, we have assumed that the spectroscopic factors equal 1, for both the 1s and 1p nuclear levels. The theoretical transparencies of Fig. 9.5 are the results of the following ratio

$$T_{theo} = \frac{S_{1p}\sigma_{1p}^{theo} + S_{1s}\sigma_{1s}^{theo}}{\sigma_{1p}^{PWIA} + \sigma_{1s}^{PWIA}} , \quad (9.9)$$

where  $S_{1p} = S_{1s} = 1$ , and where  $\sigma^{theo(PWIA)}$  is a shorthand notation for

$$\int_{\Delta^3k} d\vec{k} \int_{\Delta E} dE S_{theo(PWIA)}(\vec{k}, E) , \quad (9.10)$$

as in Eq. (9.6). Analogously, we have that the experimental transparency  $T_{exp}$  is given by

$$T_{exp} = \frac{\sigma_{1p}^{exp} + \sigma_{1s}^{exp}}{\sigma_{1p}^{PWIA} + \sigma_{1s}^{PWIA}} . \quad (9.11)$$

In order to make an accurate comparison of the theoretical transparencies and the experimental transparencies possible, we should insert the correct values for the spectroscopic factors  $S_{1s}$  and  $S_{1p}$  in Eq. (9.9). In Ref. [120] an analysis of the world’s

$^{12}\text{C}(e, e'p)$  data was performed in order to extract the correct values for the 1s and 1p spectroscopic factors from experiment. It was shown there that such an extraction of the spectroscopic factors at low  $Q^2$  [ $Q^2 < 0.6$  (GeV/c) $^2$ ] lead to a summed (average) spectroscopic factor  $S_{12C} = 0.575 \pm 0.02$  for  $^{12}\text{C}$ . These calculations were performed with an optical potential model to treat the final state interactions. On the other hand, the authors of Ref. [120] also performed Glauber calculations in the higher  $Q^2$  range [ $Q^2 > 0.8$  (GeV/c) $^2$ ] with the result that they found a summed spectroscopic factor of  $0.84 \pm 0.03$  at  $Q^2 = 1.08$  (GeV/c) $^2$  and slightly increasing values with increasing energy. The results of this analysis are shown in Fig. 9.6. We note that the authors of Ref. [120] adopt the convention in which the spectroscopic factor for a particular angular level is normalized according to the occupation number in the independent-particle model (i.e. 2 and 4 for the 1s and 1p proton levels in  $^{12}\text{C}$ , respectively). It is evident from the results for the spectroscopic factors in  $^{12}\text{C}$  that the calculated transparencies will differ enormously from each other depending on which values for the spectroscopic factors are adopted. When using the high  $Q^2$  spectroscopic factors of Fig. 9.6 to calculate the nuclear transparencies in the  $^{12}\text{C}(e, e'p)$  reaction, the authors found values  $T_{12C} \sim 0.5 - 0.6$  in the  $Q^2$  range between 1 and 8 (GeV/c) $^2$ . On the other hand, when using the low  $Q^2$  spectroscopic factors, transparencies  $T_{12C} \sim 0.8 - 0.9$  were found.

As already pointed out above, one can also perform the inverse procedure, where one combines the experimental transparency and the theoretical transparency to obtain an average spectroscopic factor  $S_{12C}$ . If the theoretically calculated transparency is scaled with the correct averaged spectroscopic factor, it should equal the experimentally found transparency. In other words the summed or average spectroscopic factor is simply found by considering the ratio  $T_{exp}/T_{theo}$ . This simple relationship gives the results of Fig. 9.5 a whole new dimension. For one, this means that we should only consider the calculations that overshoot the data points as realistic. The uncorrelated Glauber calculation using the CC2 current operator for example, largely undershoots the data points ( $T_{theo} < T_{exp}$ ), assuming a spectroscopic factor larger than unity. Second, the closer the theoretical curves are to the experimental data points, the higher the average spectroscopic factor. Complete agreement with the experimental results would assume a full occupancy of the nuclear shell levels.

In Fig. 9.5 the correlated RMSGA calculations predict an average spectroscopic factor that approaches unity in the  $Q^2 > 0.6$  (GeV/c) $^2$  regime. This observation concurs with the findings of Fig. 9.6. These spectroscopic factors are large compared to the ones typically found in low  $Q^2$  analysis. From Fig. 9.5 we can also infer a rather modest  $Q^2$  dependent rise of the spectroscopic factors in the correlated RMSGA calculations using the CC1 operator. This also concurs with the findings of Ref. [120], as can be seen from Fig. 9.6. For the calculations using the CC2 current operator, there's no real indication for a  $Q^2$  dependence of the spectroscopic strength, when experimental error margins are kept in mind. However, the most striking feature of Fig. 9.6 is the abrupt rise of the spectroscopic strength when going from the low

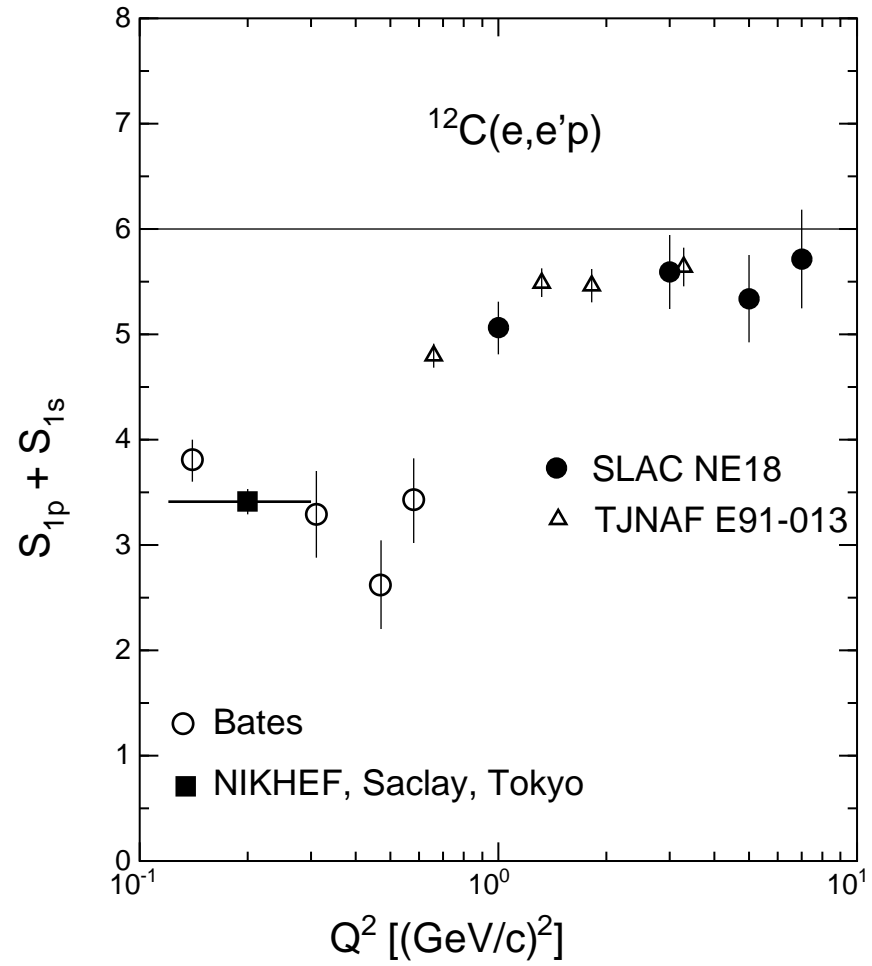


**Figure 9.6**  $Q^2$  dependence of the summed spectroscopic strength  $S_{1p} + S_{1s}$  for 1p and 1s knockout in the reaction  $^{12}\text{C}(e, e'p)$  up to  $E_m = 80$  MeV. This picture was taken from Ref. [120].

$Q^2$  regime to the higher  $Q^2$ . This rise is a well established fact and is caused by the quenching of the single-particle strength at low  $Q^2$ . Consequently, the rise of the spectroscopic factor from low to high  $Q^2$  is often referred to as single-particle strength restoration. Our results also point towards this strength restoration, but this rise of the spectroscopic factor in Fig. 9.6 happens rather abruptly around values of  $Q^2 \sim 0.6$  (GeV/c)<sup>2</sup>. A number of reasons are cited in Ref. [120] to account for this gap. First, and most apparent, is the usage of two entirely different models to analyze the low and the high  $Q^2$  data. As already mentioned the authors of Ref. [120] used an optical potential method to describe the <sup>12</sup>C( $e, e'p$ ) data at low  $Q^2$ , while a Glauber approach was adopted to account for the higher  $Q^2$  data. Our results of Fig. 9.5 however, convincingly demonstrate that calculations adopting an optical potential method at low  $Q^2$  are not necessarily inconsistent with Glauber calculations at higher  $Q^2$ , as can be deduced from Table 6.1. In the intermediate regime [ $0.5 < Q^2 < 1$  (GeV/c)<sup>2</sup>], where the OMEA calculations and the correlated RMSGA curves overlap, similar spectroscopic factors are predicted. Even if we were to exclude the effects stemming from SRC, the net effect on the spectroscopic factor would still be much smaller than is the case in Fig. 9.6. The good agreement in describing  $A(e, e'p)$  observables between the eikonal method with optical potentials and the multiple-scattering Glauber approximation was already extensively discussed in Sec. 6. Another reason that was cited as a possible origin for the observed discrepancy in Fig. 9.6 is the usage of different current operators. From Fig. 9.5 we can estimate this effect to be no larger than 10 % around  $Q^2 \sim 0.6$  (GeV/c)<sup>2</sup>. Also, we have shown in Sec. 8 that relativistic effects never exceed the 10 % level in the calculation of the differential cross section. One other possible explanation for the observed gap around  $Q^2 \sim 0.6$  (GeV/c)<sup>2</sup> is the contribution of two-body currents which are of more importance at low  $Q^2$  than they are at large  $Q^2$ . Many studies into the role of meson exchange and intermediate delta excitations in ( $e, e'p$ ) reactions have been carried out in the past [104, 121, 122], and it appears that the observed discrepancy can also not be (entirely) explained by two-body contributions. In fact, in Ref. [123] it is shown that the uncertainty on the extracted spectroscopic factors induced by mechanisms that fall beyond the impulse approximation is of the order of 5 - 10 %. The combined effect of two-body currents and ground-state correlations on the spectroscopic factors in <sup>16</sup>O is depicted in Fig. 9.7.

As suggested by the authors of Ref. [120], a consistent analysis of all <sup>12</sup>C( $e, e'p$ ) data between  $0.1 \leq Q^2 \leq 10$  (GeV/c)<sup>2</sup> could much improve insight into this matter. A consistent treatment would at least allow to separate genuine physical effects (contributions from meson exchange etc.) from model-dependent uncertainties (current operator, construction of final state etc.). Such an analysis should preferably be carried out in a framework that is able to describe both the low and high  $Q^2$  data without any inconsistencies in some intermediate-energy range. We feel that our model presented here, is an initial step in this direction.

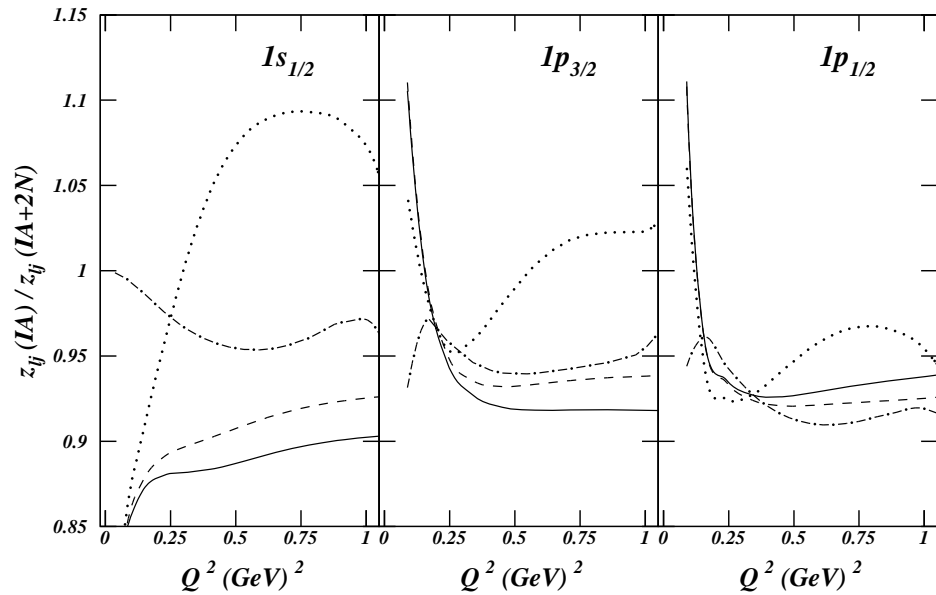


**Figure 9.7** The predicted sensitivity of the extracted spectroscopic factors to effects beyond the impulse approximation in the  $^{16}\text{O}(e, e'p)$  reaction. Parallel kinematics ( $\vec{k}_f \parallel \vec{q}$ ) and quasi-elastic conditions were imposed. The dashed line includes only central correlations, whereas the solid curve also includes tensor correlations. The dot-dashed calculation accounts only for meson exchange currents, whereas the dotted line includes meson and  $\Delta$ -isobar exchange currents, central and tensor correlations. This picture was taken from [123].

---

## Chapter 10

# Conclusion and Outlook

---

In this work we have outlined a *fully relativistic eikonal framework for modelling semi-exclusive  $A(e, e'p)$  reactions from spherical nuclei at intermediate and high four-momentum transfers  $Q^2$* . We have carried out a wide range of  $^{12}\text{C}(e, e'p)$  and  $^{16}\text{O}(e, e'p)$  calculations for a variety of kinematical conditions, thereby covering four-momentum transfers in the range  $0.1 \leq Q^2 \leq 20$  (GeV/c)<sup>2</sup>. Our model has proven to be a very *flexible framework* as it can be used in conjunction with relativistic optical potentials or within a Glauber multiple-scattering approach, which are two substantially different techniques to deal with final state interactions. To our knowledge all Glauber calculations reported in literature are performed within a non-relativistic and factorized scheme. Our approach can accommodate *dynamical relativity*, and all calculations were performed within a fully *unfactorized model*. This means that in our theoretical considerations we do not formally separate the proton-nucleus interaction from the nuclear dynamics.

In addition to the Glauber and optical potential approach we developed a consistent eikonal model (CEA) in which the bound and scattering states were derived from the same Dirac equation. Our results illustrate that the validity of the CEA is confined to proton emission in a cone with a relatively small opening angle about the direction of the virtual photon's momentum. At first sight, this observation put serious constraints on the applicability of the Glauber method, that is based on the eikonal approximation, for modelling the final state interactions in high-energy  $(e, e'p)$  reactions from nuclei.

However, although this consistent treatment minimizes the effects of spurious states, it can only take elastic contributions into account. It turned out that the implementation of inelastic contributions in the exit channels is needed to fully appreciate the limits of the Glauber model. To that purpose we have extended the eikonal formalism to include optical (complex) potentials that are constructed by global fits to the available nucleon-nucleus data. This method of dealing with final state interactions has shown to extend the applicability of the eikonal method far

beyond the limits which were observed in the consistent approach (CEA). In fact, we have found *no evidence that the applicability of the optical potential model in the eikonal approximation (OMEA) is restricted to a certain angular range.*

At higher  $Q^2$  [ $Q^2 > 1$  (GeV/c) $^2$ ] nucleon-nucleus scattering becomes increasingly diffractive, and descriptions of the reaction dynamics that rely on a potential approach for the ejectile can no longer be justified. For that reason we have also introduced a relativistic generalization of the Glauber approximation (RMSGGA). In such an approach the final state interactions in the nuclear medium are calculated from pp and pn scattering data. The question arises whether the transition between the low-energy regime, where optical potentials are used to calculate the scattering states, and the high-energy regime, where the Glauber method is adopted, is smooth.

To address this question, we have studied a large number of observables for the  $^{12}\text{C}(e, e'p)$  and  $^{16}\text{O}(e, e'p)$  reactions, and compared them with experimental results. Although both methods treat final state interactions in a rather different manner, *it was shown that they produce comparable results for the differential cross sections, structure functions and polarization observables.* We consider the fact that both methods produce *similar spectroscopic strengths* one of the major findings of this work. In this comparison, special attention was paid to the  $R_{TL}$  structure function. It has been extensively discussed in literature that the contribution stemming from the interference  $R_{TL}$  structure function is very sensitive to slight changes in the theoretical modelling of the reaction process, including the construction of the scattering wave function. We have shown that the largest differences between the optical model approach and the Glauber approach are indeed observed in the  $R_{TL}$  structure function. The left-right asymmetry  $A_{LT}$  that is heavily influenced by the  $R_{TL}$  structure function, proved to be a very efficient tool to express these differences. However, although both methods exhibit a very different  $p_m$  dependence for large missing momenta, they both reproduce the experimental trend, thereby illustrating *the necessity of including final state interactions at high missing momenta.*

A major concern in any relativistic approach are the uncertainties that arise from the choice of the electromagnetic electron-proton coupling. We have quantified the effects of the ambiguities on the observables by comparing results obtained with a number of current operators and methods to restore current conservation. In line with other investigations we have found that *the off-shell ambiguities grow with increasing missing momenta.* Further, it was demonstrated that a modification of the longitudinal component of the vector current according to  $J_z \rightarrow (\omega/q)J_0$ , which restores current conservation, produces the smallest off-shell ambiguities in the calculated results. Also, the current operator CC2 was put forward as the most favorable choice for the electron-proton coupling as calculations employing this operator proved to be rather insensitive to the chosen gauge restoration scheme.

A key issue in the considerations of off-shell ambiguities was the  $Q^2$  dependence of the induced uncertainties on the reaction observables. It is often claimed that

with increasing  $Q^2$  the uncertainties related to these ambiguities drop, making the impulse approximation increasingly accurate. In an attempt to verify this statement we have performed calculations in a wide  $Q^2$  range up to  $20 \text{ (GeV/c)}^2$ . It was not only found that the calculations using the substitution  $J_0 \rightarrow (q/\omega)J_z$  converged to those using the substitution  $J_z \rightarrow (\omega/q)J_0$ , but that the predictions with different current operators in one scheme also converged to each other with increasing energy transfer. Speaking in terms of cross sections, the uncertainties introduced by off-shell effects drop to percent levels for  $Q^2 \sim 3 - 4 \text{ (GeV/c)}^2$ . *It appears thus as if off-shell ambiguities are of far less concern at higher  $Q^2$  than they used to be in the  $Q^2 \leq 1 \text{ (GeV/c)}^2$  region, where most of the data have been accumulated up to now.* It was also found that the *interference structure functions  $R_{TT}$  and  $R_{TL}$  are subject to off-shell ambiguities that are extending to the highest four-momentum transfers* considered here. Note however that these effects also decrease with increasing energies, albeit in a much slower manner. This feature was explained by the large weight of the negative energy states in these structure functions.

Our theoretical model also permits to assess the impact of the relativistic effects over a wide energy range. Non-relativistic models for the electron-nucleus coupling typically miss the coupling between the lower components in the bound and scattering states. We have interpreted the effect of this coupling as a measure for genuine relativistic effects. *The impact of the lower components on the  $A(e, e'p)$  observables was observed to be significant over the whole  $Q^2$  range studied.* As for the cross section it was found that the impact of the coupling amongst the lower components first increases, and then tends to converge to zero when higher values of the energy transfer are reached. It is noteworthy that for the differential cross section the effect of this genuine relativistic mechanism never exceeds the 10 % level. *The enhanced sensitivity of the  $R_{TL}$  structure function to relativistic effects complies with other studies.* This enhancement leads the left-right asymmetry  $A_{LT}$  to be almost entirely governed by the coupling amongst the lower components, making this observable very useful to study the effects of genuine relativistic origin.

We have also calculated nuclear transparencies in our relativistic model. *We have not found any evidence for the onset of color transparency in the  $0.1 \leq Q^2 \leq 20 \text{ (GeV/c)}^2$  region.* It also became clear that an accurate description of the nuclear transparency at higher  $Q^2$  requires the inclusion of short-range correlations effects (SRC), as they prove to significantly enhance the  $(e, e'p)$  cross section, and, evidently, the nuclear transparency. Although the inclusion of SRC causes the nuclear transparency to be overall enhanced with some 10 %, still no  $Q^2$  dependent increase of the nuclear transparency with increasing momentum transfers is observed. The results for the nuclear transparency in  $^{12}\text{C}$  were also linked with the spectroscopic strength of the 1s and 1p levels in  $^{12}\text{C}$ . We have found that the summed *spectroscopic strength is almost  $Q^2$  independent* in the  $Q^2 > 1 \text{ (GeV/c)}^2$  range. Further, we have shown that the usage of a potential model for the description of  $A(e, e'p)$  transparencies at low  $Q^2$  is reasonably consistent with the high  $Q^2$  results which can

only be computed in a Glauber framework.

To conclude we would also like to propose some points of interest towards the future that might contribute to a better understanding of  $A(e, e'p)$  nuclear reactions, and, in particular, the transparency phenomenon

- *Extension of the eikonal/Glauber method* : higher order terms to increase the accuracy of the transversal momentum distribution, proper inclusion of spin-orbit, spin-spin, non-central corrections to the adopted potentials and scattering amplitudes, multiple-scattering extension of the optical eikonal method through the use of realistic nucleon-nucleon interaction potentials
- *Effect of short-range correlations at high  $Q^2$*  : particularly useful in this context are the two-nucleon knockout experiments and the corresponding polarization observables to gain some insight into the role of the strong central and tensor components of these correlations [124, 125, 126, 127]
- *Inclusion of recent experimental results on nucleon form factors* : in this work we have performed all calculations with the standard dipole form for the electromagnetic form factors. Since the reaction strength is heavily influenced by the elastic nucleon form factors, one should make use of the available experimental results and QCD-based predictions for these form factors
- *Hybrid models* : at high  $Q^2$  the incoming foton is able to probe the quark degrees of freedom in the struck nucleon, and a correct combination of QCD modelling and nuclear reaction theory might result in a more accurate description of the physics governing the  $A(e, e'p)$  reaction
- *Usage of other reaction frames* : standard nuclear calculations are performed within the laboratory or center-of-mass frame. It might be more efficient to consider another framework, as is done for example in Light Cone theory, where some of the properties inherent to high-energy reactions are already incorporated in the formalism

# Bibliography

---

- [1] V. Pandharipande, I. Sick, and P. deWitt Huberts, *Rev. Mod. Phys.* **69**, 981 (1997).
- [2] L. Frankfurt and M. Strikman, *Phys. Rep.* **76**, 215 (1981).
- [3] L. Frankfurt and M. Strikman, *Prog. Part. Nucl. Phys.* **27**, 135 (1991).
- [4] L. Frankfurt, G. Miller, and M. Strikman, *Annu. Rev. Nucl. Part. Sci.* **45**, 501 (1994).
- [5] R. Glauber and G. Matthiae, *Nucl. Phys. B* **21**, 135 (1970).
- [6] G. Alkhozov, S. Belostotsky, and A. Voroboyov, *Phys. Rep.* **42**, 89 (1978).
- [7] S. Jeschonnek and T. Donnelly, *Phys. Rev. C* **59**, 2676 (1999).
- [8] L. Frankfurt, E. Moniz, M. Sargsyan, and M. Strikman, *Phys. Rev. C* **51**, 3435 (1995).
- [9] O. Benhar, S. Fantoni, N. Nikolaev, J. Speth, A. Usmani, and B. Zakharov, *Z. Phys. A* **355**, 267 (1996).
- [10] N. Nikolaev, A. Szcurek, J. Speth, J. Wambach, B. Zakharov, and V. Zoller, *Nucl. Phys. A* **582**, 665 (1995).
- [11] C. Ciofi degli Atti and D. Treleani, *Phys. Rev. C* **60**, 024602 (1999).
- [12] A. Bianconi and M. Radici, *Phys. Lett. B* **363**, 24 (1995).
- [13] A. Rinat and M. Taragin, *Nucl. Phys. A* **623**, 519 (1997).
- [14] A. Kohama, K. Yazaki, and R. Seki, *Nucl. Phys. A* **662**, 175 (2000).
- [15] J. Gao et al., *Phys. Rev. Lett.* **84**, 3265 (2000).
- [16] C. Horowitz and B. Serot, *Nucl. Phys. A* **368**, 503 (1981).
- [17] Y. Yin, D. Onley, and L. Wright, *Phys. Rev. C* **45**, 1311 (1992).
- [18] J. Udias, P. Sarriguren, E. Moya de Guerra, E. Garrido, and J. Caballero, *Phys. Rev. C* **48**, 2731 (1993).
- [19] S. Boffi, C. Giusti, and F. Pacati, *Phys. Rep.* **226**, 1 (1993).

- [20] V. Van der Sluys, K. Heyde, J. Ryckebusch, and M. Waroquier, *Phys. Rev. C* **55**, 1982 (1997).
- [21] R. Mercer, *Phys. Rev. C* **15**, 1786 (1977).
- [22] L. Cardman, D. Dowell, R. Gulbranson, D. Ravenhall, and R. Mercer, *Phys. Rev. C* **18**, 1388 (1978).
- [23] J. Heisenberg, *Adv. Nucl. Phys.* **12**, 61 (1981).
- [24] M. Rosenbluth, *Phys. Rev.* **79**, 615 (1950).
- [25] T. Donnelly and A. Raskin, *Ann. Phys.* **169**, 247 (1986).
- [26] A. Raskin and T. Donnelly, *Ann. Phys.* **191**, 78 (1989).
- [27] J. Bjorken and S. Drell, *Relativistic Quantum Mechanics* (Mc-Graw-Hill, New York, 1964).
- [28] J. Forest, V. Pandharipande, and A. Arriaga, *Phys. Rev. C* **60**, 014002 (1999).
- [29] B. Serot and J. Walecka, *Adv. Nucl. Phys.* **16**, 1 (1986).
- [30] H. Boersma and R. Malfliet, *Phys. Rev. C* **49**, 1495 (1994).
- [31] H. Müther, G. Knehr, and A. Polls, *Phys. Rev. C* **52**, 2955 (1995).
- [32] Y. Nedjadi and J. Rook, *Nucl. Phys. A* **585**, 641 (1995).
- [33] D. Phillips and S. Wallace, *Phys. Rev. C* **54**, 507 (1996).
- [34] P. Ring and P. Schuck, *The Nuclear Many-Body Problem* (Springer-Verlag, 1980).
- [35] J. Walecka, *Ann. Phys.* **83**, 491 (1974).
- [36] C. Horowitz, D. Murdock, and B. Serot, "The Relativistic Impulse Approximation," In *Computational Nuclear Physics*, K. Langanke, J. Moruhn, and S. Koonin, eds., p. 129 (Springer, Berlin, 1991).
- [37] B. Serot, *Phys. Lett. B* **86**, 146 (1979).
- [38] J. Piekarewicz and R. Rego, *Phys. Rev. C* **45**, 1654 (1992).
- [39] T. de Forest, *Nucl. Phys. A* **392**, 232 (1983).
- [40] H. Naus and J. Koch, *Phys. Rev. C* **36**, 2459 (1987).
- [41] S. Pollock, H. Naus, and J. Koch, *Phys. Rev. C* **53**, 2304 (1996).

- [42] J. Kelly, Phys. Rev. C **56**, 2672 (1997).
- [43] S. Nagorny and A. Dieperink, Eur. Phys. J. A **5**, 417 (1999).
- [44] F. Gross and D. Riska, Phys. Rev. C **36**, 1928 (1987).
- [45] J. Kelly, Phys. Rev. C **60**, 044609 (1999).
- [46] J. Mougey, M. Bernheim, A. Bussière, A. Gillebert, P. Hô, M. Priou, D. Royer, I. Sick, and G. Wagner, Nucl. Phys. A **262**, 461 (1976).
- [47] J. Caballero, T. Donnelly, E. Moya de Guerra, and J. Udias, Nucl. Phys. A **632**, 323 (1998).
- [48] M. Jones et al., Phys. Rev. Lett. **84**, 1398 (2000).
- [49] A. Picklesimer, J. Van Orden, and S. Wallace, Phys. Rev. C **32**, 1312 (1985).
- [50] A. Picklesimer and J. Van Orden, Phys. Rev. C **35**, 266 (1987).
- [51] A. Picklesimer and J. Van Orden, Phys. Rev. C **40**, 290 (1989).
- [52] J. Udias, P. Sarriguren, E. Moya de Guerra, E. Garrido, and J. Caballero, Phys. Rev. C **51**, 3246 (1995).
- [53] J. Udias, P. Sarriguren, E. Moya de Guerra, and J. Caballero, Phys. Rev. C **53**, R1488 (1996).
- [54] D. Yennie, D. Ravenhall, and R. Wilson, Phys. Rev. **95**, 500 (1954).
- [55] J. Johansson, H. Sherif, and G. Lotz, Nucl. Phys. A **605**, 517 (1996).
- [56] E. Cooper, S. Hama, B. Clarck, and R. Mercer, Phys. Rev. C **47**, 297 (1993).
- [57] R. Amado, J. Piekarewicz, D. Sparrow, and J. McNeil, Phys. Rev. C **28**, 1663 (1983).
- [58] W. Greenberg and G. Miller, Phys. Rev. C **49**, 2747 (1994).
- [59] H. Ito, S. Koonin, and R. Seki, Phys. Rev. C **56**, 3231 (1997).
- [60] O. Benhar, N. Nikolaev, J. Speth, A. Usmani, and B. Zakharov, Nucl. Phys. A **673**, 241 (2000).
- [61] S. Hama, B. Clarck, E. Cooper, H. Sherif, and R. Mercer, Phys. Rev. C **41**, 2737 (1990).
- [62] E. Cooper, B. Clarck, R. Kozack, S. Shim, S. Hama, J. Johansson, H. Sherif, R. Mercer, and B. Serot, Phys. Rev. C **36**, 2170 (1987).

- [63] C. Joachain, *Quantum Collision Theory* (Elsevier, Amsterdam, 1975).
- [64] Particle Data Group, “<http://pdg.lbl.gov>,”.
- [65] C. Ciofi degli Atti, L. Kaptari, and D. Treleani, *Phys. Rev. C* **63**, 044601 (2001).
- [66] R. Arndt, J. H. III, and L. Roper, *Phys. Rev. D* **35**, 128 (1987).
- [67] R. Arndt, L. Roper, R. Workman, and M. McNaughton, *Phys. Rev. D* **45**, 3995 (1992).
- [68] R. Arndt, I. Strakovsky, and R. Workman, *Phys. Rev. C* **50**, 2731 (1994).
- [69] R. Arndt, C. Oh, I. Strakovsky, R. Workman, and F. Dohrmann, *Phys. Rev. C* **56**, 3005 (1997).
- [70] R. Arndt, I. Strakovsky, and R. Workman, *Phys. Rev. C* **62**, 034005 (2000).
- [71] S. Wallace, *Adv. Nucl. Phys.* **12**, 135 (1981).
- [72] A. Kohama, K. Yazaki, and R. Seki, *Nucl. Phys. A* **551**, 687 (1993).
- [73] G. Arfken, *Mathematical Methods for Physicists* (Academic Press, Inc., 1985).
- [74] J. Ryckebusch, V. Van der Sluys, K. Heyde, H. Holvoet, W. Van Nespren, M. Waroquier, and M. Vanderhaegen, *Nucl. Phys. A* **624**, 581 (1997).
- [75] N. Nikolaev, A. Szczurek, J. Speth, J. Wambach, B. Zakharov, and V. Zoller, *Phys. Lett. B* **317**, 281 (1993).
- [76] R. Seki, T. Shoppa, A. Kohama, and K. Yazaki, *Phys. Lett. B* **383**, 133 (1996).
- [77] O. Benhar, A. Fabrocini, S. Fantoni, V. Pandharipande, and I. Sick, *Phys. Rev. Lett.* **69**, 881 (1992).
- [78] C. Gearheart, Ph.D. thesis, Washington University, St. Louis, 1994.
- [79] W. Dickhoff, Private communication.
- [80] K. Blomqvist et al., *Phys. Lett. B* **421**, 71 (1998).
- [81] R. Blankenbecler and S. Drell, *Phys. Rev. D* **36**, 277 (1987).
- [82] A. Akhiezer and N. Shul’ga, *Phys. Rep.* **234**, 297 (1993).
- [83] R. Blankenbecler and S. Drell, *Phys. Rev. D* **53**, 6265 (1996).
- [84] N. Bondarenko and N. Shul’ga, *Phys. Lett. B* **427**, 114 (1998).

- [85] A. Saha, W. Bertozzi, L. Weinstein, and K. Fissum, JLab PAC 18 Update for E89-003 (2000).
- [86] J. Udias, J. Caballero, E. Moya de Guerra, J. Amaro, and T. Donnelly, Phys. Rev. Lett. **83**, 5451 (1999).
- [87] D. Debruyne, J. Ryckebusch, W. Van Nespén, and S. Janssen, Phys. Rev. C **62**, 024611 (2000).
- [88] A. Bianconi and M. Radici, Phys. Rev. C **54**, 3117 (1996).
- [89] M. Leuschner et al., Phys. Rev. C **49**, 955 (1994).
- [90] S. Gardner and J. Piekarewicz, Phys. Rev. C **50**, 2822 (1994).
- [91] S. Jeschonnek and T. Donnelly, Phys. Rev. C **57**, 2438 (1998).
- [92] J. Udias and J. Vignote, Phys. Rev. C **62**, 034302 (2000).
- [93] S. Malov et al., Phys. Rev. C **62**, 057302 (2000).
- [94] A. Akhiezer and M. Rekaló, Sov. J. Part. Nucl. **3**, 277 (1974).
- [95] R. Arnold, C. Carlson, and F. Gross, Phys. Rev. C **23**, 363 (1981).
- [96] P. Bosted et al., Phys. Rev. Lett. **68**, 3841 (1992).
- [97] A. Lung et al., Phys. Rev. Lett. **70**, 718 (1993).
- [98] N. Makins et al., Phys. Rev. Lett. **72**, 1986 (1994).
- [99] T. O'Neill et al., Phys. Lett. B **351**, 87 (1995).
- [100] R. Woo et al., Phys. Rev. Lett. **80**, 456 (1998).
- [101] K. Kim, M. Cheoun, I.-T. Cheon, and Y. Ko, J. Kor. Phys. Soc. **35**, 399 (1999).
- [102] H. Naus, S. Pollock, J. Koch, and U. Oelfke, Nucl. Phys. A **509**, 717 (1990).
- [103] J. Johansson and H. Sherif, Phys. Rev. C **59**, 3481 (1999).
- [104] J. Ryckebusch, D. Debruyne, W. Van Nespén, and S. Janssen, Phys. Rev. C **60**, 034604 (1999).
- [105] S. Ulrych and H. Müther, Nucl. Phys. A **641**, 499 (1998).
- [106] S. Gilad, W. Bertozzi, and Z.-L. Zhou, Nucl. Phys. A **631**, 276c (1998).

- [107] S. Brodsky, In *Proceedings of the XIII International Symposium on Multiparticle Dynamics*, W. Kittel, W. Metzger, and A. Stergiou, eds., p. 963 (World Scientific, Singapore, 1982).
- [108] A. Mueller, In *Proceedings of the XVII Rencontre de Moriond*, J. T. T. Van, ed., p. 13 (Editions Frontières, Gif-sur-Yvette, 1982).
- [109] G. Farrar et al., *Phys. Rev. Lett.* **61**, 686 (1988).
- [110] L. Frankfurt and M. Strikman, *Phys. Rep.* **160**, 235 (1988).
- [111] A. Carroll et al., *Phys. Rev. Lett.* **61**, 1698 (1988).
- [112] J. Ralston and B. Pire, *Phys. Rev. Lett.* **61**, 1823 (1988).
- [113] D. Geesaman et al., *Phys. Rev. Lett.* **63**, 734 (1989).
- [114] G. Garino et al., *Phys. Rev. C* **45**, 780 (1992).
- [115] D. Abbott et al., *Phys. Rev. Lett.* **80**, 5072 (1998).
- [116] L. Frankfurt, M. Strikman, and M. Zhalov, *Phys. Rev. C* **50**, 2189 (1994).
- [117] V. Pandharipande and S. Pieper, *Phys. Rev. C* **45**, 791 (1992).
- [118] L. Frankfurt, M. Sargsian, and M. Strikman, *Phys. Rev. C* **56**, 1124 (1997).
- [119] L. Frankfurt, M. Strikman, and M. Zhalov, hep-ph/0011088 (2000).
- [120] L. Lapikas, G. van der Steenhoven, L. Frankfurt, M. Strikman, and M. Zhalov, *Phys. Rev. C* **61**, 064325 (2000).
- [121] J. Rycebusch, V. Van der Sluys, M. Waroquier, L. Kester, W. Hesselink, A. Zondervan, and E. Jans, *Phys. Lett. B* **333**, 310 (1994).
- [122] V. Van der Sluys, J. Rycebusch, and M. Waroquier, *Phys. Rev. C* **49**, 2704 (1994).
- [123] J. Rycebusch, Submitted to *Phys. Rev. C* .
- [124] J. Rycebusch, W. Van Nespén, and D. Debruyne, *Phys. Lett. B* **441**, 1 (1998).
- [125] J. Rycebusch, D. Debruyne, and W. Van Nespén, *Phys. Rev. C* **57**, 1319 (1998).
- [126] S. Janssen, J. Rycebusch, W. Van Nespén, and D. Debruyne, *Nucl. Phys. A* **672**, 285 (2000).
- [127] J. Rycebusch, S. Janssen, W. Van Nespén, and D. Debruyne, *Phys. Rev. C* **61**, 021603R (2000).